UNIVERSITY OF GENOA

Master's Degree in

CHEMICAL AND PROCESS ENGINEERING

Physicochemical Numerical Simulation of a Molten Carbonate Fuel Cell: Insights into Improving Current Collector Design

Supervisors:

Prof. Barbara Bosio

Prof. Marco Mazzuoli

Co-supervisors:

Prof. Fiammetta Rita Bianchi

Prof. Dario Bove

Candidate:

Davide Garibaldi

Academic Year 2025/2026

Contents

Abstract

Molten carbonate fuel cells are promising high-temperature electrochemical devices for efficient power generation and carbon dioxide capture. Their performance is strongly affected by gas distribution inside the cell, which is influenced by the geometry of the current collector.

This thesis investigates the effect of current collector design on the fluid-dynamic, mass-transport and electrochemical behaviour of a molten carbonate fuel cell. A three-dimensional numerical model was developed in COMSOL Multiphysics to compare a traditional arched collector with an innovative grooved geometry designed to improve gas accessibility to the porous electrodes.

The traditional collector generates local shielding, non-uniform gas supply and internal flow redistribution inside the porous electrode. By contrast, the grooved design provides a more distributed gas-access area, reduces hydraulic losses and promotes a more uniform reactant supply towards the reactive surface. Under the analysed operating conditions, the proposed geometry increases the average current density by approximately 5.4% and reduces the pressure drop by about 45%.

Overall, the study highlights the importance of current collector geometry as a key design parameter for improving transport uniformity, electrochemical performance and hydraulic behaviour in molten carbonate fuel cells.

Nomenclature

$(\cdot)'$ Local fluctuation with respect to an averaged quantity

$*$ Dimensionless quantity

$\boldsymbol{K}$ Viscous stress tensor

$\Delta E^0(T)$ Standard equilibrium potential difference at temperature T

ΔE_{eq} Local equilibrium potential difference calculated from the Nernst equation

$\Delta G^0(T)$ Standard Gibbs free-energy change of the global electrochemical reaction

Δp Reference pressure difference, $p_{\text{in}} - p_{\text{out}}$

ΔV Imposed cell-voltage difference

ϵ_{ij} Lennard–Jones energy parameter for the species pair i–j

κ Permeability of the porous electrode

$\mathbf{F}$ Volumetric force term

$\mathbf{I}$ Identity tensor

$\mathbf{N}_i$ Total molar flux of species i

$\mathbf{N}_{i,\text{conv}}$ Convective molar flux of species i

$\mathbf{N}_{i,\text{diff}}$ Diffusive molar flux of species i

$\mathbf{u}$ Gas-mixture velocity field

$\mathbf{u}^*$ Dimensionless velocity field

$\mathbf{x}$	Position vector
$\mathbf{x}^*$	Dimensionless position vector
ch	Feeding-channel region
Da_κ	Darcy number based on permeability, κ/L^2
$\mathrm{Da_I}$	Local first Damköhler number, $R_{\mathrm{WGS}}L/(Uc_{j,\mathrm{lim}})$
Eu	Euler number, $\Delta p/(\rho U^2)$
int	Quantity evaluated at the electrode–matrix interface
in	Inlet condition
lim	Limiting reactant used as reference
Ma	Mach number, U/c
out	Outlet condition
Pe_i	Local Péclet number of species i, $UL/D_{i,\mathrm{eff}}$
Re	Local Reynolds number, $\rho UL/\mu$
μ	Dynamic viscosity of the gas mixture
μ_{eff}	Effective viscosity in the Brinkman formulation
ν_i	Stoichiometric coefficient of species i
Ω_D	Diffusion collision integral
ω_x	Streamwise component of the vorticity vector
$\overline{(\,\cdot\,)}$	Section-averaged or area-averaged quantity
$\overline{j}$	Area-averaged current density
$\overline{p}^*(x)$	Section-averaged dimensionless pressure at axial position x
ϕ	Geometric void fraction of the channel region, $V_{\mathrm{fluid}}/V_{\mathrm{tot}}$
ψ	Free-area ratio of the current collector, $A_{\mathrm{free}}/A_{\mathrm{tot}}$

ρ Density of the gas mixture

ρ_{a} Reference density of the anodic gas mixture

ρ_{c} Reference density of the cathodic gas mixture

σ_i Lennard–Jones collision diameter of species i

σ_{ij} Mean collision diameter for the species pair i–j

τ Tortuosity of the porous electrode

ε_p Gas-accessible porosity of the porous electrode

a Anodic compartment or anodic quantity

a_i Thermodynamic activity of species i

A_{free} Electrode surface area directly exposed to the gas flow

A_{tot} Total geometric electrode area considered in the computational domain

c Cathodic compartment or cathodic quantity

c Speed of sound

c_i Molar concentration of species i

c_i^* Dimensionless concentration of species i

$c_{\mathrm{CO_2,c,lim}}$ Reference carbon-dioxide concentration on the cathodic side

$c_{\mathrm{H_2,a,lim}}$ Reference hydrogen concentration on the anodic side

$c_{j,\mathrm{lim}}$ Inlet concentration of the limiting reactant used as concentration scale

D Diameter of the reference circumference used to define the extraction region around the bump

D_A First heat-capacity correction coefficient in the Water Gas Shift equilibrium expression

D_B Second heat-capacity correction coefficient in the Water Gas Shift equilibrium expression

D_C Third heat-capacity correction coefficient in the Water Gas Shift equilibrium expression

d_p Representative pore diameter of the porous electrode

$D_{i,\mathrm{comb}}$ Combined molecular–Knudsen diffusivity of species i

$D_{i,\mathrm{eff}}$ Effective diffusivity of species i in the porous electrode

$D_{i,m}$ Mixture-averaged molecular diffusivity of species i

D_{ij} Binary molecular diffusion coefficient between species i and j

$D_{K,i}$ Knudsen diffusivity of species i

F Faraday constant

H^0 Standard enthalpy-related term in the Water Gas Shift equilibrium expression

H_{ch} Feeding-channel height

I Integration constant in the Water Gas Shift equilibrium expression

i, j Generic chemical-species indices

j Local current density

k_{B} Boltzmann constant

$K_{\mathrm{eq}}(T)$ Temperature-dependent equilibrium constant of the Water Gas Shift reaction

L Characteristic length

$L_{\mathrm{a,ch}}$ Characteristic length of the anodic feeding channel

$L_{\mathrm{a,p}}$ Characteristic length of the anodic porous electrode

$L_{\mathrm{c,ch}}$ Characteristic length of the cathodic feeding channel

$L_{\mathrm{c,p}}$ Characteristic length of the cathodic porous electrode

L_{cell} Modelled cell length

M_i Molar mass of species i

M_{ij} Reduced molecular-mass term for the species pair i–j

N Total number of species in the gas mixture

p Gas pressure

p Porous-electrode region

p'^{*} Local dimensionless pressure fluctuation with respect to the section-averaged value

p^{*} Dimensionless pressure, $(p - p_{\mathrm{out}})/\Delta p$

p^{0} Standard reference pressure

P_1 Pre-exponential parameter of the ohmic resistance contribution

P_2 Temperature parameter of the ohmic resistance contribution

P_3 Pre-exponential parameter of the cathodic carbon-dioxide resistance contribution

P_4 Temperature parameter of the cathodic carbon-dioxide resistance contribution

P_5 Pre-exponential parameter of the cathodic oxygen resistance contribution

P_6 Temperature parameter of the cathodic oxygen resistance contribution

P_7 Pre-exponential parameter of the anodic hydrogen resistance contribution

P_8 Temperature parameter of the anodic hydrogen resistance contribution

p_a^{int} Local gas pressure at the anodic electrode–matrix interface

p_c^{int} Local gas pressure at the cathodic electrode–matrix interface

p_i Partial pressure of species i

p_{in} Inlet pressure

p_{out} Outlet pressure

Q Volumetric flow rate

R Universal gas constant

r Base diameter of the bump

R^2 Coefficient of determination of the electrochemical-model fit

R_i Volumetric source or sink term of species i

$R_{\mathrm{an,H_2}}$ Anodic resistance contribution associated with hydrogen

$R_{\mathrm{cat,CO_2}}$ Cathodic resistance contribution associated with carbon dioxide

$R_{\mathrm{cat,O_2}}$ Cathodic resistance contribution associated with oxygen

R_{ohm} Ohmic area-specific resistance contribution

R_{tot} Total equivalent area-specific resistance

R_{WGS} Local molar rate of the Water Gas Shift reaction

s_{cc} Current-collector thickness

s_{el} Porous-electrode thickness

T Operating temperature

t Time

t^* Dimensionless time

U Characteristic velocity

u Streamwise velocity component

u^* Dimensionless streamwise velocity component

u_p^* Dimensionless streamwise velocity in the porous electrode

$U_{\mathrm{a,ch}}$ Characteristic streamwise velocity in the anodic feeding channel

$u_{\mathrm{a,in}}$ Anodic inlet gas velocity

$U_{\mathrm{a,p}}$ Characteristic through-plane velocity in the anodic porous electrode

$U_{\mathrm{c,ch}}$ Characteristic streamwise velocity in the cathodic feeding channel

$u_{\mathrm{c,in}}$ Cathodic inlet gas velocity

$U_{\mathrm{c,p}}$ Characteristic through-plane velocity in the cathodic porous electrode

u^*_{ch} Dimensionless streamwise velocity in the feeding channel

$U_{\mathrm{CO_2}}$ Carbon-dioxide utilisation factor

$U_{\mathrm{H_2}}$ Hydrogen utilisation factor

v Cross-stream or through-plane velocity component

v^*_p Dimensionless cross-stream velocity in the porous electrode

V_{cell} Applied cell voltage

V_{fluid} Volume available for fluid flow

V_{solid} Volume occupied by the solid phase

V_{tot} Total geometric volume

V_{void} Gas-accessible pore volume

w Spanwise velocity component

W_{cell} Modelled cell width

x Axial coordinate along the main gas-flow direction

x^*, y^*, z^* Dimensionless spatial coordinates

x_i Mole fraction of species i

y Cross-stream coordinate across the channel and porous-electrode thickness

y_i Molar fraction of species i

y_i^{int} Local molar fraction of species i at the electrode–matrix interface

$y_{\mathrm{CO_2},c}^{\mathrm{int}}$ Local carbon-dioxide molar fraction at the cathodic electrode–matrix interface

$y_{\mathrm{H_2},a}^{\mathrm{int}}$ Local hydrogen molar fraction at the anodic electrode–matrix interface

$y_{\mathrm{O_2},c}^{\mathrm{int}}$ Local oxygen molar fraction at the cathodic electrode–matrix interface

z Spanwise coordinate across the modelled cell width

Chapter 1

Introduction

The transition toward a low-carbon energy system represents one of the major technological, environmental and industrial challenges of the coming decades. International energy and climate scenarios indicate that a deep transformation of the global energy sector is needed in order to reduce greenhouse gas emissions and achieve climate neutrality by mid-century [1, 2]. The decarbonization of the energy sector requires the combined contribution of renewable electricity, hydrogen technologies, carbon capture and utilization systems, energy storage and high-efficiency conversion devices [1]. In this framework, Molten Carbonate Fuel Cells (MCFCs) are promising stationary power generators. In addition, the carbonate ion conduction mechanism makes MCFCs particularly relevant for carbon capture applications [3, 4].

Despite these advantages, the practical performance of MCFCs is strongly influenced by the internal distribution of gases, the transport of reacting species and the geometry of the cell components. The gas mixture must be effectively supplied to the porous electrodes, while the reaction products must be removed without generating excessive pressure losses and local transport limitations. Therefore, the design of the gas flow path and the current collector plays a critical role in determining both local and global electrochemical response of the cell [5, 6].

The current collector is a multifunctional component. It must guarantee electrical conduction, provide mechanical support and allow the gas mixture distribution in the porous electrodes. These requirements are not always easy to satisfy simultaneously. A geometry that provides good mechanical and electrical contact may partially shield the

electrode surface and reduce the direct accessibility of the gas to the active regions. This shielding effect can generate non-uniform pressure fields, local transport limitations and spatial variations in current density [5].

The aim of this thesis is to investigate theoretically the effect of current collector geometry on the fluid-dynamic, mass transport and electrochemical behaviour of a molten carbonate fuel cell. In particular, the work focuses on designing an innovative grooved geometry to improve gas accessibility to the porous electrodes and reduce the shielding effect, without weakening the cell mechanical stability. A comparison with a traditional current collector configuration, representative of a standard industrial solution, is carried out by three-dimensional numerical simulation in COMSOL Multiphysics. The study is performed under the same operating conditions and using the same assumptions in the model. This allows the differences observed in the velocity field, pressure distribution, material transport and current density distribution to be mainly attributed to the effect of the geometry in each studied configuration.

After this short introduction, the thesis is organized as follows.

Chapter 2 presents the theoretical and technological background of molten carbonate fuel cells. The operating principle of the cell is described, together with the main electrochemical reactions, the role of the molten carbonate electrolyte, the porous electrodes, the ceramic matrix and the current collectors. Particular attention is given to the limitations associated with gas transport, electrode accessibility and current collector shielding effects.

Chapter 3 describes the numerical model and the methodology adopted in the work. The two current collector geometries are introduced, namely the traditional configuration and the proposed grooved design. The computational domain, the main geometrical parameters and the governing equations for fluid flow, porous-medium transport, species balance, Water Gas Shift reaction and electrochemical behaviour are reported. The implementation of the model in COMSOL Multiphysics is also described.

Chapter 4 presents and discusses the numerical results. The comparison between traditional and grooved configurations is carried out mainly in terms of velocity field, pressure distribution, convective and diffusive transport of reactants, and current density distribution. The objective of this chapter is to connect the fluid-dynamic behaviour

induced by the collector geometry with the local mass transport phenomena and the resulting electrochemical response, to check the benefits of the proposed innovative design with respect to the traditional configuration.

Chapter 5 summarizes the main conclusions of the work and discusses possible future developments. The advantages and limitations of the proposed grooved current collector are highlighted, and further improvements of the numerical model and collector geometry are suggested.

Chapter 2

Molten Carbonate Fuel Cell Technology

After introducing the general energy context and motivation of the present work, this chapter focuses on the description of molten carbonate fuel cell technology. The aim is to provide the theoretical and technological background required to understand the numerical analysis developed in the following chapters.

Molten carbonate fuel cells are high-temperature devices that typically operate in the range of 850–970 K. This temperature range is required to keep the carbonate electrolyte in the molten state and to ensure adequate ionic mobility. The selected operating window represents a compromise between the need for high ionic conductivity and the limitation of carbonate volatilization phenomena and corrosion of metallic components [3].

From a structural standpoint, MCFC technology has been developed predominantly in a planar configuration, in which individual electrochemical cells are stacked and electrically connected in series through bipolar plates. This architecture allows high volumetric power densities and easier industrial scale-up compared to a tubular configuration [3]. From a structural standpoint, MCFC technology has been developed predominantly in a planar configuration, in which individual electrochemical cells are stacked and electrically connected in series through bipolar plates. This architecture allows high volumetric power densities and easier industrial scale-up compared to a tubular configuration [3].

A simplified representation of the main components of a planar MCFC unit is shown in Figure 2.1. The cell consists of porous anodic and cathodic electrodes separated by the electrolyte matrix, while current collectors and cell frames provide electrical connection, mechanical support and gas-distribution pathways.

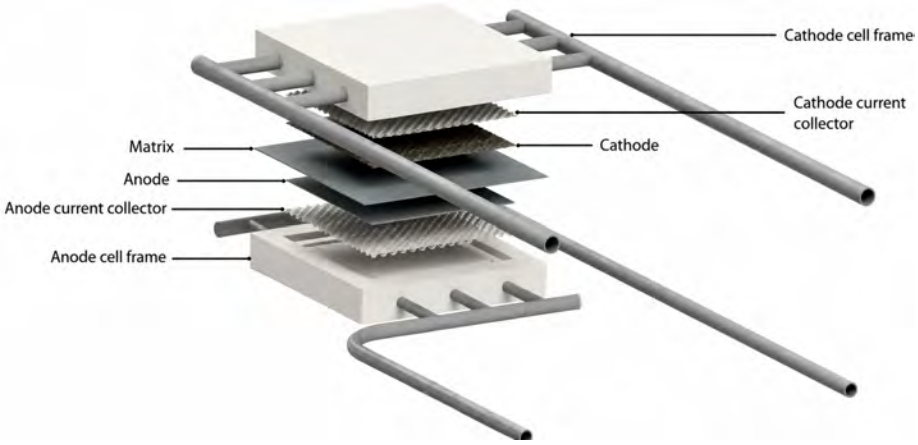

Figure 2.1: Schematic representation of the main components of a planar molten carbonate cell, including anode, cathode, electrolyte matrix, current collectors and cell frames. Adapted from Della Pietra et al. [7].

The arrangement of the reactant gas flows can follow cross-flow, co-flow or counter-flow configurations. In co-flow operation, the anodic and cathodic gases enter from the same side and are progressively depleted along the same axial direction, producing aligned concentration and temperature gradients. In counter-flow operation, the two streams enter from opposite sides, so that depleted gas on one side can locally face fresher gas on the other side. This configuration can promote a more distributed electrochemical driving force along the active length, although the opposite gas-composition gradients make the local coupling between the two electrodes more complex. In cross-flow operation, the perpendicular arrangement of the streams generates two-dimensional variations in reactant concentration, temperature and current density. The selected flow configuration therefore has a direct influence on the local operating conditions of the cell, as discussed in advanced MCFC modelling studies and in specific analyses of flow-direction effects in MCFC single cells [6, 8]. The following sections describe the electrochemical operating principle of MCFCs, the main materials used for anode, cathode, electrolyte and ceramic matrix, and the role of current collectors and interconnects. Particular attention is given to effects of the current collector geometry on the gas accessibility to porous electrodes since this aspect provides the theoretical basis

for the numerical simulation developed in the present thesis.

2.1 Electrochemical Operating Principle

The operation of molten carbonate fuel cells is based on the transport of ionic species through a molten carbonate electrolyte. In the conventional single-anion mechanism, ionic conduction is dominated by carbonate ions, ${CO_3}^{2-}$, which are generated at the cathode and consumed at the anode.

At the cathode, oxygen and carbon dioxide are reduced to form carbonate ions according to:

$$\frac{1}{2}\,O_2 + CO_2 + 2\,e^- \longrightarrow {CO_3}^{2-} \tag{2.1}$$

The carbonate ions migrate through the molten electrolyte toward the anode, where they react with hydrogen to produce water, carbon dioxide and electrons:

$$H_2 + {CO_3}^{2-} \longrightarrow H_2O + CO_2 + 2\,e^- \tag{2.2}$$

By summing the cathodic and anodic half-reactions, the overall reaction for the carbonate pathway is obtained:

$$H_2 + \frac{1}{2}\,O_2 + CO_{2(\mathrm{cat})} \longrightarrow H_2O + CO_{2(\mathrm{an})} \tag{2.3}$$

This reaction scheme makes carbon dioxide an essential species for MCFC operation. Here, CO_2 is required at the cathode to form carbonate ions and is regenerated at the anode. This characteristic enables the use of MCFCs not only for power generation but also as electrochemical devices for carbon dioxide capture and concentration [3].

More recent experimental and modelling studies have shown that, under humidified operating conditions and low CO_2 content at the cathode side, ionic transport may not be limited to carbonate anions alone. In these conditions, a dual-anion mechanism can occur, in which hydroxide ions, OH^-, also contribute to charge transport through the

electrolyte.

In this alternative pathway, water participates in a competitive cathodic semi-reaction, as follows:

$$\frac{1}{2}\,O_2 + H_2O + 2\,e^- \longrightarrow 2\,OH^- \tag{2.4}$$

while the anodic half-reaction is:

$$H_2 + 2\,OH^- \longrightarrow 2\,H_2O + 2\,e^- \tag{2.5}$$

By summing these two half-reactions, the overall reaction is:

$$H_2 + \frac{1}{2}\,O_2 \longrightarrow H_2O \tag{2.6}$$

Therefore, the ionic species involved in the charge transport of each mechanism are different, and this difference affects the local ionic balance, the electrolyte conductivity and the cell voltage. The relative contribution of each pathway depends on the fed gas composition, humidity level and operating conditions [9].

This effect is particularly relevant when MCFCs are operated as carbon-capture devices. In the carbonate pathway, the cell current is directly associated with the transport of carbonate ions from the cathode to the anode, resulting in the net transfer of CO_2 across the cell. Conversely, when the hydroxide-related pathway becomes significant, part of the current is carried by ionic species associated with water transport rather than by carbonate ions. As a consequence, a fraction of the electrical current no longer contributes directly to CO_2 transfer from the cathodic stream to the anodic side. This reduces the carbon-capture efficiency of the cell, since part of the electrochemical charge transport is diverted towards water-related transport processes instead of being fully exploited for CO_2 separation.

2.2 Anode Materials and Features

The MCFC anode is generally composed of porous nickel, sometimes alloyed with chromium or aluminium in order to improve mechanical stability and limit sintering at high operating temperatures. The anodic microstructure is designed to ensure high electronic conductivity, adequate permeability to the reactant gases and a sufficiently large active surface for the electrochemical oxidation of hydrogen.

From an electrochemical perspective, hydrogen oxidation is the dominant anodic reaction. The electrochemical oxidation of carbon monoxide is generally considered kinetically unfavourable under typical MCFC operating conditions. Consequently, the contribution of CO to direct current generation is limited, while carbon monoxide mainly participates in the Water Gas Shift (WGS) reaction [9].

The Water Gas Shift reaction can be written as:

$$CO + H_2O \rightleftharpoons CO_2 + H_2 \tag{2.7}$$

This reaction is particularly relevant in MCFCs operating with reformed fuels, because it modifies the local concentration of H_2, H_2O, CO and CO_2. In particular, it can contribute to the hydrogen availability in the anodic compartment and therefore indirectly affect the electrochemical response of the cell.

The porous microstructure of the anode influences gas diffusion, reactant distribution and current density distribution. Porosity, pore size distribution and tortuosity determine the ability of the fuel mixture to penetrate the electrode and reach the electrochemically active regions. Typical MCFC anodes are highly porous structures, with porosity values commonly in the range of approximately 0.50–0.70, in order to provide sufficient gas accessibility while maintaining adequate electronic conductivity and mechanical integrity [10].

The anode porosity is also essential for the formation of triple phase boundaries, where the electronic conducting electrode, the molten carbonate electrolyte and the gas phase coexist. These regions represent the effective electrochemically active sites, since hydrogen oxidation requires simultaneous access to gaseous reactants, ionic transport through

the electrolyte and electronic conduction through the electrode skeleton. Therefore, the pore network must be sufficiently open to allow gas transport, but also adequately filled or wetted by the electrolyte to sustain ionic continuity.

However, in view of the high operating temperature and the fast kinetics of hydrogen oxidation, the anode is often not the main limiting component for the overall MCFC performance [10].

2.3 Cathode Materials and Features

The MCFC cathode is typically made of porous nickel oxide, NiO. This material combines adequate electronic conductivity with sufficient catalytic activity for oxygen reduction in the presence of carbon dioxide. However, NiO is prone to dissolution in molten carbonates, leading to nickel migration and long-term performance degradation [3].

Several experimental studies have investigated strategies to improve cathode stability. In particular, chemical modification of NiO and the introduction of dopant elements have been shown to reduce dissolution rates and enhance electrochemical durability [11].

An alternative approach involves the use of composite cathode materials, such as $LiFeO_2$–$LiCoO_2$–NiO systems, which exhibit improved chemical stability while maintaining adequate electrocatalytic activity [12, 13].

Further studies have shown that the microstructural design of the cathode, particularly through layered structures and controlled pore size distributions, can improve mass transport and reduce polarisation losses [14]. Similar to the anode, the cathode must combine electrochemical activity, gas permeability, mechanical stability and chemical compatibility with the molten carbonate electrolyte.

MCFC cathodes are generally porous structures, with porosity values typically of the same order of magnitude as those adopted for the anode, commonly around 0.50–0.70, although the optimal value depends on the material formulation, electrolyte filling and operating conditions. The pore size distribution must allow effective transport of

the oxidising gas mixture, mainly CO_2 and O_2, while preserving sufficient electrolyte contact and electronic continuity. As discussed for the anode, the coexistence of gas phase, electrolyte and electronically conducting solid phase is required to sustain the electrochemical reaction at the active sites.

Typical pore sizes for MCFC cathodes are generally in the micrometre range, in order to balance gas accessibility and electrolyte retention. For this reason, both porosity and pore size distribution are key design parameters: excessively small pores can hinder gas diffusion, whereas excessively large pores may reduce electrolyte retention and the extension of the electrochemically active region.

2.4 Electrolyte and Ceramic Matrix Materials and Features

The MCFC electrolyte consists of an eutectic mixture of alkali carbonates, mainly Li_2CO_3/K_2CO_3 or Li_2CO_3/Na_2CO_3, which becomes liquid at the operating temperature of the cell. Since the electrolyte is in the molten state, it must be immobilized within a porous ceramic matrix. The ceramic matrix is therefore one of the most critical components of the entire MCFC technology.

The ceramic matrix separates the porous cathode from the porous anode, preventing direct mixing between fuel and oxidant streams while retaining the molten carbonate electrolyte by capillary forces. At the same time, the matrix must allow ionic conduction through the electrolyte and ensure electrical insulation between the two electrodes.

The reference material for the MCFC matrix is lithium aluminate, $LiAlO_2$, which provides a good compromise among chemical stability, mechanical strength and wettability with respect to molten carbonates [15].

The microstructure of the matrix, in terms of porosity, pore size and specific surface area, directly affects the ohmic resistance and operational stability of the cell. According to the review by Sheikh et al., suitable MCFC matrix behaviour is generally associated with porosity values in the range of approximately 50–70% and pore sizes

below 1 μm, with an optimal average pore-size distribution often reported around 0.1–0.3 μm [15].

These microstructural requirements are directly linked to the function of the matrix as an electrolyte-supporting and gas-separating layer. A sufficiently porous structure is necessary to retain an adequate amount of molten carbonate electrolyte and to provide continuous ionic conduction. At the same time, the pores must remain sufficiently small and uniformly distributed to promote capillary retention of the electrolyte and to avoid gas crossover between the anodic and cathodic compartments.

Microstructural coarsening, electrolyte loss and instability of the $LiAlO_2$ crystalline phases are therefore recognised as primary causes of long-term degradation [15]. Recent literature further emphasizes that the matrix should not be regarded as a purely inert component. In composite electrolyte configurations, the matrix may actively participate in ionic transport, opening new perspectives for improving MCFC performance and durability [15].

2.5 Current Collectors Materials and Features

In MCFC stacks, current collectors are essential components responsible for collecting and transporting the electrons generated by the electrochemical reactions occurring at the electrodes. They provide the electrical connection between adjacent cells, contribute to mechanical integrity and help define gas flow paths within the stack. Although they do not directly participate in the electrochemical reactions, their geometry, material properties and interface behaviour strongly influence the overall performance and durability of the cell.

Current collectors in MCFCs operate under particularly harsh conditions, characterized by high temperatures, direct contact with molten carbonates and exposure to different atmospheres. The anode side is exposed to reducing conditions, whereas the cathode side is exposed to oxidizing conditions. These operating conditions make material selection a critical aspect of stack design [3]. In this context, current collectors and interconnects must simultaneously ensure high electrical conductivity, sufficient mechanical stability, chemical compatibility with molten carbonates and adequate re-

sistance to corrosion. In addition to their electrical and mechanical functions, current collectors influence the accessibility of reactant gases to the porous electrodes. This effect is directly related to the collector geometry and to the fraction of electrode surface that remains exposed to the feeding channels. When solid portions of the collector cover part of the porous electrode, the gas cannot directly access the whole electrode surface and the covered regions become partially screened from the main stream. This local shielding of the electrode surface is here referred to as a *shadow effect*.

In these screened regions, reactants are supplied less directly than in the open areas facing the gas channel. Their transport towards the active electrode surface is therefore governed by lateral redistribution within the porous electrode and by diffusion from neighbouring exposed regions. As a consequence, the collector geometry can generate spatial gradients in reactant availability, with better supplied regions close to the openings and less effectively renewed regions below the solid portions of the collector.

This effect is particularly relevant for MCFC operation because the electrochemical reactions occur inside porous electrodes coupled with gas streams distributed by the current collector. A non-uniform gas access can locally increase concentration gradients between the feeding channel and the reactive surface, producing spatial variations in reactant concentration, current density and polarisation losses.

The detrimental effect of solid ribs or collector-covered regions on reactant access has been widely discussed in terms of under-rib mass-transport limitations and concentration polarisation in fuel-cell flow fields [16]. In the specific context of MCFCs, Lee et al. investigated different current-collector structures using three-dimensional fluid dynamics analysis and showed that a larger gas open area towards the electrodes improves diffusion characteristics and cell performance [5]. These findings indicate that the current collector cannot be considered only as an electrical component, since its shape also contributes to defining the local gas distribution and the transport conditions near the porous electrodes.

Material degradation represents another key issue for MCFC current collectors and interconnects. Recent literature has emphasized that metallic components are among the most critical elements in terms of long-term durability, since corrosion remains one of the primary causes of performance loss and instability in molten carbonate systems

[17]. High-temperature corrosion of metallic current collectors can lead to the formation of oxide or carbonate layers on the collector surface. These layers may increase the contact resistance and contribute to additional ohmic losses within the cell [18].

Experimental investigations have also highlighted that contact resistance at the electrode - collector interface can be a non-negligible contribution to total cell polarization. In particular, corrosion at the cathode-collector interface has been shown to increase local resistance and promote non-uniform current distributions on the active area [19]. Contact resistance is also influenced by mechanical compression. Milewski et al. showed that increasing compression force reduces contact resistance up to an optimal range, beyond which further improvements become limited. This highlights the coupling of electrochemical performance with mechanical design of the stack [20].

To mitigate degradation, several strategies have been proposed, including alloy optimization and protective coatings. Kim et al. demonstrated that cobalt electrodeposition and aluminium-based coatings can form stable lithiated oxide layers, such as $LiCoO_2$ and $LiAlO_2$, which reduce corrosion rates and improve the long-term stability of cathode current collectors and wet-seal regions [21]. These approaches confirm that current collector optimization cannot be limited to the selection of a conductive metal, but must also consider corrosion resistance, surface chemistry, contact conditions and the evolution of the electrode-collector interface during operation.

Despite their relevance, the geometrical and fluid-dynamic role of current collectors has been addressed less frequently than the microstructural optimisation of the main electrochemically active and electrolyte-retaining components. A substantial part of the MCFC literature is devoted to porous electrodes, cathode materials, layered electrode architectures and matrix degradation mechanisms, with particular attention to properties such as porosity, pore size distribution, phase stability and electrolyte retention [10, 11, 14, 15].

By contrast, current collectors and other metallic cell components are often discussed in relation to high-temperature corrosion, material stability, protective coatings and contact resistance [18, 19, 21, 20]. These aspects are essential for long-term operation, but they do not fully describe the influence of collector geometry on local gas accessibility and electrochemical response.

Only a smaller number of studies explicitly considers the current collector as a geometrical element controlling the transport of reactants between the gas channels and the porous electrodes.

A useful perspective can be obtained by comparing MCFC technology with other fuel cell systems, where current collectors and interconnects have been studied more extensively. In Proton Exchange Membrane Fuel Cells (PEMFCs), bipolar plates are considered core components of the stack. They are responsible not only for electron transport but also for gas distribution, water management and structural support. As a result, extensive research has focused on materials, coatings and manufacturing strategies to improve corrosion resistance and reduce costs [22].

Similarly, in Solid Oxide Fuel Cells (SOFCs), metallic interconnects act as current collectors and have been the subject of extensive investigation. A large body of literature has addressed degradation mechanisms such as oxidation, scale growth and chromium-related degradation phenomena, as well as mitigation strategies based on protective coatings and alloy design [23, 24]. In addition, electrode-interconnect contact resistance has been shown to represent a relevant contribution to ohmic losses and cell performance in planar SOFC configurations [25].

Compared with PEMFCs and SOFCs, the literature on MCFC current collectors appears more limited and less focused on integrated design strategies. This does not reduce the importance of the component; rather, it highlights the need to consider MCFC current collectors as multifunctional interface elements. Their corrosion behaviour, contact resistance, mechanical interaction with the electrodes and influence on gas accessibility can all affect efficiency, durability and lifetime. In this perspective, the optimization of collector materials, surface treatments, mechanical contact and flow-field geometry represents a relevant aspect in advanced MCFC development and provides the basis for the numerical analysis presented in the following chapters.

Chapter 3

Fluid Dynamics and Numerical Modeling

The previous chapter has introduced the main technological features of molten carbonate fuel cells and highlighted the functional role of current collectors within the stack. In particular, current collectors have been described not only as electrical and mechanical components but also as elements able to influence gas accessibility to the porous electrodes. Their geometry can partially shield the electrode surface, generating a shadow effect that may affect reactant distribution, local mass transport and the electrochemical response of the cell.

Starting from the objectives defined in Chapter 1, this chapter presents the numerical model adopted to evaluate the behaviour of the innovative grooved current collector, also compared to the traditional configuration. The purpose is to define the computational domain, the geometrical parameters used to characterize the collector designs and the governing equations adopted to describe gas motion, species transport, chemical reaction and local electrochemical response.

The considered domain represents a slice of cell, simplified as anodic feeding channel, porous anode, porous cathode and feeding cathodic channel. The matrix hosting the electrolyte is simplified as an interface between anodic and cathodic sections, since the study aims to evaluate current collector effects on electrode performance without a detailed simulation of all layers. At each side, the fed gas flows within the current collector and partially penetrates porous electrodes. The presence of the collector locally

modifies the cross-section available for fluid flow, inducing accelerations, decelerations, possible stagnation zones and pressure variations along the main flow direction. These phenomena are relevant because they influence the distribution of reactants and the ability of the system to maintain uniform operating conditions at the electrochemically active interface.

The formulation was developed with the aim of isolating the contribution of the collector geometry to the overall behaviour of the system. For this reason, the traditional and grooved configurations were analysed under the same operating conditions and by the same porous-medium and electrochemical kinetic models. In addition, the limiting case of a free channel was introduced as an ideal reference configuration, without internal obstacles, in order to evaluate the minimum fluid-dynamic resistance achievable within the considered domain.

The cell is assumed to operate under isothermal conditions. Therefore, temperature variations inside the computational domain are neglected and a uniform operating temperature is imposed in all the simulated regions. This assumption allows the analysis to focus on the effect of current collector geometry on fluid flow, species transport and local electrochemical response, without introducing additional thermal gradients and heat-transfer effects.

3.1 Feeding Channels and Current Collector Design

The geometries analysed in the present study were defined with the objective of evaluating the effect of the current collector configuration on the fluid-dynamic behaviour of the channel and on the accessibility of the gas mixture to the porous electrode. In particular, the selected configurations represent different levels of obstruction to gas motion and different degrees of direct exposure of the electrode surface.

The comparison was developed by considering configurations characterized by different distributions of the solid collector openings over the active area of the electrode. In this way, it is possible to evaluate how the geometrical arrangement of the collector affects the available flow section, the pressure losses and the ability of the gas to enter the porous electrode.

To quantify the degree of surface accessibility, a free-area ratio, denoted by ψ, was introduced and defined as:

$$\psi = \frac{A_{\text{free}}}{A_{\text{tot}}} \tag{3.1}$$

where ψ represents the free-area ratio, A_{free} is the electrode surface directly exposed to the gas flowing through the current collector and A_{tot} is the geometric area considered in the computational domain.

By definition, in the case of the free channel:

$$\psi = 1 \tag{3.2}$$

since the entire electrode surface is exposed to the gas flow. Conversely, in configurations where the collector partially occupies the surface above the electrode, the value of ψ is lower than unity. This parameter therefore makes it possible to compare the different geometries in terms of direct gas accessibility to the electrode surface.

However, the free-area ratio alone is not sufficient to describe the complete fluid-dynamic behaviour of the system. Two geometries may have similar values of ψ, but generate different velocity fields and pressure losses because of the different distribution of the solid volume inside the channel. For this reason, a second geometric parameter was introduced, namely the void fraction of the channel occupied by the collector:

$$\phi = \frac{V_{\text{fluid}}}{V_{\text{tot}}} \tag{3.3}$$

where ϕ represents the geometric void fraction, V_{fluid} is the volume available for fluid flow and V_{tot} is the total volume of the considered channel region.

The void fraction ϕ quantifies the degree of volumetric obstruction introduced by the collector inside the channel. High values of ϕ indicate a greater availability of volume for fluid flow and, in general, a lower obstruction to the gas mixture. In the limiting case of the free channel:

$$\phi = 1 \tag{3.4}$$

since the entire channel volume is occupied by the fluid.

The combined use of ψ and ϕ allows the geometries to be characterized both in terms of electrode surface accessibility and in terms of volumetric obstruction. The first parameter describes how much of the electrode is directly exposed to the gas flow, while the second quantifies how much channel volume remains available for fluid motion. The simultaneous evaluation of ψ and ϕ is important because these two parameters are directly related to two opposite design requirements. Increasing both parameters would generally favour gas flow, reduce geometrical obstruction and improve the accessibility of reactants to the porous electrode. However, a current collector cannot be designed only by maximizing the open area and the void volume, because it must also provide mechanical support and electrical contact under the compressive load applied to the cell. For this reason, the current collector design requires a compromise between fluid-dynamic performance and structural functionality. A very open geometry would approach the ideal behaviour of the free channel, but it could become mechanically weaker and less suitable for sustaining the clamping pressure required during cell operation. Conversely, a more closed geometry would provide higher mechanical support, but would increase the shadow effect and reduce the direct access of the gas to the electrode surface. In the present work, the traditional current collector was used as the reference configuration, characterized by a free-area ratio of approximately $\psi \simeq 0.60$. The proposed grooved geometry was designed to increase this value above 0.80, while maintaining a channel void fraction of approximately $\phi \simeq 0.80$. These values were selected to increase electrode accessibility while preserving a sufficient mechanical and electrical contact area. Therefore, the objective of the proposed geometry was not simply to maximize the open surface, but to obtain a more favourable balance between gas access, pressure losses and structural feasibility. This approach is consistent with the general indication reported in MCFC current collector studies, where larger gas-open areas are associated with improved diffusion between the gas channels and the porous electrodes, but the collector must still guarantee contact and support functions [5].

The geometric configurations applied at both cell sides in the study are therefore:

- the limiting case of the free channel, used as an ideal reference of minimum fluid-dynamic resistance;
- a traditional current collector configuration, representative of an industrial reference geometry;
- the alternative proposed grooved or embossed configuration, characterized by a higher degree of surface openness and a optimised shape of the profile to increase the mechanical resistance.

3.1.1 Free Channel

The free channel was introduced as an ideal reference configuration. In this geometry, the current collector is not present, leaving the entire channel cross-section available for the passage of the gas mixture and the entire electrode surface directly exposed to the fluid.

This configuration does not represent a solution applicable to a real cell, since the absence of the collector would prevent current collection and the maintenance of external electrical contact with the electrode. However, it constitutes a useful limiting case for evaluating the ideal fluid-dynamic behaviour of the system in the absence of internal obstacles.

The comparison with this configuration makes it possible to quantify how much the collector-equipped geometries deviate from the condition of minimum flow obstruction. In this sense, the free channel is used as a theoretical reference to evaluate the effectiveness of the alternative geometry studied in reducing fluid-dynamic resistance and in bringing the behavior of the system closer to the ideal condition.

3.1.2 Traditional Current Collector

The traditional current collector represents the industrial reference configuration. In MCFC stacks, the current collector and gas-distribution structure play a key role in directing the reactant gases over the active area and in determining the local fluid-dynamic conditions inside the cell [26]. The analysed configuration consists of a thin

planar structure characterised by a periodic distribution of openings and raised features over the active area. The geometry does not present a completely open surface, but rather a regular arrangement of alternating solid and empty elements, which define the paths available for the passage of the gas mixture.

The main geometric element is represented by a succession of raised arches, arranged in parallel and staggered rows. Each arch constitutes a three-dimensional solid element that develops above the collector plane and contributes to mechanical and electrical contact with the electrode. The staggered arrangement of the arches generates a periodic structure in which the solid elements are alternated between successive rows.

From the point of view of gas passage, the geometry is characterised by localised openings positioned in correspondence with the arches and by a regular distribution of small holes. The openings below the arches, together with the holes, allow the gas mixture to pass through the collector and reach the electrode surface. The contact between gas and electrode therefore does not occur through a completely open surface, but through a discrete network of passages distributed over the electrode geometric area.

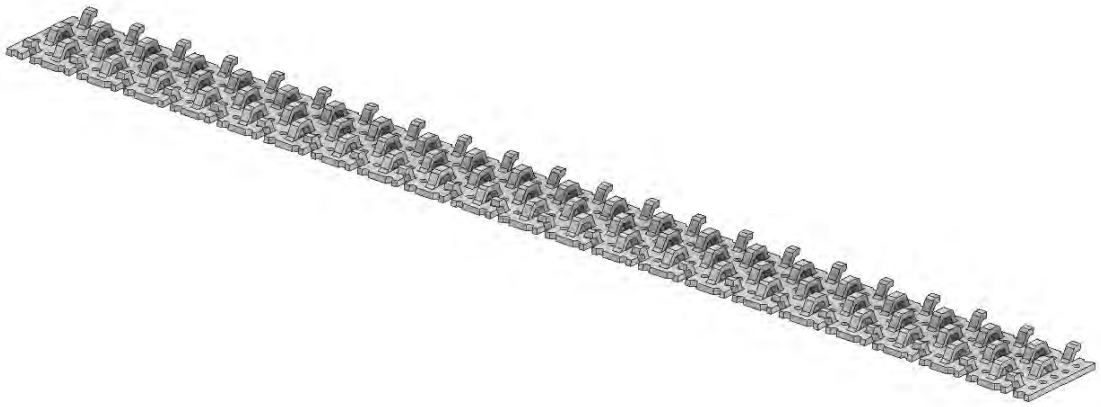

Figure 3.1: Three-dimensional representation of the traditional current collector geometry.

This configuration allows the gas to come into contact with different regions of the electrode, promoting a certain distribution of the fluid over the surface. However, the presence of arches also introduces a volumetric obstruction effect. The arches occupy part of the channel volume intended for the passage of the gas mixture, reducing the volume actually available to the fluid flow. Consequently, the gas is forced to pass

through the available openings and to bypass the solid elements, following locally non-straight paths.

The main limitation of the traditional configuration is represented by the relatively low free area available on the electrode. Although the collector is provided with openings below the arches and holes distributed over the surface, the contact between gas and electrode does not occur over the entire active area, but only through the regions left free by the collector geometry.

In the analysed case, the ratio between the electrode surface directly accessible to the gas and the total electrode surface is approximately $\psi = 0.60$. This means that a significant part of the electrode remains shielded by the solid elements of the collector and is not directly exposed to the gas flow. The openings present in the geometry still allow the fluid to be distributed over the active area, but this distribution is constrained by the position of the holes and of the gaps located below the arches.

3.1.3 Innovative Grooved Current Collector

The proposed alternative configuration consists of a current collector with an embossed or grooved surface, characterised by the presence of raised features distributed over the active area. These features were idealised using a truncated-cone geometry, selected to reduce the fraction of electrode surface covered by the collector while maintaining distributed mechanical and electrical contact.

A schematic two-dimensional section of the proposed geometry is shown in Figure 3.2. The lower side of the collector faces the porous electrode, whereas the opposite side is oriented towards the upper interface and the feeding-channel region. The truncated-cone embossments therefore define discrete contact regions with the porous electrode while leaving a large fraction of the electrode surface directly accessible to the gas phase.

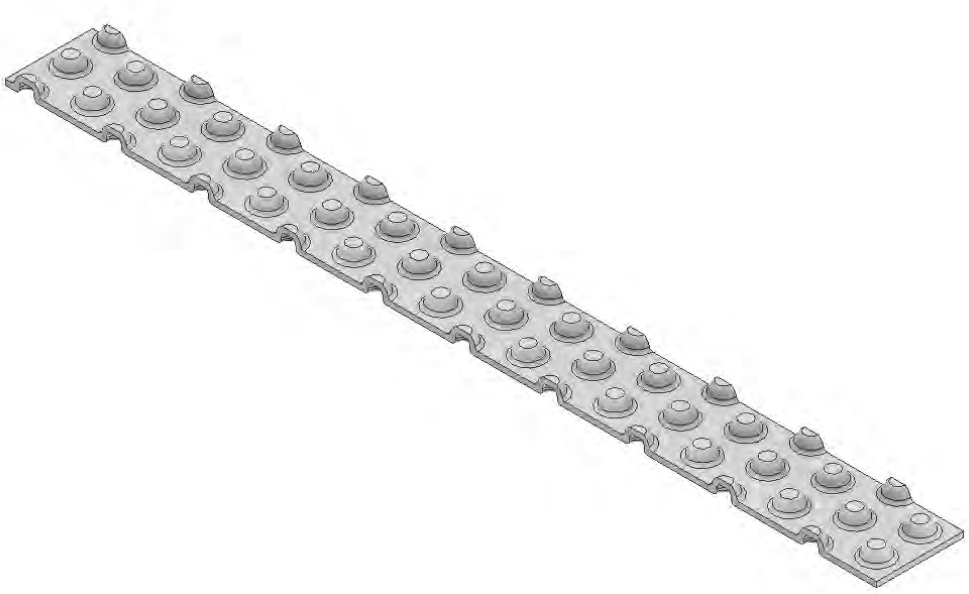

Figure 3.2: Schematic two-dimensional profile of the proposed grooved current collector, showing the porous-electrode interface and the upper interface facing the feeding-channel region.

Compared with the traditional arched configuration, the grooved geometry introduces a different interaction between the collector, gas flow and porous electrode. In the traditional collector, gas access to the electrode occurs through localised passages formed by the holes distributed over the surface and by the openings beneath the arches. The gas mixture must therefore pass through a discrete network of openings before reaching the underlying electrode.

In the grooved collector, gas access to the porous electrode is more direct. The electrode surface remains largely free and exposed to the gas flow, while the shielded regions are mainly associated with the contact footprints of the truncated-cone embossments. The gas can therefore redistribute through the open regions between neighbouring raised features rather than being constrained to pass through localised openings only. This configuration increases the free-area ratio ψ by increasing the fraction of the electrode surface directly exposed to the gas mixture.

The proposed geometry also avoids highly abrupt variations in the available flow domain. The inclined surfaces of the truncated-cone embossments introduce a more gradual geometrical transition than sharp or highly angular obstacles. This may contribute to limiting localised hydraulic losses and severe flow separation around the solid

features.

The raised elements were arranged according to a staggered pattern in order to avoid the formation of uninterrupted preferential flow paths between the inlet and outlet. The repeated offset arrangement promotes a progressive redistribution of the gas between neighbouring embossments and increases the interaction between the feeding flow and the electrode surface.

The proposed geometry was designed to maintain a channel void fraction of approximately 0.80, comparable to that of the traditional collector. This allows the free area available on the electrode to be increased without substantially reducing the volume available for gas flow. The grooved configuration therefore aims to increase ψ, associated with electrode-surface accessibility, while maintaining a high value of ϕ, associated with the volumetric availability of the channel.

The truncated-cone profile was also selected according to mechanical considerations. Point-like or nearly spherical contacts could concentrate the applied load over very small areas and generate severe local stresses on the underlying porous electrode. Such loading conditions could promote local indentation, crushing or alteration of the porous structure.

By contrast, the truncated-cone geometry provides a finite contact area and is therefore expected to distribute the applied load more effectively. This aspect is particularly relevant because MCFC stacks require assembly and clamping pressures to ensure contact between the cell components, gas sealing and stack integrity.

Zhang et al. analysed the assembly pressure of a high-power MCFC stack during the initial roasting stage and considered an assembly pressure of approximately 4.35 MPa [27]. This value confirms that the current-collector geometry should not be evaluated only in terms of gas accessibility and pressure losses, but also according to the mechanical load-transfer conditions generated under stack compression.

The grooved collector can therefore be interpreted as an intermediate solution between the traditional current collector and the limiting free-channel configuration. Compared with the traditional geometry, it reduces the fraction of electrode surface shielded by solid elements and provides more direct gas access to the porous layer. Compared with the free channel, it retains the solid structure required for mechanical support and

electrical contact.

3.2 Porous Electrode Model

To complete the geometric description of the model, the regions corresponding to the porous electrodes located below the current collectors were introduced. These represent the porous volume crossed by the gas mixture after its interaction with the collector geometry and therefore constitutes a fundamental part of the analysed domain.

In the present study, the electrodes were not modelled through an explicit description of their real microstructure and the liquid carbonate electrolyte phase inside the porous electrodes was not explicitly included, resulting in computational cost not consistent with the objectives of the analysis. The electrodes were therefore represented as a gas-accessible equivalent porous medium characterized by homogeneous macroscopic properties.

The characteristics of the porous medium, such as porosity and permeability, were defined in accordance with available experimental information and with values reported in the literature for similar electrodes. The porosity, denoted by ε, was defined as the fraction of the total electrode volume available for the passage of the gas phase:

$$\varepsilon = \frac{V_{\text{void}}}{V_{\text{tot}}} \tag{3.5}$$

where V_{void} represents the volume of pores accessible to the gas mixture, while V_{tot} indicates the overall geometric volume of the electrode considered in the computational domain. Equivalently, the porosity can be expressed as:

$$\varepsilon = 1 - \frac{V_{\text{solid}}}{V_{\text{tot}}} \tag{3.6}$$

where V_{solid} is the volume occupied by the solid phase of the electrode.

Permeability represents the ability of the porous medium to be crossed by the fluid and makes it possible to introduce into the model the resistance offered by the porous structure to the motion of the gas mixture. In the comparison between the different

collector configurations, the properties of the porous medium were kept constant. This choice makes it possible to isolate the effect of the collector geometry on the fluid-dynamic behaviour of the system.

The electrode domain was modelled up to the interface with the matrix hosting the electrolyte. The region consisting of matrix and electrolyte was not explicitly included in the present fluid-dynamic domain to avoid the introduction of additional physical phenomena and the excessive increase in the complexity of the model.

3.3 Physical Problem

After defining the current collector geometries and the representation of the electrodes as an equivalent porous medium, the problem is formulated with reference to the operation of a molten carbonate fuel cell. The computational domain represents a portion of the anodic and cathodic compartments. Each compartment includes a feeding channel with the corresponding current collector and the porous electrode region modelled up to the electrode/electrolyte interface.

The physical formulation aims to describe the transport of chemical species, the reaction development and the local electrochemical response of the cell. The current collector geometries play a direct role in the problem, since they modify the way in which the reactants are distributed along the electrode surface and influence the accessibility of the gas to the regions where the reactions occur.

Two possible feeding arrangements can be considered for the anodic and cathodic gas streams: co-flow and counter-flow. In the co-flow configuration, the anodic and cathodic streams enter the cell from the same side and flow along the same main direction. In this case, the local operating conditions of the two compartments evolve in the same axial direction, and the inlet regions of anode and cathode are spatially aligned. In the counter-flow configuration, instead, the anodic and cathodic streams enter the cell from opposite sides and flow in opposite directions. This arrangement can modify the axial distribution of species, partial pressures and current density, because the local anodic and cathodic gas compositions are coupled at different positions along the cell length. In principle, the numerical framework developed in the present work

could be applied to both configurations. However, the simulations presented in this thesis refer only to the co-flow arrangement.

The first phenomenon to be described is the motion of the gas mixture in the feeding channels and in the regions occupied by the current collectors. In these zones, transport is mainly convective: the mixture is carried along the main flow direction and interacts with the collector geometry. The presence of the collector locally modifies the velocity field, generating accelerations, decelerations and flow deviations. These non-uniformities may also induce local concentration gradients, especially near solid obstacles, openings and regions less crossed by the fluid.

The transport of chemical species is described through the concentrations c_i, the mole fractions x_i and the molar fluxes $\mathbf{N}_i$ of the individual species. In the anodic compartment, the mixture is representative of a fuel gas obtained from reforming processes and is mainly composed of H_2, H_2O, CO and CO_2. In the cathodic compartment, the mixture is representative of an oxidising gas containing O_2, CO_2 and inert N_2.

Inside the porous electrode, transport has a more complex nature than in the free channel. Part of the gas motion is due to the penetration of the mixture into the porous structure as a result of pressure gradients. This contribution can be interpreted as convective or permeative motion through the porous medium and is mainly controlled by permeability, porosity and pressure distribution. In addition, the diffusive contribution is linked to concentration gradients generated by the electrochemical reactions localized at the electrode/electrolyte interface. The consumption of reactants and the production of products modify the local composition of the mixture, creating concentration differences between the reactive zone and the outer regions of the electrode. Diffusion therefore tends to transport reactants toward the interface and to remove products from the reaction zone.

In the anodic domain, the Water Gas Shift reaction is also considered, both in the channel occupied by the collector and inside the porous medium. This reaction locally modifies the concentrations of H_2, H_2O, CO and CO_2, indirectly influencing the availability of hydrogen for the anodic electrochemical reaction.

Electrochemical reactions are considered to be localized at the interface between the electrode and the matrix. At this interface, reactant transport is coupled with current

production through the anodic and cathodic semi-reactions.

Overall, the physical problem can be interpreted as the coupling among fluid motion, species transport, chemical reaction and electrochemical response. The governing equations are introduced in the following sections by distinguishing among momentum balance, material balances with a focus on transport mechanisms in the porous medium, Water Gas Shift reaction and interfacial electrochemical kinetic model.

3.3.1 Momentum Balance

The computational domain includes free-flow regions, corresponding to the feeding channels and to the spaces available around the current collectors, and porous regions, corresponding to the electrodes. In the feeding channels, the gas mixture flows in an open domain and its motion is described by the Navier–Stokes equations, whose historical development is associated with the works of Navier and Stokes on viscous fluid motion [28, 29]. Inside the electrodes, instead, the gas moves through an equivalent porous medium and the momentum balance is described by a Brinkman formulation [30].

In the feeding channels, the gas mixture is treated as a continuous Newtonian fluid. The momentum balance is written in the standard form for a Newtonian fluid [31]:

$$\rho\frac{\partial \mathbf{u}}{\partial t} + \rho\left(\mathbf{u}\cdot\nabla\right)\mathbf{u} = \nabla\cdot\left(-p\mathbf{I} + \boldsymbol{K}\right) + \mathbf{F} \tag{3.7}$$

where $\mathbf{u}$ is the velocity field, p is the pressure, ρ is the gas density, $\mathbf{I}$ is the identity tensor and $\mathbf{F}$ represents possible volumetric force terms, which are neglected in the present channel domain. The tensor $\boldsymbol{K}$ represents the viscous stress contribution and, for a Newtonian fluid, is expressed as [31]:

$$\boldsymbol{K} = \mu\left[\nabla\mathbf{u} + \left(\nabla\mathbf{u}\right)^T\right] \tag{3.8}$$

where μ is the dynamic viscosity of the gas mixture.

The gas mixture was treated as incompressible in the fluid-dynamic model. This assumption is justified by the low characteristic velocities involved in the simulations.

In fact, the gas velocities are of the order of a few $\mathrm{m\,s^{-1}}$, while the speed of sound under the operating conditions of the cell is of the order of several hundreds of $\mathrm{m\,s^{-1}}$. Therefore, the Mach number,

$$\mathrm{Ma} = \frac{U}{c} \tag{3.9}$$

where U is the characteristic gas velocity and c is the speed of sound, is much lower than the conventional limit of $\mathrm{Ma} \simeq 0.3$ commonly used to neglect compressibility effects. Under these conditions, density variations induced by pressure changes are negligible for the purpose of the present fluid-dynamic analysis.

The momentum balance is therefore associated with the incompressible continuity equation, which derives from the conservation of mass under constant-density conditions [31]:

$$\nabla \cdot \mathbf{u} = 0 \tag{3.10}$$

Inside the electrodes, modelled as equivalent porous media, the gas motion is described by the Brinkman equation. This formulation extends the classical Darcy description by including a viscous stress contribution, allowing a smoother coupling between the free-flow channel and the porous electrode [30]. The momentum balance in the porous domain is written as:

$$\frac{\rho}{\varepsilon_p}\frac{\partial \mathbf{u}}{\partial t} + \frac{\rho}{\varepsilon_p}\left(\mathbf{u}\cdot\nabla\right)\left(\frac{\mathbf{u}}{\varepsilon_p}\right) = \nabla\cdot\left(-p\mathbf{I} + \boldsymbol{K}\right) - \mu\kappa^{-1}\mathbf{u} + \mathbf{F} \tag{3.11}$$

where ε_p is the porosity of the porous medium and κ is its permeability. The permeability describes the ability of the porous electrode to be crossed by the gas mixture and is strongly related to the microstructural properties of the medium, such as porosity and pore size. In the present model, volumetric force terms are neglected also in the porous domain.

The viscous stress tensor in the porous region is expressed as:

$$\boldsymbol{K} = \frac{\mu}{\varepsilon_p}\left[\nabla \mathbf{u} + (\nabla \mathbf{u})^T\right] \tag{3.12}$$

where the term μ/ε_p represents the effective viscosity contribution adopted in the Brinkman formulation. Compared with the free-flow domain, the presence of the porosity term accounts for the reduced volume effectively available for gas motion inside the porous electrode.

The resistive term of the Brinkman equation is:

$$\mu\kappa^{-1}\mathbf{u} \tag{3.13}$$

and describes the resistance offered by the porous structure to the passage of the gas mixture. Since this contribution is inversely proportional to the permeability, a decrease in κ produces a stronger damping of the velocity field inside the porous electrode.

A commonly adopted relation for estimating the permeability of porous media is the Kozeny–Carman equation, which links κ to the porosity ε_p and to a representative microstructural length scale [32, 33]. In its classical form, the equation is derived for packed beds and uses a characteristic particle diameter. In porous electrodes, however, the same relation is often used as an approximate macroscopic estimate by introducing a representative pore or microstructural diameter. In the present work, d_p is therefore interpreted as a representative pore diameter of the electrode, consistently with the available microstructural information used to define the porous domain.

$$\kappa = \frac{\varepsilon_p^3 d_p^2}{180\,(1-\varepsilon_p)^2} \tag{3.14}$$

where κ is the permeability, ε_p is the porosity and d_p is the representative pore diameter. According to this relation, the permeability increases with increasing porosity. A higher value of ε_p corresponds to a larger fraction of void volume available for the gas phase and therefore to a lower resistance to flow. Conversely, when the porosity decreases, the available pathways for the gas become more restricted, leading to a lower permeability and to a stronger attenuation of the velocity field inside the porous electrode.

3.3.2 Material Balance and Species Transport

The transport of chemical species is described by a material balance for each species i, according to the standard conservation form for multicomponent mass transport [31, 34]:

$$\frac{\partial c_i}{\partial t} + \nabla \cdot \mathbf{N}_i = R_i \tag{3.15}$$

where c_i is the concentration of species i, $\mathbf{N}_i$ is the total molar flux and R_i represents the source or sink term due to chemical and electrochemical reactions.

The total molar flux can be expressed as the sum of a convective contribution and a diffusive contribution. Assuming a Fickian description of diffusion, the molar flux is written as [35, 31, 34]:

$$\mathbf{N}_i = c_i \mathbf{u} - D_{i,\text{eff}} \nabla c_i \tag{3.16}$$

where $c_i \mathbf{u}$ represents convective transport and $-D_{i,\text{eff}} \nabla c_i$ represents diffusion due to concentration gradients according to Fick's law.

In the porous medium, diffusion is not described by considering molecular diffusivity alone. Since transport occurs inside pores of finite size, the contribution of Knudsen diffusion, associated with the interaction between gas molecules and pore walls, must also be considered. The combined molecular–Knudsen diffusivity is then corrected by the porosity and tortuosity of the porous structure [34, 36, 37]:

$$D_{i,\text{eff}} = \frac{\varepsilon}{\tau} D_{i,\text{comb}} \tag{3.17}$$

where ε is the porosity of the porous medium, τ is the tortuosity and $D_{i,\text{comb}}$ is a combined diffusivity accounting for both molecular diffusion and Knudsen diffusion.

A possible expression for the combined diffusivity is given by the reciprocal addition of the molecular and Knudsen contributions, commonly used to represent the combined resistance to diffusion in porous media [36, 34]:

$$\frac{1}{D_{i,\mathrm{comb}}} = \frac{1}{D_{i,m}} + \frac{1}{D_{K,i}} \tag{3.18}$$

where $D_{i,m}$ represents the molecular diffusivity of species i in the gas mixture and $D_{K,i}$ represents the Knudsen diffusivity.

The molecular diffusivity $D_{i,m}$ was evaluated using the Wilke–Lee model for binary gas diffusion coefficients [38]. This model is based on the kinetic theory of gases and relates the binary diffusivity of two gaseous species to temperature, pressure, molecular weight and molecular interaction parameters.

The binary diffusion coefficient between species i and j is expressed as [38]:

$$D_{ij} = \frac{\left[3.03 - \frac{0.98}{M_{ij}^{1/2}}\right] 10^{-3} T^{3/2}}{p M_{ij}^{1/2} \sigma_{ij}^2 \Omega_D} \tag{3.19}$$

where D_{ij} is the binary diffusion coefficient, T is the temperature, p is the pressure, σ_{ij} is the characteristic collision length and Ω_D is the diffusion collision integral. The term M_{ij} is the reduced molecular weight of the binary pair, defined as:

$$M_{ij} = 2\left[\frac{1}{M_i} + \frac{1}{M_j}\right]^{-1} \tag{3.20}$$

where M_i and M_j are the molecular weights of species i and j, respectively.

The characteristic collision length is calculated from the molecular collision diameters of the two species:

$$\sigma_{ij} = \frac{\sigma_i + \sigma_j}{2} \tag{3.21}$$

where σ_i and σ_j are the characteristic molecular lengths of species i and j. The diffusion collision integral Ω_D accounts for the interaction between the diffusing molecules and depends on the reduced temperature, defined as:

$$T^* = \frac{k_\mathrm{B} T}{\varepsilon_{ij}} \tag{3.22}$$

where k_B is the Boltzmann constant and ε_{ij} is the characteristic energy parameter of the molecular interaction. For polar molecules, the collision integral can also include the effect of the dipole moment, which modifies the interaction potential between the diffusing species.

Since the gas phase is composed of multicomponent mixtures, the molecular diffusivity of each species was not treated as a single binary coefficient, but as an average diffusivity in the gas mixture. Starting from the binary diffusion coefficients D_{ij} obtained with the Wilke–Lee model, the mixture-averaged diffusivity of species i was calculated as [31, 34]:

$$D_{i,m} = \frac{1 - y_i}{\sum_{\substack{j=1 \\ j \neq i}}^{N} \frac{y_j}{D_{ij}}} \tag{3.23}$$

where $D_{i,m}$ is the mixture-averaged molecular diffusivity of species i, y_i is the molar fraction of species i, y_j is the molar fraction of the generic species j, D_{ij} is the binary diffusion coefficient between species i and j, and N is the total number of species in the gas mixture.

This formulation allows the molecular diffusivity of each species to account for the presence of the other components in the gas phase. Therefore, the value of $D_{i,m}$ depends not only on the binary interaction between two species, but also on the overall mixture composition.

The Knudsen diffusivity accounts for the interaction between gas molecules and the pore walls. It becomes relevant when the characteristic pore size is sufficiently small for molecule–wall collisions to influence gas transport. It can be expressed as [36, 34]:

$$D_{K,i} = \frac{d_p}{3} \sqrt{\frac{8RT}{\pi M_i}} \tag{3.24}$$

where d_p is the representative pore diameter, R is the universal gas constant, T is the local temperature and M_i is the molar mass of species i.

The tortuosity was estimated through a Bruggeman-type relation, following the theoretical approach adopted in MCFC modelling studies [37]:

$$\tau = \varepsilon^{-1/2} \tag{3.25}$$

This correction accounts for the fact that the gas does not diffuse through straight channels but through tortuous pathways inside the porous electrode. As a consequence, the effective diffusivity is lower than the corresponding gas-phase diffusivity. The representative pore diameter d_p affects the Knudsen contribution, while porosity and tortuosity account for the reduction in transport due to the porous structure.

3.3.3 Water Gas Shift Model

In the anodic domain, the Water Gas Shift reaction was included in order to describe the local redistribution of CO, H_2O, CO_2 and H_2. This reaction is particularly relevant when the fuel stream contains carbon monoxide and steam, because it can affect the local hydrogen availability before the electrochemical reaction takes place.

Consistently with the modelling approach reported by Lee et al. [5], the Water Gas Shift reaction was treated as an equilibrium reaction. Therefore, its local behaviour was described through a temperature-dependent equilibrium constant, rather than by introducing independent forward and reverse kinetic constants.

In the present model, the equilibrium formulation was applied in both the anodic interconnect/channel region and the porous anode. This choice follows the control-volume approach adopted in the reference modelling work [5]. Physically, this assumption is justified by the fact that the reformate gas composition can evolve before entering the porous electrode and can continue to change during penetration through the porous structure.

The Water Gas Shift reaction is written as:

$$CO + H_2O \rightleftharpoons CO_2 + H_2 \tag{3.26}$$

Assuming the direction toward the formation of carbon dioxide and hydrogen positive, the equilibrium constant is defined as:

$$K_{\mathrm{eq}}(T) = \frac{a_{\mathrm{CO_2}} a_{\mathrm{H_2}}}{a_{\mathrm{CO}} a_{\mathrm{H_2O}}} \tag{3.27}$$

where a_i represents the activity of species i. Working near atmospheric pressure in MCFCs, ideal gas mixtures were considered and the activities were approximated by normalized partial pressures:

$$a_i = \frac{p_i}{p^0} \tag{3.28}$$

where p_i is the partial pressure of species i and p^0 is the reference pressure.

The temperature dependence of the equilibrium constant was introduced as:

$$\ln K_{\mathrm{eq}} = I - \frac{H^0}{RT} + \frac{D_A}{R} \ln T + \frac{D_B}{2R} T + \frac{D_C}{6R} T^2 \tag{3.29}$$

and therefore:

$$K_{\mathrm{eq}}(T) = \exp\left[I - \frac{H^0}{RT} + \frac{D_A}{R} \ln T + \frac{D_B}{2R} T + \frac{D_C}{6R} T^2 \right] \tag{3.30}$$

where I, H^0, D_A, D_B and D_C are thermodynamic parameters of the equilibrium expression, R is the universal gas constant and T is the local anodic temperature.

The parameters used to calculate the local value of $K_{\mathrm{eq}}(T)$ at the imposed anodic operating temperature are reported in Table 3.1.

Table 3.1: Parameters adopted for the equilibrium formulation of the Water Gas Shift reaction.

Parameter	**Description**	**Value**	**Unit**
I	Integration constant of the equilibrium expression	-5.0927801	–
H^0	Standard enthalpy-related term of the equilibrium expression	-4.182×10^4	$\mathrm{Jmol^{-1}}$
D_A	Heat-capacity correction coefficient	-9.125×10^{-1}	$\mathrm{Jmol^{-1}K^{-1}}$
D_B	Heat-capacity correction coefficient	2.382×10^{-2}	$\mathrm{Jmol^{-1}K^{-2}}$
D_C	Heat-capacity correction coefficient	-1.219×10^{-5}	$\mathrm{Jmol^{-1}K^{-3}}$
R	Universal gas constant	8.3145	$\mathrm{Jmol^{-1}K^{-1}}$

This approach allows the local anodic gas composition to be related to the thermodynamic equilibrium of the WGS reaction at the operating temperature. In the channel/interconnect region, it accounts for the re-equilibration of the anodic gas mixture before it reaches the porous electrode. In the porous anode, it accounts for the additional composition adjustment occurring while the gas diffuses and convects toward the reactive surface. As a consequence, the local concentrations of CO, H_2O, CO_2 and H_2 can be consistently updated, influencing hydrogen availability in the anodic compartment.

3.3.4 Electrochemical Kinetic Model

The electrochemical reactions are considered localized at the interface between electrode and matrix. The local electrochemical behaviour is described starting from the equilibrium potential, or Nernst potential, which represents the reversible cell voltage under the local conditions of temperature and composition.

The equilibrium potential can be expressed as:

$$\Delta E_{\text{eq}} = \Delta E^0(T) + \frac{RT}{2F} \ln \left[\frac{a_{\text{H}_2,a} a_{\text{O}_2,c}^{1/2} a_{\text{CO}_2,c}}{a_{\text{H}_2\text{O},a} a_{\text{CO}_2,a}} \right] \tag{3.31}$$

where $\Delta E^0(T)$ is the standard potential at temperature T, R is the universal gas constant, F is Faraday's constant and a_i are the activities of the species involved.

For ideal gases at atmospheric operative pressure, using partial pressures normalized with respect to the standard pressure p^0, it can be written as:

$$\Delta E_{\text{eq}} = \Delta E^0(T) + \frac{RT}{2F} \ln \left[\frac{(p_{\text{H}_2,a}/p^0) \, (p_{\text{O}_2,c}/p^0)^{1/2} \, (p_{\text{CO}_2,c}/p^0)}{(p_{\text{H}_2\text{O},a}/p^0) \, (p_{\text{CO}_2,a}/p^0)} \right] \tag{3.32}$$

The term $\Delta E^0(T)$ can be expressed starting from the standard Gibbs free energy change of the global reaction:

$$\Delta E^0(T) = -\frac{\Delta G^0(T)}{2F} \tag{3.33}$$

Once the equilibrium potential has been defined, the local electrochemical response of the cell is described through an effective resistive formulation. The local voltage can be expressed as:

$$\Delta V = \Delta E_{\text{eq}} - jR_{\text{tot}} \tag{3.34}$$

where ΔV is the local cell voltage, j is the local current density and R_{tot} is the total equivalent resistance.

The local electrochemical response was described through the effective MCFC kinetic model proposed by Audasso, Bosio and Nam [39]. In this formulation, the global cell overpotential is represented by means of equivalent resistance contributions associated with ohmic losses and with the main anodic and cathodic reaction limitations. This approach makes it possible to express the local current density as a function of local temperature, pressure and gas composition at the electrode/matrix interface. The total equivalent resistance is expressed as:

$$R_{\text{tot}} = R_{\text{ohm}} + R_{\text{an,H}_2} + R_{\text{cat,CO}_2} + R_{\text{cat,O}_2} \tag{3.35}$$

where R_{tot} is the total local resistance, R_{ohm} is the ohmic contribution, $R_{\text{an,H}_2}$ is the anodic resistance contribution associated with hydrogen, and $R_{\text{cat,CO}_2}$ and $R_{\text{cat,O}_2}$ are the cathodic resistance contributions associated with carbon dioxide and oxygen, respectively. The ohmic contribution is expressed as:

$$R_{\text{ohm}} = P_1 \exp\left(\frac{P_2}{T}\right) \tag{3.36}$$

where P_1 is the pre-exponential coefficient of the ohmic resistance, P_2 is the corresponding temperature coefficient and T is the local cell temperature. This term accounts for the temperature-dependent ohmic losses of the cell. The cathodic contribution associated with carbon dioxide is expressed as:

$$R_{\text{cat,CO}_2} = \frac{P_3 T \exp\left(\frac{P_4}{T}\right)}{p_c^{\text{int}} \ln\left[\left(1 - 1.5 y_{\text{CO}_2,c}^{\text{int}}\right)^{-1}\right]} \tag{3.37}$$

where P_3 is the pre-exponential parameter associated with the cathodic carbon dioxide

contribution and P_4 is the corresponding temperature parameter. The term p_c^{int} represents the local gas pressure at the cathodic electrode/matrix interface, while $y_{\text{CO}_2,c}^{\text{int}}$ is the local molar fraction of carbon dioxide at the same interface. Therefore, this resistance depends not only on temperature, but also on the local availability of CO_2 at the cathodic reactive surface. The cathodic contribution associated with oxygen is calculated as:

$$R_{\text{cat,O}_2} = \frac{P_5 T \exp\left(\frac{P_6}{T}\right) \left(p_c^{\text{int}}\right)^{1/2} y_{\text{CO}_2,c}^{\text{int}} \left(y_{\text{O}_2,c}^{\text{int}}\right)^{1/2}}{\ln\left[\left(1 - 3y_{\text{O}_2,c}^{\text{int}}\right)^{-1}\right]} \tag{3.38}$$

where P_5 and P_6 are the pre-exponential and temperature parameters associated with the oxygen-related cathodic contribution. The term $y_{\text{O}_2,c}^{\text{int}}$ is the local molar fraction of oxygen at the cathodic electrode/matrix interface. This expression accounts for the dependence of the cathodic polarization on both oxygen and carbon dioxide availability, consistently with the cathodic semi-reaction of MCFCs, where both species are involved in carbonate ion formation. The anodic contribution associated with hydrogen is written as:

$$R_{\text{an,H}_2} = \frac{P_7 T \exp\left(\frac{P_8}{T}\right)}{p_a^{\text{int}} \ln\left(1 + y_{\text{H}_2,a}^{\text{int}}\right)} \tag{3.39}$$

where P_7 and P_8 are the pre-exponential and temperature parameters associated with the anodic hydrogen contribution. The term p_a^{int} represents the local gas pressure at the anodic electrode/matrix interface, while $y_{\text{H}_2,a}^{\text{int}}$ is the local hydrogen molar fraction at the same interface. This term therefore links the anodic resistance to the local availability of hydrogen, which is the main reacting species consumed at the anode. The superscript "int" indicates that the quantities are evaluated locally at the electrode/matrix interface, where the electrochemical reactions are assumed to occur. This is important because the pressure and composition at the interface can differ from the corresponding values in the feeding channel, due to porous-medium resistance, diffusion, convection and local reaction source terms. As a consequence, the current density is calculated from the local interfacial operating conditions rather than from inlet or bulk gas properties. In the present work, the electrochemical model was implemented under potentiostatic operating conditions. This means that the cell voltage was imposed as an input parameter, while the local current density was calculated as the response of the system. The relation can therefore be rearranged to obtain the local

current density:

$$j = \frac{\Delta E_{\text{eq}} - \Delta V}{R_{\text{tot}}} \tag{3.40}$$

where j is the local current density, ΔE_{eq} is the local equilibrium potential difference calculated from the Nernst relation, ΔV is the imposed cell voltage difference and R_{tot} is the total equivalent resistance. Under potentiostatic conditions, ΔV is fixed, while ΔE_{eq} and R_{tot} vary locally because they depend on the pressure, temperature and composition at the anodic and cathodic interfaces. Therefore, spatial variations in gas distribution and species availability are directly reflected in the calculated current density field.

3.4 Non-Dimensional Formulation

After introducing the dimensional governing equations, the problem can be reformulated in dimensionless form. Through non-dimensionalisation, the physical variables are scaled by characteristic quantities of the system, resulting in dimensionless variables of order unity. This makes it possible to identify the relative importance of the terms governing the flow in the feeding channels and in the porous electrodes.

The characteristic velocity is denoted by U, while the characteristic length is denoted by L. These quantities are defined separately depending on the region considered. In the feeding channel, U represents the average tangential velocity in the channel and L represents the channel height. In the porous electrode, U represents the average velocity through the porous medium and L represents the porous electrode thickness.

The dimensional variables are scaled as follows:

$$\mathbf{x} = L\mathbf{x}^* \tag{3.41}$$

$$\mathbf{u} = U\mathbf{u}^* \tag{3.42}$$

$$t = \frac{L}{U}t^* \tag{3.43}$$

The pressure is non-dimensionalised with respect to the outlet pressure and to the pressure difference between the inlet and outlet sections:

$$p = p_{\text{out}} + \Delta p \, p^* \tag{3.44}$$

where

$$\Delta p = p_{\text{in}} - p_{\text{out}} \tag{3.45}$$

This scaling was adopted because the pressure variations analysed in the present work are directly associated with the pressure decrease developed along the computational domain.

The differential operators become:

$$\nabla = \frac{1}{L} \nabla^* \tag{3.46}$$

For the feeding channels, the dimensional momentum balance is written in tensorial form. After introducing the dimensionless variables, the dimensionless Navier–Stokes equation becomes:

$$\frac{\partial \mathbf{u}^*}{\partial t^*} + \left(\mathbf{u}^* \cdot \nabla^*\right) \mathbf{u}^* = -\text{Eu} \nabla^* p^* + \nabla^* \cdot \left[\frac{1}{\text{Re}} \left(\nabla^* \mathbf{u}^* + \left(\nabla^* \mathbf{u}^*\right)^T \right) \right] \tag{3.47}$$

where the local Reynolds number is defined as:

$$\text{Re} = \frac{\rho U L}{\mu} \tag{3.48}$$

and the Euler number is defined as:

$$\text{Eu} = \frac{\Delta p}{\rho U^2} \tag{3.49}$$

The Reynolds number is retained inside the divergence operator because the dynamic viscosity is evaluated locally and may vary throughout the computational domain as

a consequence of changes in gas composition. Consequently, the viscous contribution accounts for the spatial variation of the local gas properties rather than assuming a uniform reference viscosity.

The incompressible continuity equation becomes:

$$\nabla^* \cdot \mathbf{u}^* = 0 \tag{3.50}$$

For the porous electrode, the Brinkman formulation is non-dimensionalised using the characteristic quantities of the porous region. The porosity of the porous medium is denoted by ε_p, while the permeability is denoted by κ. Starting from the Brinkman equation adopted in the dimensional formulation, the dimensionless form can be written as:

$$\frac{1}{\varepsilon_p}\frac{\partial \mathbf{u}^*}{\partial t^*} + \frac{1}{\varepsilon_p^2}\left(\mathbf{u}^* \cdot \nabla^*\right)\mathbf{u}^* = -\mathrm{Eu}\nabla^* p^* + \frac{1}{\varepsilon_p}\nabla^* \cdot \left[\frac{1}{\mathrm{Re}}\left(\nabla^*\mathbf{u}^* + (\nabla^*\mathbf{u}^*)^T\right)\right] - \frac{1}{\mathrm{Re}\,\mathrm{Da}_\kappa}\mathbf{u}^* \tag{3.51}$$

where the Darcy number is:

$$\mathrm{Da}_\kappa = \frac{\kappa}{L^2} \tag{3.52}$$

In this formulation, the divergence term represents momentum diffusion within the porous medium and explicitly retains the spatial dependence of the local Reynolds number. The term multiplied by $1/(\mathrm{Re}\,\mathrm{Da}_\kappa)$ represents the Darcy resistance associated with the permeability of the porous electrode.

This formulation was applied separately to the anodic and cathodic compartments by using the corresponding characteristic quantities reported in the simulation parameters section. The characteristic velocity, characteristic length, pressure difference and local fluid properties were therefore evaluated independently for the feeding channel and porous electrode on each side of the cell.

The material balance for a generic species i, in non-stationary form, can be written as:

$$\frac{\partial c_i}{\partial t} + \mathbf{u} \cdot \nabla c_i = \nabla \cdot (D_{i,\text{eff}} \nabla c_i) + \nu_i R \tag{3.53}$$

where c_i is the concentration of species i, $\mathbf{u}$ is the velocity field, $D_{i,\text{eff}}$ is the effective diffusivity, R_i is the scalar reaction rate assuming a single reaction development (i.e., WGS) and ν_i is the stoichiometric coefficient of species i. The coefficient ν_i accounts for the role of the species in the reaction: it is negative for reactants consumed by the reaction and positive for products generated by the reaction.

The concentration of species i is non-dimensionalised using the inlet concentration of the j-th limiting reactant, $c_{j,\text{lim}}$, according to:

$$c_i = c_{j,\text{lim}} c_i^* \tag{3.54}$$

The dimensionless species balance can then be written as:

$$\frac{\partial c_i^*}{\partial t^*} + \mathbf{u}^* \cdot \nabla^* c_i^* = \nabla^* \cdot \left[\frac{1}{\text{Pe}_i} \nabla^* c_i^* \right] + \nu_i \text{Da}_\text{I} \tag{3.55}$$

where the local Peclet number and the local first Damköhler number are defined as:

$$\text{Pe}_i = \frac{UL}{D_{i,\text{eff}}} \tag{3.56}$$

and:

$$\text{Da}_\text{I} = \frac{RL}{U c_{j,\text{lim}}} \tag{3.57}$$

respectively, U being the characteristic velocity, L the characteristic length and $D_{i,\text{eff}}(\mathbf{x})$ the local effective diffusivity of species i.

The Peclet number compares convective transport with diffusive transport. High values of Pe indicate a dominant convective contribution, while low values indicate a more relevant diffusive contribution.

The first Damköhler number compares the characteristic rate of reaction with the characteristic rate of convective transport. In this formulation, a local Damköhler number

is introduced because the reaction rate can vary within the computational domain. Therefore, Da_I provides a pointwise measure of the relative importance between the local reaction rate and the convective supply of the limiting reactant. Overall, non-dimensionalization makes it possible to interpret the behaviour of the MCFC through synthetic parameters that express the relative role of the physical phenomena involved. This formulation is useful for comparing the different collector geometries, since it links variations in the flow field and species distribution to the dominant mechanisms in the channel, in the porous medium and near the electrochemically active interface.

3.5 COMSOL Multiphysics Implementation

The mathematical formulation described in the previous sections was implemented numerically using COMSOL Multiphysics, a computational environment based on the finite element method and suitable for solving coupled problems involving different physical phenomena. In the present case, the problem simultaneously involves the motion of the gas mixture, the transport of chemical species, the presence of porous regions, the Water Gas Shift reaction in the anodic domain and the local electrochemical response of the cell.

The finite element method is based on the discretization of the continuous domain into a finite number of elementary subdomains, called elements. Within each element, the unknown variables of the problem, such as velocity, pressure and species concentration, are approximated by means of suitable shape functions. In this way, the differential equations describing the physical problem are transformed into an algebraic system that can be solved numerically.

This approach is particularly useful because the MCFC domain presents complex geometries due to the presence of current collectors and porous electrode regions. The analysed configurations are not reducible to simple one-dimensional or two-dimensional geometries, but require a three-dimensional description capable of representing openings, obstacles, local variations of the flow cross-section and interfaces between different physical domains.

In the numerical model, the MCFC was schematized by considering the region available

for gas passage above the porous electrode and inside the current collector volume. This control volume represents the fluid domain in which the gas mixture flows before partially penetrating the porous electrode. Three configurations were considered: the ideal free channel, the traditional current collector and the proposed grooved current collector. The free channel represents the limiting case in which no internal obstruction is present, while the other two configurations introduce different degrees of geometrical obstruction and electrode shielding.

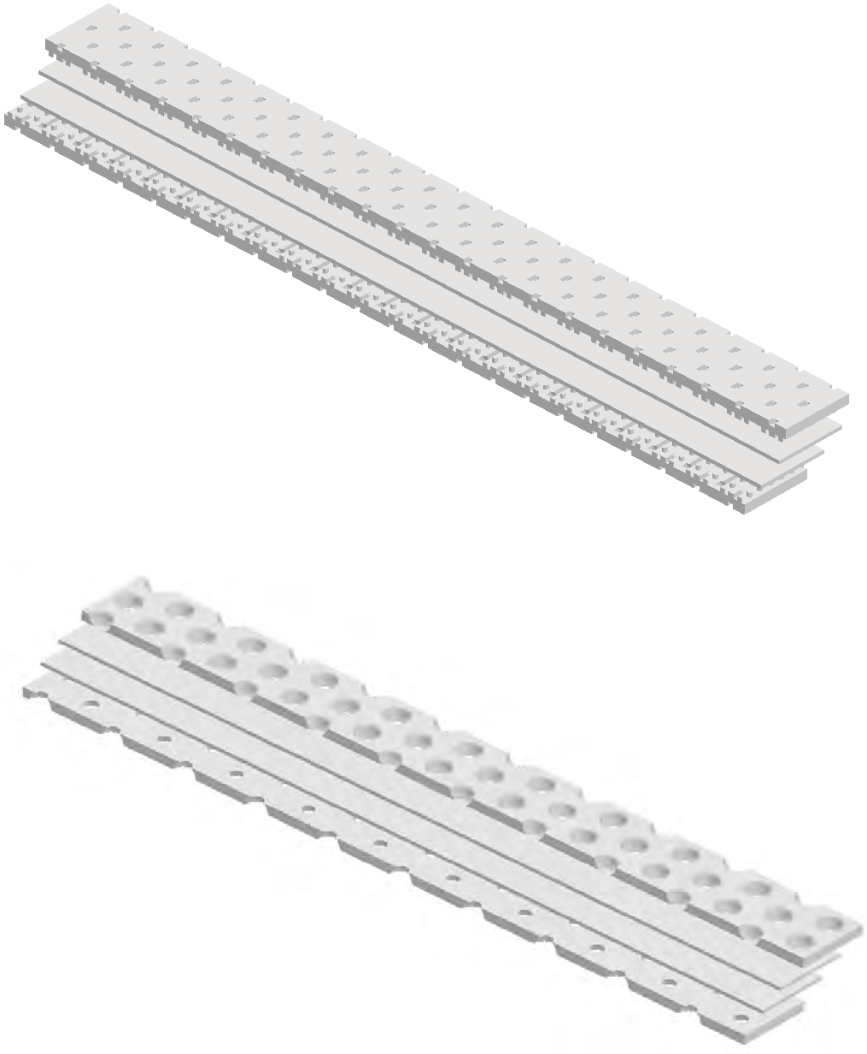

Figure 3.3: Exploded views of the fluid domains implemented in COMSOL Multiphysics for the traditional and grooved current collector configurations, from top to bottom.

The numerical solution was obtained through a stationary study, assuming that the variables of the problem do not explicitly depend on time under the analysed operating conditions. This choice makes it possible to determine the steady-state distribution of

velocity, pressure, concentrations and local current density.

The geometric domain was discretized using an unstructured mesh made of tetrahedral elements. This choice is motivated by the complexity of the considered geometries, in particular by the presence of current collectors and openings through which the gas comes into contact with the electrode surface. Tetrahedral elements allow the discretization to adapt to the shape of the three-dimensional domain, making it easier to describe complex and non-regular regions, as shown in Figure 3.4.

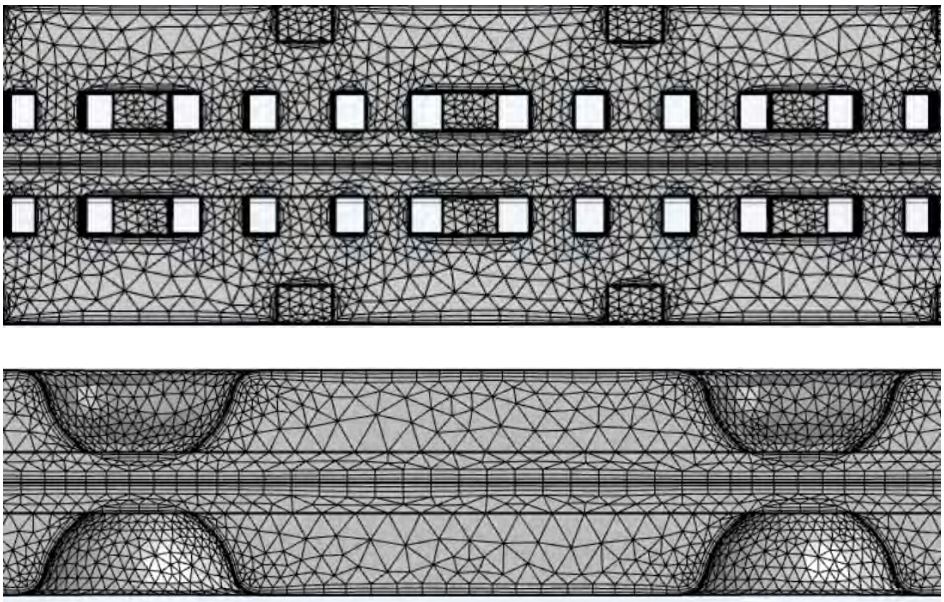

Figure 3.4: Magnified views of the computational meshes adopted for the traditional and grooved current collector configurations, from top to bottom, showing the local mesh discretisation in greater detail.

The mesh was constructed with particular attention to the zones where greater variations in physical quantities are expected. Local refinement is therefore required near the solid obstacles of the collector, the surfaces in contact with the gas, the interface between the channel and the porous electrode and the electrode/matrix interface.

The formulation was translated into COMSOL through the assignment of distinct physical domains. The model includes free-fluid regions, corresponding to the feeding channels and to the spaces available around the current collectors, and porous regions, corresponding to the anodic and cathodic electrodes.

In the free domains, the flow field of the gas mixture was described using the Navier–Stokes equation. This equation makes it possible to determine the velocity and pressure

distribution in the channel, highlighting the effect of the collector geometry on flow direction, local accelerations, possible stagnation zones and overall pressure drop.

In the porous domains, the motion of the gas mixture was described using the Brinkman formulation. This makes it possible to represent the resistance opposed by the electrode to gas flow through an equivalent permeability of the porous medium. The use of the Brinkman formulation is particularly suitable in this work because it allows the transition between the free-flow domain and the porous electrode to be described within the same numerical framework.

The transport of chemical species was implemented both in the channels and in the porous media through material balances for the considered species. In the anodic compartment, the species H_2, H_2O, CO and CO_2 were considered, representative of a fuel mixture derived from reforming processes. In the cathodic compartment, the species O_2, CO_2 and possible inert species were considered, representative of an oxidizing stream containing carbon dioxide.

In the porous layers, species diffusivity was introduced by taking into account the reduction in transport due to porosity, tortuosity and the contribution of Knudsen diffusion. This choice allows for a more realistic representation of species transport inside the electrodes than a purely molecular diffusion description.

In the anodic domain, the Water Gas Shift reaction was implemented as an equilibrium reaction, consistently with the formulation described previously. The equilibrium condition was applied both in the channel/interconnect region and inside the porous anode, in order to account for the local redistribution of CO, H_2O, CO_2 and H_2 before and during gas penetration through the porous electrode. In this way, the anodic gas composition was adjusted according to the temperature-dependent equilibrium constant of the WGS reaction, influencing the local hydrogen availability for the anodic electrochemical reaction.

The electrochemical reactions were localized at the interface between electrode and matrix. In this region, the local compositions and partial pressures required to calculate the equilibrium potential through the Nernst relation are evaluated. The local current density is then calculated using the kinetic model described previously.

The stationary solution makes it possible to evaluate quantities such as velocity field,

pressure distribution, concentration distribution, Nernst potential, total equivalent resistance and local current density. These variables constitute the main indicators used to compare the fluid-dynamic and electrochemical performance of the analysed geometries.

Chapter 4

Results and Discussion

This chapter presents the numerical results obtained from the analysis of the current collector configurations described in Chapter 3. The main focus is placed on the proposed grooved current collector, which was developed with the aim of improving the interaction between the gas streams and the porous electrodes by reducing the geometrical shielding effect.

The traditional current collector is first considered as the reference configuration. The grooved geometry is then analysed in detail in terms of pressure distribution, local flow redistribution and gas penetration towards the porous electrodes. Particular attention is devoted to the effect of the embossments on the streamwise and vertical velocity fields and to the fluid-dynamic mechanisms governing transport at the channel–porous interface.

The chapter subsequently discusses species transport and electrochemical behaviour. The concentration and convective–diffusive transport fields are used to clarify how the reacting species are supplied through the porous electrodes towards the reactive surfaces, while the current density distribution is interpreted as the final response of the coupled fluid-dynamic, mass-transport and electrochemical phenomena.

Finally, the traditional and grooved current collectors are directly compared in terms of hydraulic and electrochemical performance. A preliminary structural assessment is also presented to evaluate the effect of the collector geometry on stress and contact-pressure redistribution under stack compression.

All configurations were analysed under the same operating conditions and using the same porous-medium and electrochemical formulations. This approach was adopted to isolate the influence of the current collector geometry on the overall behaviour of the system.

4.1 Simulation Parameters

Before discussing the numerical results, the main geometrical, operating and modelling parameters adopted in the simulations are summarised. These parameters define the computational domain, the gas-feeding conditions, the porous-medium properties and the reference quantities used for the dimensional analysis of the problem.

A Cartesian coordinate system was adopted throughout the numerical analysis. The x direction corresponds to the axial direction and to the main gas-flow direction along the cell length. The y direction represents the vertical coordinate across the feeding channel and the porous-electrode thickness, whereas the z direction identifies the transverse coordinate across the modelled cell width.

The corresponding dimensionless coordinates are defined as

$$x^* = \frac{x}{L}, \qquad y^* = \frac{y}{L}, \qquad z^* = \frac{z}{L}, \tag{4.1}$$

where L is the characteristic length associated with the region considered, as defined in the non-dimensional formulation.

The computational domain represents a portion of the MCFC cell in the transverse z direction rather than the complete cell width. The full axial length of the cell, equal to 130 mm, was considered along the x direction. This choice was adopted because the pressure drop along the main flow direction is one of the quantities of interest in the present analysis and because the length scales of the processes associated with the interactions between the pore flow and the channel flow are unknown.

Conversely, only a representative width of the cell was modelled along the (spanwise) z direction, equal to 13 mm, namely the width of the minimal periodic pattern of the current-collector. Hence, periodic boundary conditions were imposed in the spanwise

direction.

This modelling strategy reduces the computational cost while preserving the complete axial development of the flow field and the pressure losses along the gas path.

The main geometrical and operating parameters adopted in the numerical simulations are reported in Table 4.1.

Table 4.1: Main geometrical, operating and porous-medium parameters adopted in the numerical simulations.

Parameter	**Symbol**	**Value**	**Unit**
Modelled cell length	L_{cell}	130.00	mm
Modelled cell width	W_{cell}	13.00	mm
Channel height	H_{ch}	1.61	mm
Porous electrode thickness	s_{el}	0.67	mm
Porous-medium porosity	ε	0.60	–
Mean pore diameter	d_p	5	μm
Current-collector thickness	s_{cc}	0.80	mm
Inlet anode gas velocity	$u_{\mathrm{a,in}}$	0.80	$\mathrm{m\,s^{-1}}$
Inlet cathode gas velocity	$u_{\mathrm{c,in}}$	1.50	$\mathrm{m\,s^{-1}}$
Operating temperature	T	923.15	K
Outlet pressure	p_{out}	101325	Pa
Cell voltage	V_{cell}	0.80	V

The values reported in Table 4.1 were kept constant for all analysed configurations. Therefore, the differences observed in the velocity field, pressure distribution, species transport and current density are mainly related to the different geometrical arrangement of each studied collector.

The same porous-medium properties were adopted for the anodic and cathodic electrodes. In particular, the porous electrode thickness was set equal to 0.67 mm and the porosity was set equal to $\varepsilon = 0.60$, consistently with the reference values reported for KIST-based MCFC cells [40]. The representative pore diameter was assumed equal to 5 μm, in agreement with the value reported for MCFC nickel anodes in [41]. The current-collector thickness was selected consistently with the reference geometry adopted for the numerical comparison [5].

It is important to specify that the porosity used in the numerical model refers to the gas-accessible porous domain and does not explicitly account for the presence of molten

carbonate electrolyte inside the pores. In real MCFC electrodes, part of the pore volume is occupied by the electrolyte; therefore, the effective porosity available for gas transport is expected to be lower. The gas-accessible porosity under real operating conditions depends on several factors, such as electrolyte filling, electrode microstructure and operating conditions.

Referring to the fed gases reported in Table 4.2, the anodic inlet composition was selected to represent a typical syngas stream obtained at the outlet of a reformer operating at approximately 900 °C with a steam-to-carbon ratio equal to 4. This mixture contains the main species involved in the anodic compartment, namely H_2, H_2O, CO and CO_2.

The cathodic inlet composition was instead selected to represent an oxidising stream comparable to a combustion exhaust gas, containing oxygen, carbon dioxide, steam and nitrogen as an inert species. The two compartments therefore differ in inlet velocity, gas composition and reaction stoichiometry.

Table 4.2: Inlet gas compositions adopted in the numerical simulations.

Compartment	**Species**	**Molar fraction**
Anode	H_2	0.46
Anode	H_2O	0.34
Anode	CO	0.11
Anode	CO_2	0.09
Cathode	O_2	0.15
Cathode	CO_2	0.10
Cathode	N_2	0.70
Cathode	H_2O	0.05

The non-dimensional formulation adopted in the model was based on reference quantities evaluated separately for the anodic and cathodic compartments. Since the gas mixtures were treated as incompressible in the fluid-dynamic model, a single reference density was adopted for each compartment. Therefore, the same density value was used for both the feeding channel and the porous electrode on the same side of the cell.

The reference quantities were obtained from the free-channel case, which was used as a neutral configuration not affected by the geometrical obstruction introduced by the traditional or grooved current collectors. For the feeding channel, the characteristic

velocity was defined as the average streamwise velocity component along the main flow direction. For the porous electrode, the characteristic velocity was defined as the average vertical velocity component through the porous layer, evaluated at the centre of the channel. The pressure variation used for the scaling was taken as the pressure drop of the corresponding free-channel simulation. Finally, the reference concentration was selected as the feeding-channel inlet concentration of the limiting reactant: H_2 for the anode and CO_2 for the cathode.

The reference quantities adopted for the non-dimensionalisation of the anodic and cathodic sides are reported in Table 4.3 and Table 4.4, respectively. The numerical values are reported using four significant figures to ensure a consistent representation of quantities characterised by different orders of magnitude.

Table 4.3: Reference quantities used for the non-dimensionalisation of the anodic side.

Region	**Reference quantity**	**Value**	**Unit**
Feeding channel	Characteristic length, $L_{\mathrm{a,ch}}$	1.610×10^{-3}	m
Feeding channel	Average streamwise velocity, $U_{\mathrm{a,ch}}$	1.065	$\mathrm{m\,s^{-1}}$
Feeding channel	Reference density, ρ_{a}	0.186	$\mathrm{kg\,m^{-3}}$
Feeding channel	Reference pressure drop, $\Delta p_{\mathrm{a,ch}}$	18.500	Pa
Feeding channel	Reference concentration, $c_{\mathrm{H_2,a,lim}}$	6.074	$\mathrm{mol\,m^{-3}}$
Feeding channel	Characteristic time, $L_{\mathrm{a,ch}}/U_{\mathrm{a,ch}}$	1.587×10^{-3}	s
Porous electrode	Characteristic length, $L_{\mathrm{a,p}}$	6.700×10^{-4}	m
Porous electrode	Average vertical velocity, $U_{\mathrm{a,p}}$	2.352×10^{-3}	$\mathrm{m\,s^{-1}}$
Porous electrode	Reference density, ρ_{a}	0.186	$\mathrm{kg\,m^{-3}}$
Porous electrode	Reference pressure variation, $\Delta p_{\mathrm{a,p}}$	18.500	Pa
Porous electrode	Reference concentration, $c_{\mathrm{H_2,a,lim}}$	6.074	$\mathrm{mol\,m^{-3}}$
Porous electrode	Characteristic time, $L_{\mathrm{a,p}}/U_{\mathrm{a,p}}$	2.848×10^{-1}	s

The parameters required for the electrochemical model were re-parametrised with respect to the reference kinetic formulation proposed by Audasso, Bosio and Nam [39]. Since the formulation implemented in COMSOL is based on local interfacial quantities, the parameters were made consistent with the variables calculated at the electrode–matrix interface.

A free-channel configuration was used during the parameter-identification step in order

Table 4.4: Reference quantities used for the non-dimensionalisation of the cathodic side.

Region	**Reference quantity**	**Value**	**Unit**
Feeding channel	Characteristic length, $L_{\mathrm{c,ch}}$	1.610×10^{-3}	m
Feeding channel	Average streamwise velocity, $U_{\mathrm{c,ch}}$	1.392	$\mathrm{m\,s^{-1}}$
Feeding channel	Reference density, ρ_{c}	0.392	$\mathrm{kg\,m^{-3}}$
Feeding channel	Reference pressure drop, $\Delta p_{\mathrm{c,ch}}$	34.750	Pa
Feeding channel	Reference concentration, $c_{\mathrm{CO_2,c,lim}}$	1.321	$\mathrm{mol\,m^{-3}}$
Feeding channel	Characteristic time, $L_{\mathrm{c,ch}}/U_{\mathrm{c,ch}}$	1.214×10^{-3}	s
Porous electrode	Characteristic length, $L_{\mathrm{c,p}}$	6.700×10^{-4}	m
Porous electrode	Average vertical velocity, $U_{\mathrm{c,p}}$	1.248×10^{-3}	$\mathrm{m\,s^{-1}}$
Porous electrode	Reference density, ρ_{c}	0.392	$\mathrm{kg\,m^{-3}}$
Porous electrode	Reference pressure variation, $\Delta p_{\mathrm{c,p}}$	34.750	Pa
Porous electrode	Reference concentration, $c_{\mathrm{CO_2,c,lim}}$	1.321	$\mathrm{mol\,m^{-3}}$
Porous electrode	Characteristic time, $L_{\mathrm{c,p}}/U_{\mathrm{c,p}}$	5.370×10^{-1}	s

to avoid the influence of a specific current-collector geometry on the fitted kinetic parameters. MCFC literature data on polarisation curves at the working conditions reported in Table 4.1 and Table 4.2 were taken as reference.

The re-parametrisation reproduced the reference polarisation data with a coefficient of determination of approximately $R^2 = 0.82$. This indicates that the fitted model captures the main trend of the reference polarisation behaviour within the investigated operating range. The re-parametrised parameters adopted in the equivalent resistance model are reported in Table 4.5.

Table 4.5: Re-parametrised parameters adopted in the electrochemical resistance model.

Parameter	**Description**	**Value**	**Unit**
P_1	Ohmic resistance pre-exponential parameter	0.01382	$\Omega\,\mathrm{cm}^2$
P_2	Ohmic resistance temperature parameter	3054	K
P_3	Cathodic CO_2 resistance parameter	6.70×10^{-6}	$\Omega\,\mathrm{cm}^2\,\mathrm{K}^{-1}\,\mathrm{atm}$
P_4	Cathodic CO_2 temperature parameter	2743	K
P_5	Cathodic O_2 resistance parameter	2.61×10^{-10}	$\Omega\,\mathrm{cm}^2\,\mathrm{K}^{-1}\,\mathrm{atm}^{-1/2}$
P_6	Cathodic O_2 temperature parameter	10036	K
P_7	Anodic H_2 resistance parameter	2.19×10^{-5}	$\Omega\,\mathrm{cm}^2\,\mathrm{K}^{-1}\,\mathrm{atm}$
P_8	Anodic H_2 temperature parameter	9362	K

4.2 Traditional Current Collector

This and the following sections present the numerical results obtained for the analysed current-collector configurations. Unless otherwise specified, axial results are reported as a function of the dimensionless axial coordinate x^*, while local profiles are presented using the dimensionless coordinate corresponding to the selected extraction direction.

The traditional current collector is adopted in the present work as the reference configuration representative of a conventional industrial solution. Its fluid-dynamic and electrochemical behaviour is first analysed in order to provide a baseline for the subsequent discussion of the grooved geometry. Although the local transport mechanisms are investigated in greater detail for the proposed collector, the traditional configuration must first be characterised because its geometry determines a markedly different gas distribution between the feeding channel and the porous electrode. In the traditional current collector, communication between the main gas channel and the porous electrode occurs through discrete openings defined by the arched structure. A detailed view of the collector geometry is reported in Figure 4.1, where the local openings beneath the arches and the passages through which the gas can move from the channel towards the porous electrode are highlighted.

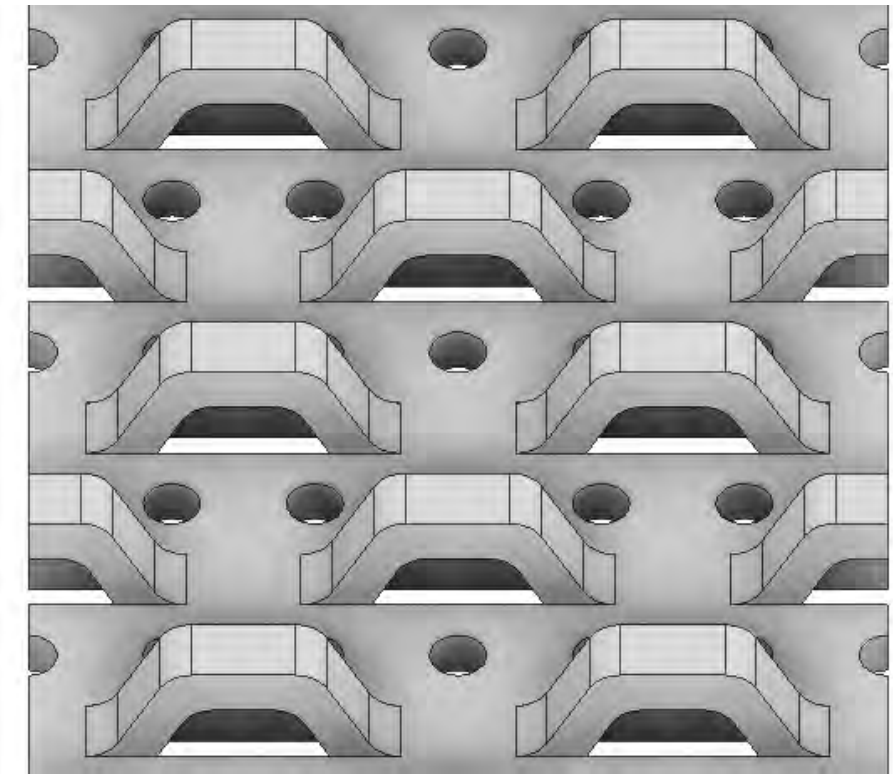

Figure 4.1: Detail of the traditional current collector geometry, shown as a zoomed view of the region highlighted in Figure 3.1. The figure emphasizes the local openings through which the gas passes from the main channel towards the porous electrode.

Consequently, the gas cannot access the porous layer uniformly over the entire projected area. Instead, the flow is periodically redirected through the available passages, while the solid portions of the collector locally screen the porous electrode from the main gas stream.

The results for the traditional geometry are therefore discussed by first considering the section-averaged pressure evolution along the feeding channels. The streamwise velocity field is then analysed along selected lines defined on an xz plane located at the mid-height of the feeding channel, in order to identify the local redistribution caused by the arched geometry. Finally, local profiles along the vertical y direction are extracted at representative openings to examine separately the streamwise motion in the channel and the streamwise and through-plane velocity components inside the porous electrode.

4.2.1 Section-Averaged Pressure along the Feeding Channels

The global hydraulic behaviour of the traditional collector was evaluated through the section-averaged pressure along the main flow direction. Pressure was averaged over sections normal to the axial direction, so that each point of the resulting profile represents the mean pressure over the corresponding channel cross-section.

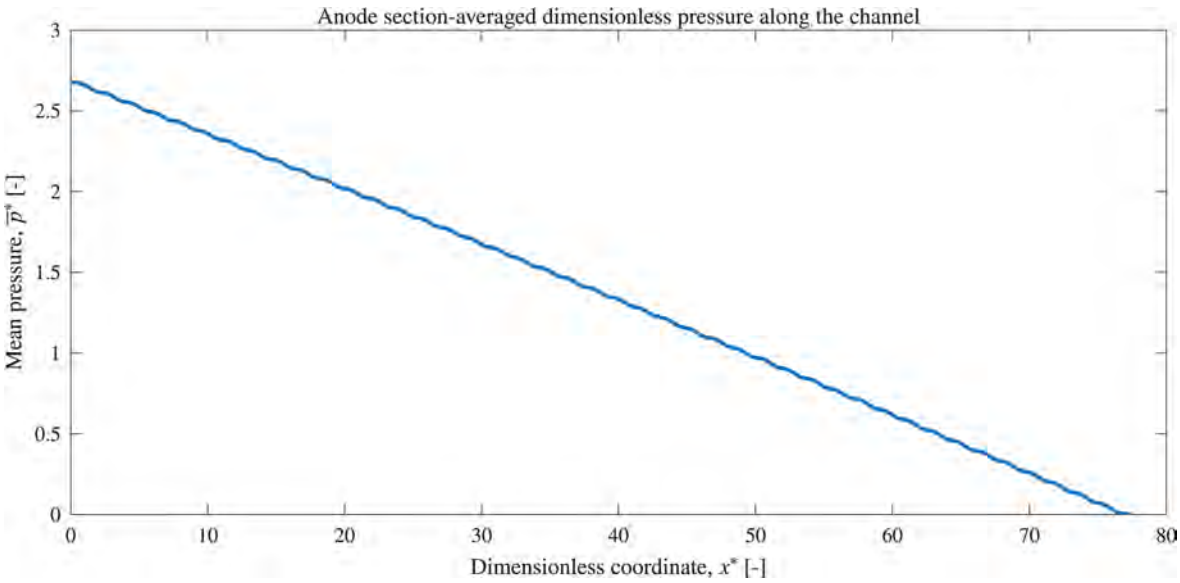

Figure 4.2: Section-averaged dimensionless pressure along the anodic feeding channel for the traditional current collector.

The anodic dimensionless pressure profile reported in Figure 4.2 shows an almost monotonic decrease from inlet to outlet. The global trend is substantially linear, indicating that pressure losses progressively accumulate along the entire channel length.

Small periodic fluctuations are superimposed on the mean pressure decrease. Their amplitude is considerably smaller than the global axial variation, but their regular spacing reflects the repeated geometrical structure of the traditional current collector. As the gas encounters successive arched elements and the corresponding open passages, the local hydraulic resistance changes periodically.

Since pressure is averaged over the entire channel cross-section, these local perturbations are partially smoothed and appear as small oscillations around the dominant axial trend. The absence of significant pressure-recovery regions indicates that the hydraulic losses associated with the repeated interaction between the gas and the collector structure accumulate progressively along the main flow direction.

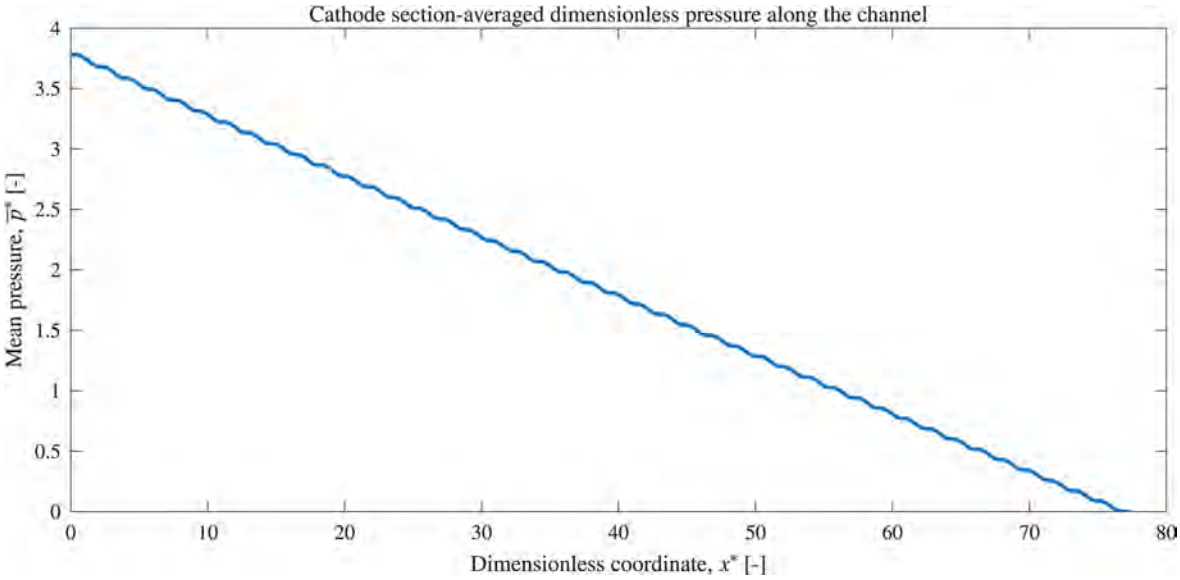

Figure 4.3: Section-averaged dimensionless pressure along the cathodic feeding channel for the traditional current collector.

The cathodic dimensionless pressure profile reported in Figure 4.3 exhibits the same overall behaviour. The mean pressure decreases progressively along the axial direction, while small periodic perturbations remain visible along the profile.

The cathodic side exhibits a larger pressure variation than the anodic compartment, consistently with the different feeding conditions and the higher cathodic gas velocity. Nevertheless, the qualitative pressure evolution remains similar on both sides of the cell.

The traditional current collector can therefore be interpreted as a distributed hydraulic resistance acting along the axial gas path. However, the section-averaged pressure profiles do not provide direct information on the local redistribution of the gas around the arched elements. For this reason, the streamwise velocity field was subsequently analysed along the selected lines on an xz plane located at the mid-height of the feeding channel shown in Figure 4.4.

4.2.2 Streamwise Velocity Redistribution in the Channel Mid-Plane

The local redistribution of the streamwise velocity was investigated on an xz plane located at the mid-height of the feeding channel. The plane was positioned halfway

between the upper channel boundary and the channel–porous interface.

The choice of this plane was made to reduce the direct influence of the cross-stream boundary regions on the extracted streamwise velocity profiles. At the upper solid wall, the no-slip boundary condition causes the gas velocity to vanish. In the lower portion of the feeding channel, the velocity field is influenced by the coupling with the porous electrode and by the resistance to flow within the porous domain.

Consequently, profiles extracted close to either the upper wall or the channel–porous interface would be strongly influenced by the corresponding local boundary behaviour. By selecting the mid-height of the feeding channel, the analysis focuses on the free-flow region where the streamwise velocity is more representative of the redistribution induced by the current-collector geometry.

The dimensionless streamwise velocity u^* was extracted along two representative lines defined on the selected xz plane. Their locations are shown in Figure 4.4. Line (a) is oriented along the spanwise direction, corresponding to the z coordinate, whereas line (b) is oriented along the streamwise direction, corresponding to the x coordinate. The two lines were selected to cross regions differently affected by the repeated arched geometry.

In Figure 4.4, the rectangular regions correspond to the intersection between the selected xz cutting plane and the solid arched elements of the traditional current collector. Therefore, they do not represent additional fluid regions, but the solid cross-sections of the arches intercepted by the plane. Since the figure is a top view of the extraction plane, the repeated arched geometry appears as a regular sequence of solid sections distributed around the selected extraction lines.

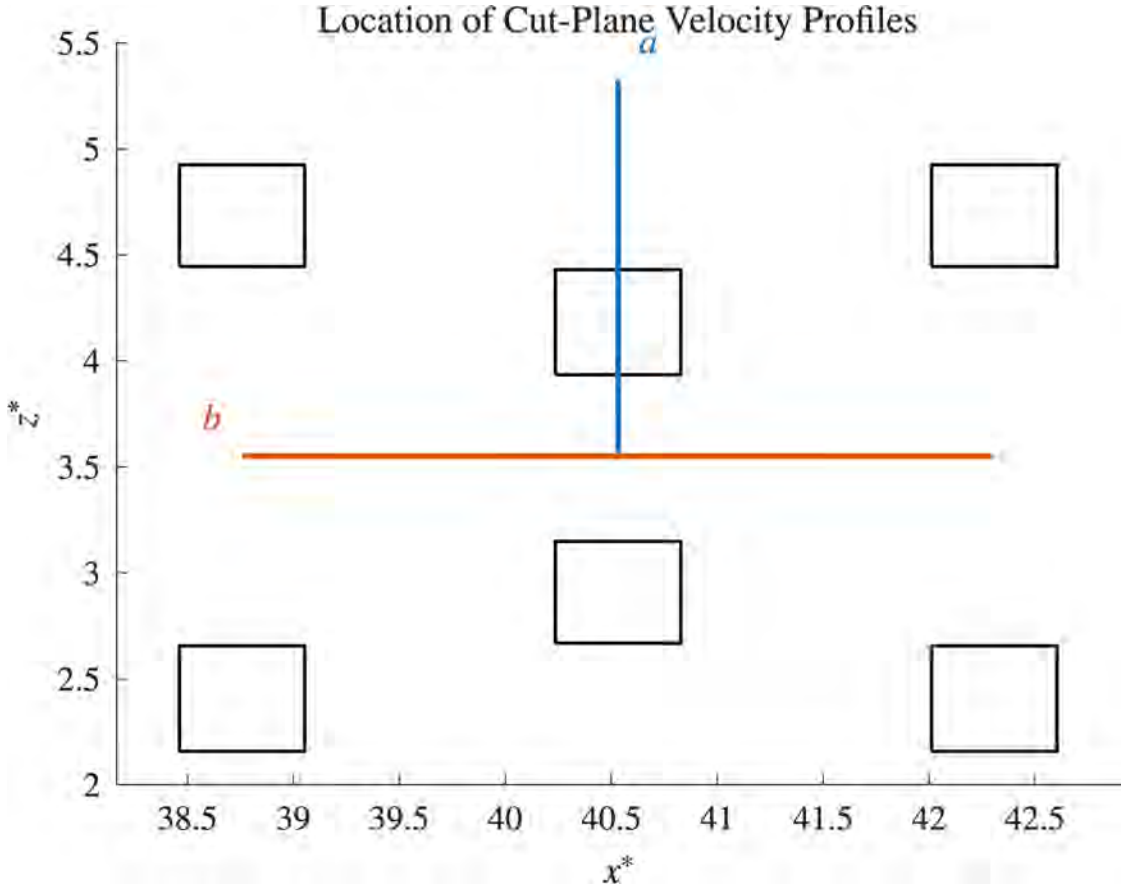

Figure 4.4: Location of the spanwise line (a) and streamwise line (b) used to extract the streamwise velocity profiles on the xz plane at the mid-height of the feeding channel for the traditional current collector. The rectangular regions represent the solid sections of the arched collector elements intersected by the cutting plane.

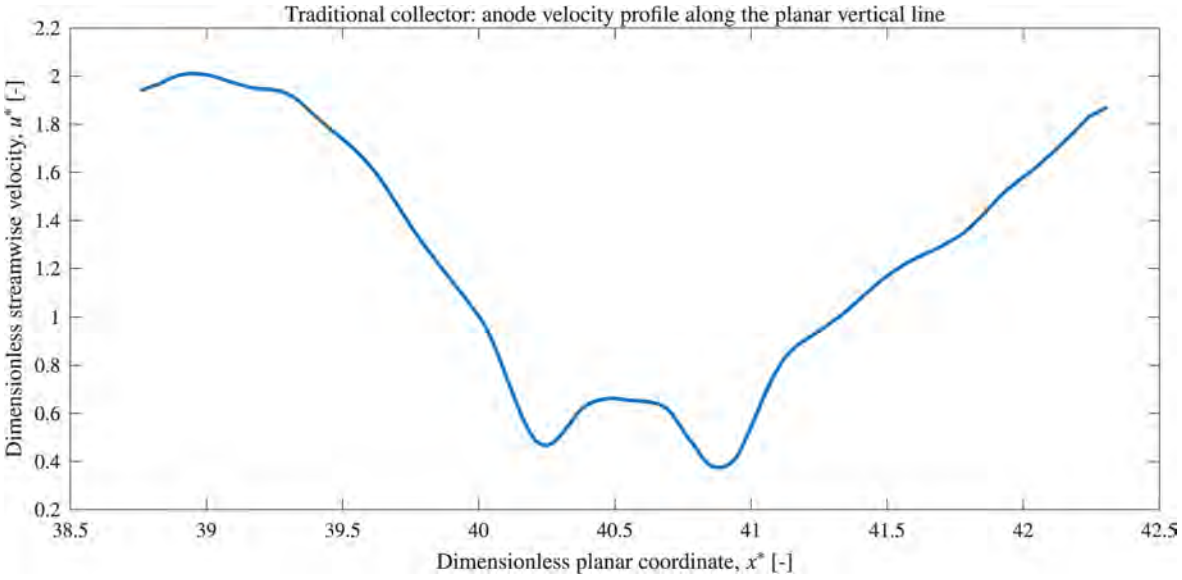

Figure 4.5: Dimensionless anodic streamwise velocity extracted along the streamwise line (b) for the traditional current collector.

The anodic velocity profile along the streamwise line (b), reported in Figure 4.5, is strongly non-uniform and exhibits a broad reduction in streamwise velocity within the central portion of the selected line.

The highest values are observed in the regions less influenced by the current-collector geometry. Moving along the selected streamwise path, the velocity decreases markedly and reaches a first local minimum as the flow enters the region affected by the arched element. A partial velocity recovery is subsequently observed, producing a local maximum approximately centred with respect to the collector element, before the streamwise velocity decreases again towards a second minimum near the opposite side of the arch-influenced region.

The two local minima can therefore be associated with the upstream and downstream interaction regions of the repeated arched geometry. Between them, the local increase in streamwise velocity reflects the redistribution of the gas along the axial direction within the central portion of the available flow path. The subsequent reduction indicates the influence of the solid collector geometry as the flow approaches the opposite side of the arched element.

The presence of this sequence of minimum–maximum–minimum values demonstrates that the velocity disturbance generated by the traditional collector is not confined to the immediate vicinity of the solid structure. The arches modify the available flow paths and generate shear layers, resulting in non-uniform streamwise transport.

Towards the opposite side of the profile, the streamwise velocity progressively increases again as the extraction line approaches a region less affected by the current collector.

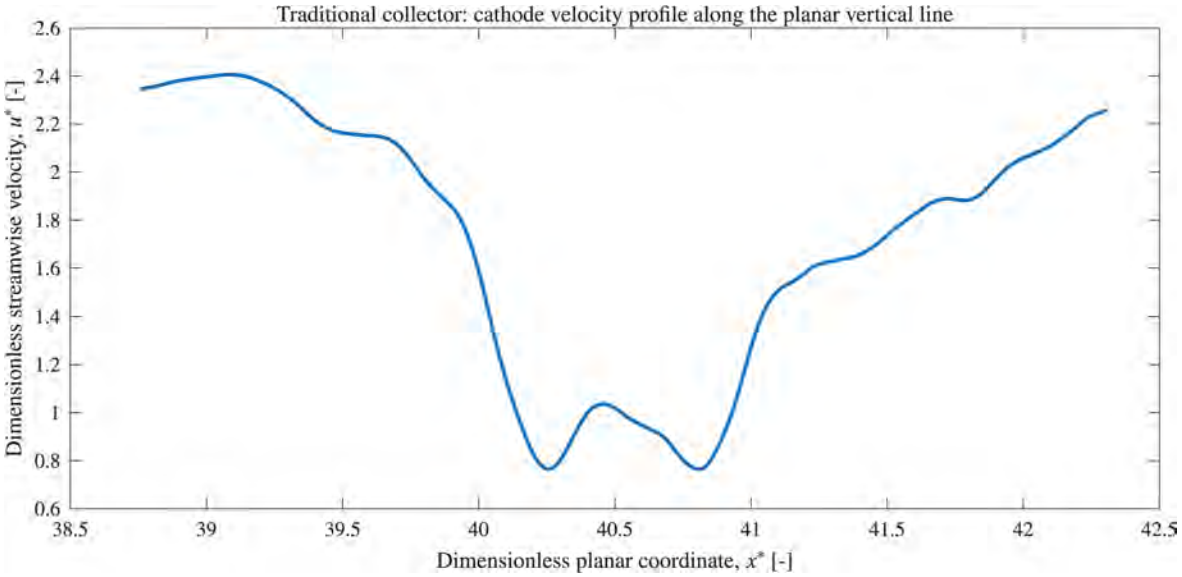

Figure 4.6: Dimensionless cathodic streamwise velocity extracted along the streamwise line (b) for the traditional current collector.

The cathodic profile reported in Figure 4.6 exhibits the same general spatial distribution. A marked velocity reduction is again observed in the central region, with two local minima located near the upstream and downstream interaction regions of the arched element and a partial recovery between them.

The higher cathodic flow intensity increases the magnitude of the local velocity variations and amplifies the contrast between the regions less affected by the collector and those directly influenced by the arched structure.

The similarity between the anodic and cathodic profiles confirms that the spatial redistribution of the streamwise velocity is primarily controlled by the collector topology, which is essentially identical.

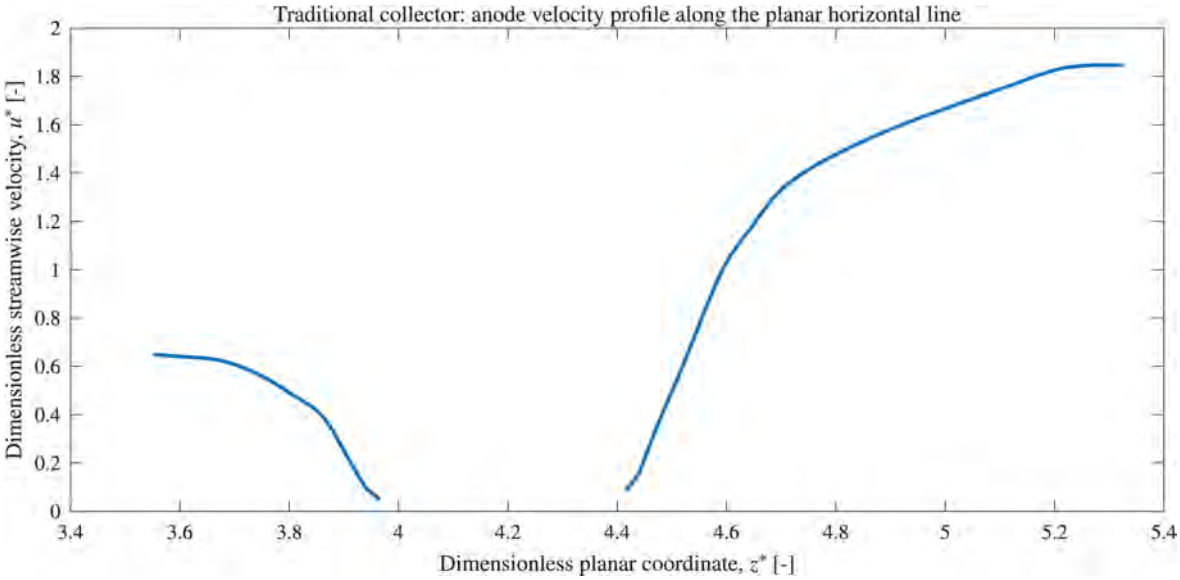

Figure 4.7: Dimensionless anodic streamwise velocity extracted along the spanwise line (a) for the traditional current collector.

The anodic profile along the spanwise line (a), reported in Figure 4.7, provides a complementary view of the local flow redistribution across the z direction.

The velocity profile is divided into two separate fluid regions. The discontinuity between the two portions does not indicate a reversal of the streamwise velocity component. Instead, it corresponds to the solid region occupied by the arched collector element intersected by the extraction line. Since the velocity field is defined only within the fluid domain, no velocity value is available where line (a) crosses the solid arch.

On both sides of the solid element, the streamwise velocity remains positive. In the first fluid region, u^* progressively decreases as the extraction line approaches the wall of the arch. The velocity reaches a value close to zero near the solid boundary, consistently with the no-slip condition imposed on the collector surface.

A corresponding behaviour is observed on the opposite side of the arch. Starting close to the solid boundary, the streamwise velocity is initially low and progressively increases as the distance from the collector wall increases. The gas therefore recovers the main axial motion when moving away from the solid element and towards the less obstructed portion of the feeding channel.

The profile clearly shows that the arched element strongly modifies the local streamwise velocity distribution. The reduction of u^* on both sides of the collector is primarily

associated with the near-wall velocity damping imposed by the no-slip condition, while the progressive increase away from the arch reflects the recovery of the main channel flow.

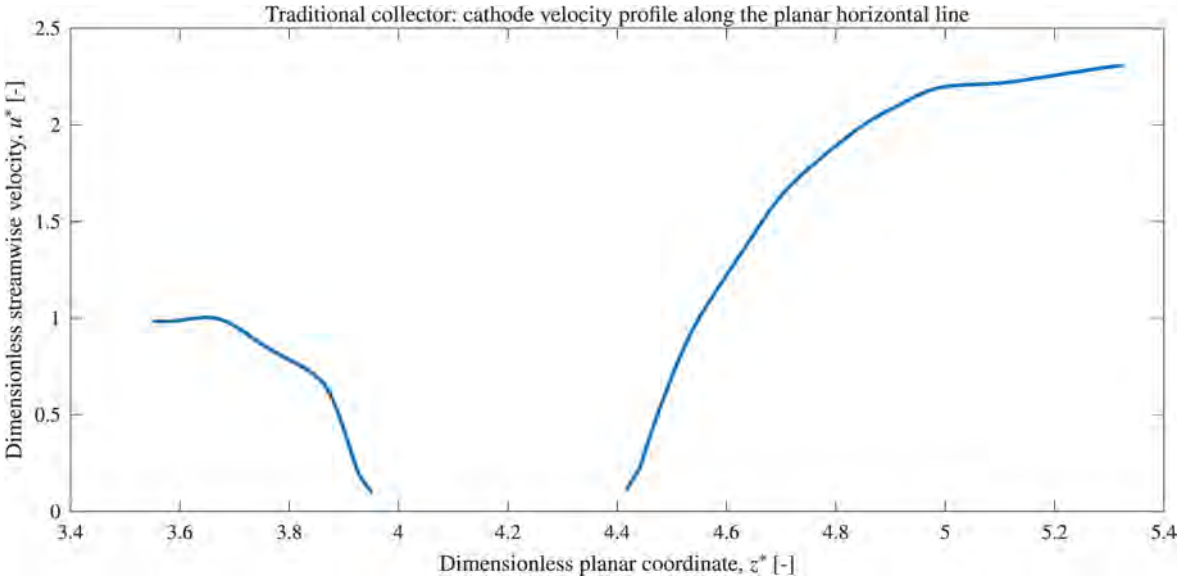

Figure 4.8: Dimensionless cathodic streamwise velocity extracted along the spanwise line (a) for the traditional current collector.

The corresponding cathodic profile shown in Figure 4.8 exhibits the same general structure observed on the anodic side. The two fluid portions are again separated by the solid arched element crossed by line (a), where the streamwise velocity is not defined.

As already discussed for the anodic profile, u^* remains positive in both fluid regions and decreases near the collector walls because of the no-slip condition. The higher cathodic flow intensity mainly increases the dimensionless velocity values reached in the less obstructed regions, without modifying the underlying physical mechanism.

The planar velocity profiles therefore identify the direct influence of the solid collector geometry on the local gas distribution. Along the spanwise line (a), the arched element interrupts the fluid domain and generates pronounced near-wall velocity reductions on both sides of the solid structure. Together with the streamwise profiles along line (b), these results demonstrate that the traditional collector constrains the gas through discrete flow passages and produces a strongly non-uniform streamwise velocity distribution.

To determine how this local redistribution is transmitted through the porous electrode, the velocity field was subsequently analysed along the cross-stream y direction.

4.2.3 Local Velocity Profiles through Representative Openings

The local transition from the feeding channel to the porous electrode was analysed along lines oriented in the cross-stream y direction and passing through representative openings of the traditional current collector. The extraction profiles extend over the complete feeding-channel height, from the upper solid wall to the channel–porous interface, and subsequently through the porous electrode towards the electrode–matrix interface.

At the upper channel wall, the no-slip boundary condition requires the gas velocity to approach zero. The streamwise velocity profiles extracted along y can therefore be interpreted by considering both the near-wall velocity damping and the local flow redistribution generated by the current-collector geometry. At the channel–porous interface, the flow instead transitions from the free-fluid domain to the highly resistive porous electrode.

Two representative locations were considered. The first cross-stream line was positioned through an opening located at the side of an arch and is hereafter referred to as the *arc-side point*. The second line was positioned through an opening located downstream of the arch and laterally displaced with respect to the centre of the arched element. This position is referred to as the *behind-arc point*.

The two positions were selected to compare a region more directly connected to the incoming gas flow with a region affected by the shielding produced by the collector. Their locations are shown in Figure 4.9.

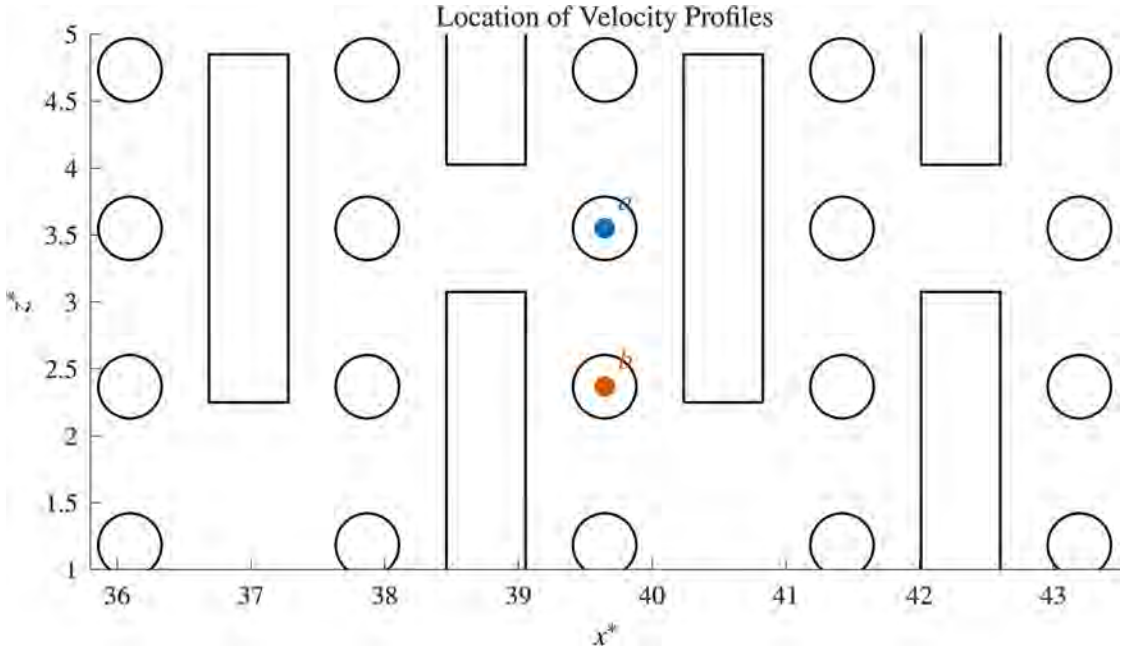

Figure 4.9: Location of the arc-side point (a) and behind-arc point (b) used for the extraction of the local velocity profiles along the cross-stream y direction.

The streamwise velocity in the feeding channel was first analysed to determine how the axial gas motion approaches each opening. The streamwise and cross-stream velocity components inside the porous electrode were then considered separately.

For clarity, different local cross-stream coordinates were used for the channel and porous-medium profiles. For the feeding-channel profiles, the vertical coordinate was shifted with respect to the channel–porous electrode interface. Therefore, the origin corresponds to the interface and the coordinate increases across the feeding channel towards the upper wall. For the porous-electrode profiles, instead, the vertical coordinate was shifted with respect to the electrode–matrix interface. In this case, the origin corresponds to the reactive surface and the coordinate increases through the porous electrode towards the channel–porous interface. This convention allows each profile to start from $y^* = 0$ within its own region while preserving the physical distinction between the channel and porous domains.

The porous-medium profiles are represented over restricted horizontal intervals in order to resolve the small local variations occurring through the electrode thickness. Consequently, differences that appear pronounced graphically must be interpreted in relation to the low characteristic velocity of the porous domain. The strong hydraulic resistance of the porous electrode substantially limits gas motion and considerably attenuates the

velocity perturbations transmitted from the feeding channel.

Arc-side point

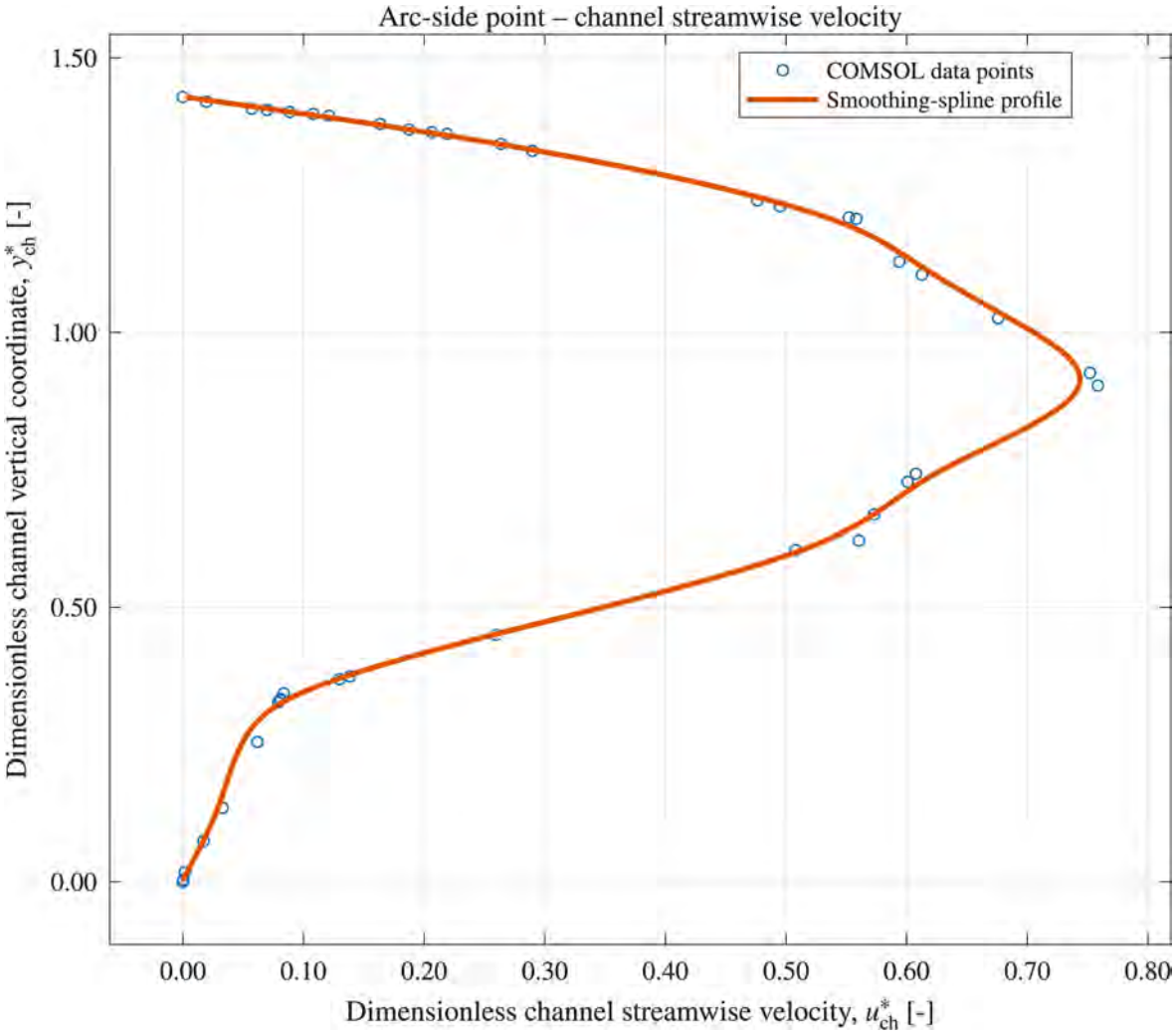

Figure 4.10: Dimensionless anodic streamwise velocity in the feeding channel along the cross-stream profile through the arc-side point (a).

The channel streamwise velocity at the arc-side point is reported in Figure 4.10. Starting from the channel–porous interface, the local coordinate increases towards the upper solid wall. The profile shows low values of u^*_{ch} close to the channel–porous interface and close to the upper wall, while the maximum streamwise velocity develops within the internal portion of the feeding channel.

Moving from the channel–porous interface towards the channel interior, the streamwise velocity progressively increases and reaches a maximum value of approximately $u^*_{ch} = 0.75$. Approaching the upper solid wall, the velocity then decreases again, consistently

with the no-slip condition imposed on the wall.

The streamwise component remains positive throughout the channel profile. The arc-side opening is therefore directly connected to the principal axial gas stream and the gas approaches the porous region without undergoing a reversal of the main flow direction in the feeding channel.

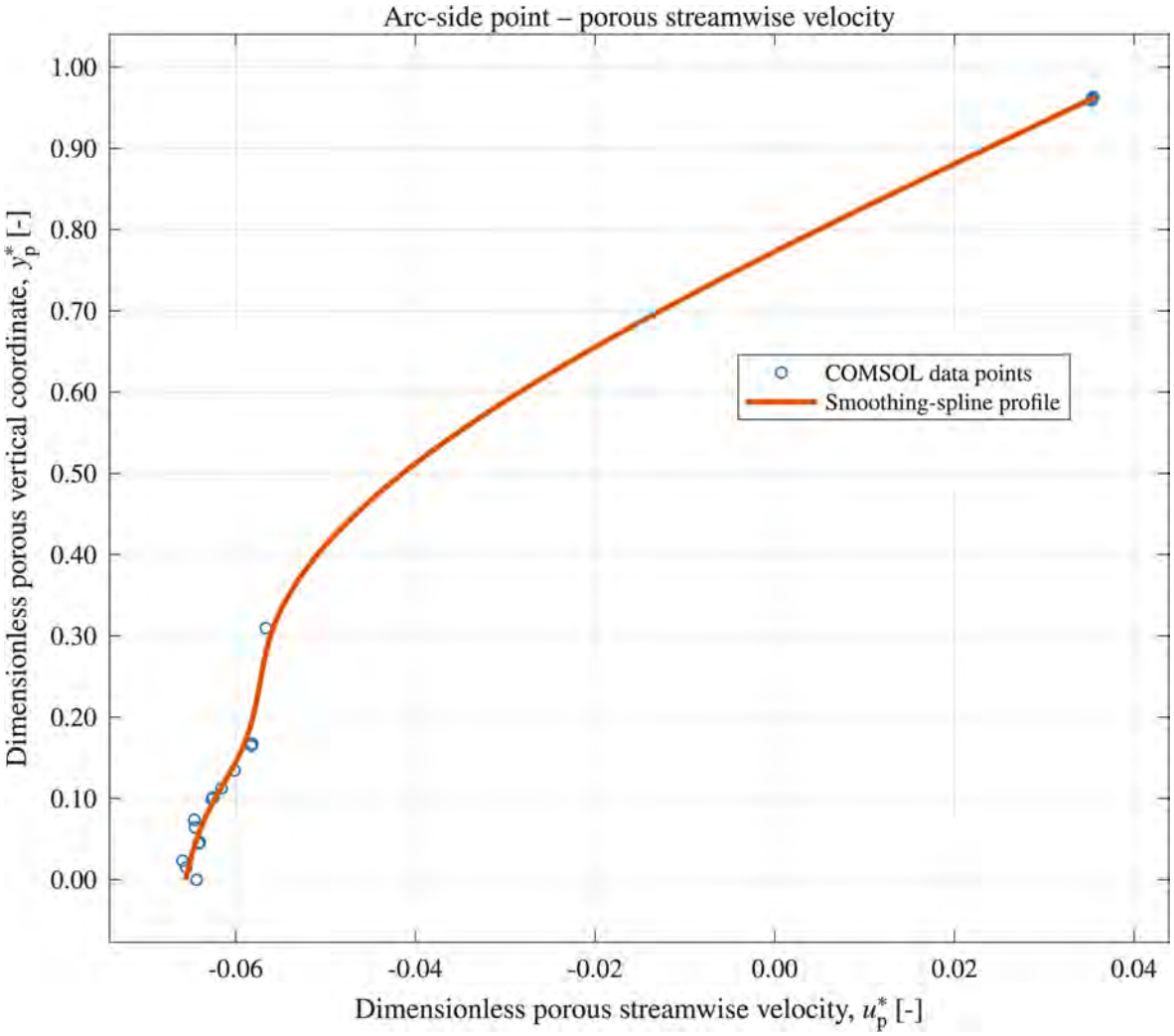

Figure 4.11: Dimensionless anodic streamwise velocity inside the porous electrode along the cross-stream profile through the arc-side point (a).

The corresponding streamwise velocity inside the porous electrode is shown in Figure 4.11. In this case, the local coordinate starts from the electrode–matrix interface, corresponding to the reactive surface, and increases towards the channel–porous interface. The restricted horizontal scale adopted in the figure makes the local variation of u_p^* clearly visible. However, these variations correspond to small physical velocities because of the strong hydraulic resistance of the electrode.

Close to the reactive surface, the streamwise component is slightly negative. Moving towards the channel–porous interface, u_p^* progressively increases and becomes positive in the upper part of the porous electrode, reaching its largest value close to the channel-facing side.

The negative values observed near the reactive surface are associated with the internal redistribution of gas within the porous layer. At the arc-side point, gas enters the porous electrode through a comparatively favourable opening and is then partially redistributed towards neighbouring regions that are less directly accessible from the feeding channel. This redistribution can locally establish a streamwise pressure gradient opposite to the main channel-flow direction, producing the small negative values of u_p^* observed through part of the electrode thickness.

Therefore, the sign change of u_p^* should not be interpreted as a numerical artefact. It reflects the local reversal of the streamwise component associated with the recirculation-like redistribution of gas inside the porous layer. The phenomenon remains confined to small physical velocities because the porous electrode offers a strong resistance to flow, but it is relevant because it shows that the traditional collector does not feed the porous electrode uniformly.

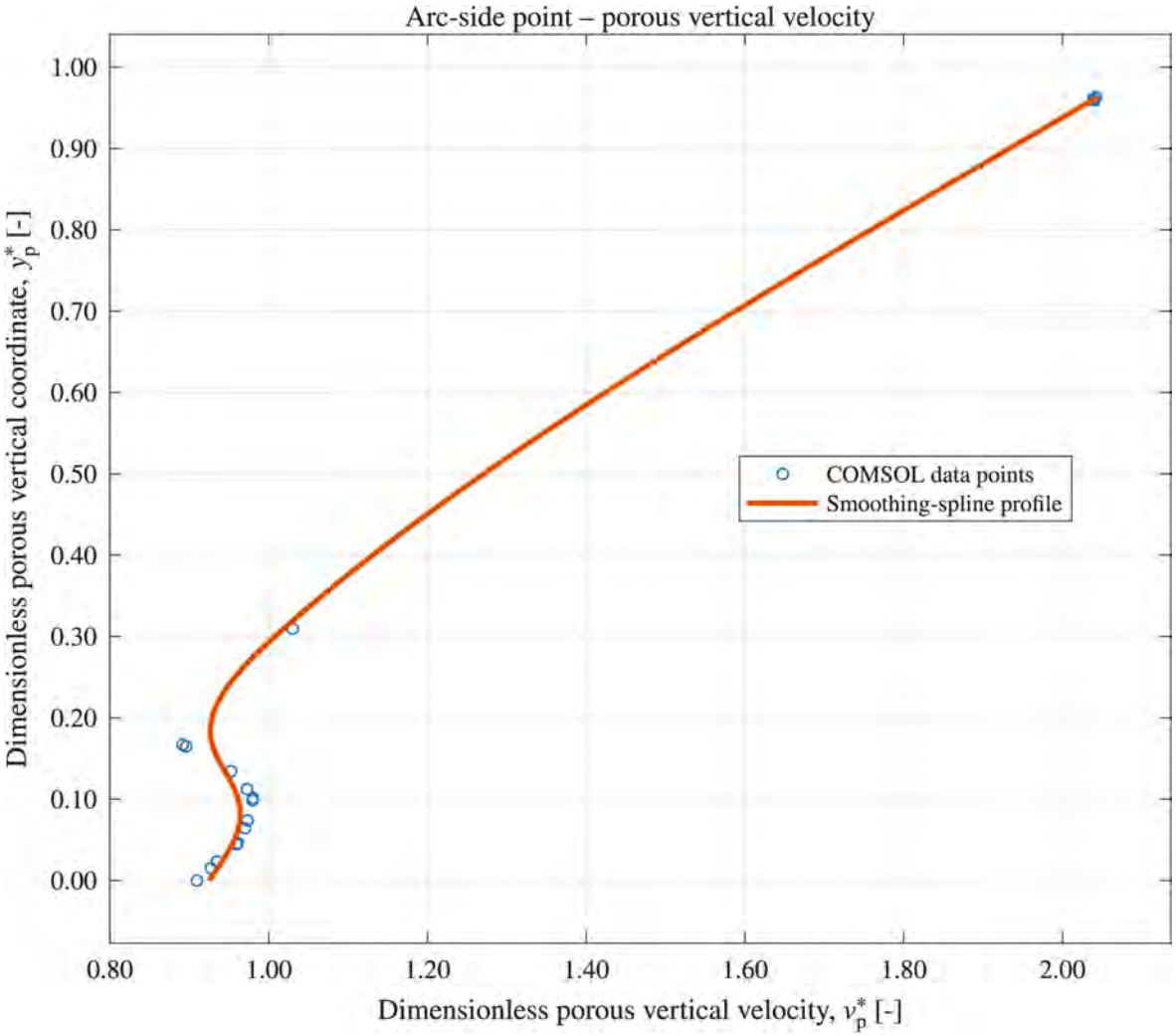

Figure 4.12: Dimensionless anodic cross-stream velocity inside the porous electrode along the profile through the arc-side point (a).

The cross-stream velocity component inside the porous electrode is reported in Figure 4.12. As for the porous streamwise profile, the local coordinate starts from the electrode–matrix interface and increases towards the channel–porous interface. The value of v_p^* is lowest close to the reactive surface and progressively increases towards the channel–porous interface.

More specifically, the dimensionless cross-stream velocity increases from values close to 0.9 near the reactive surface to approximately 2.0 close to the channel-facing side of the porous electrode. This trend indicates that the through-plane convective motion is stronger near the channel–porous interface and is progressively attenuated as the gas penetrates towards the reactive surface.

This attenuation is consistent with the hydraulic resistance of the porous electrode. The

gas entering the porous layer does not preserve the same through-plane velocity through the complete thickness, but is progressively redistributed within the pore network.

The simultaneous reduction of v_p^* towards the reactive surface and the local modification of u_p^* indicate a redistribution of the velocity vector within the porous domain. As the through-plane component is attenuated, a tangential redistribution develops and can locally direct gas towards regions that are less directly accessible from the feeding channel.

The arc-side profile therefore represents a gas-access region in which the feeding channel provides a direct supply to the porous electrode. The porous structure subsequently attenuates the through-plane motion and redistributes part of the gas in the streamwise direction.

Behind-arc point

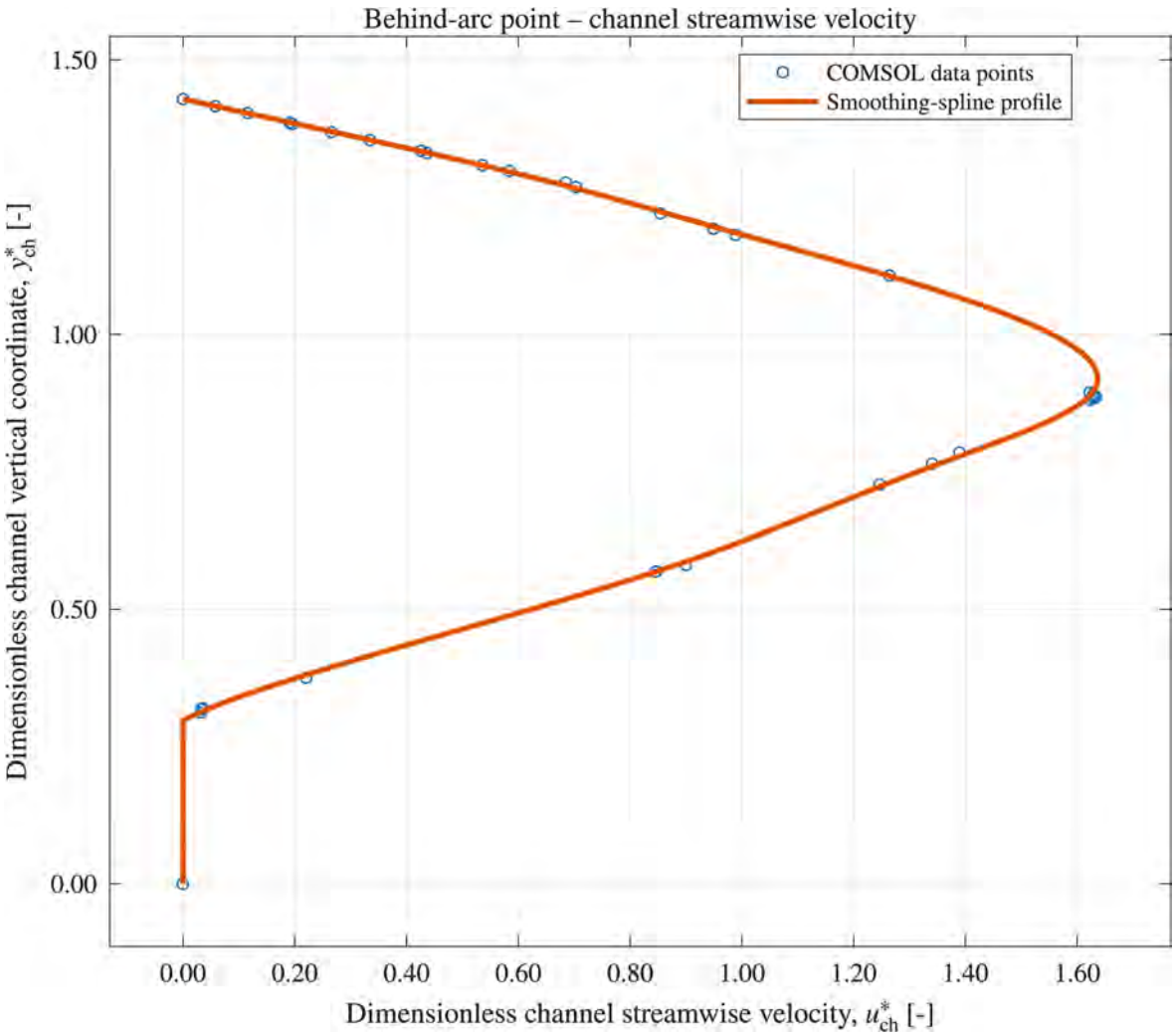

Figure 4.13: Dimensionless anodic streamwise velocity in the feeding channel along the cross-stream profile through the behind-arc point (*b*).

The channel streamwise velocity at the behind-arc point is reported in Figure 4.13. As at the arc-side location, the local coordinate is referred to the channel–porous interface and increases towards the upper channel wall. The velocity remains low close to the channel–porous interface and close to the solid-wall end of the channel.

Moving from the channel–porous interface towards the channel interior, u^*_{ch} progressively increases. A local maximum of approximately 1.7 develops in the intermediate-to-upper portion of the channel profile before the velocity decreases towards the upper wall, consistently with the no-slip condition.

The local maximum reflects the redistribution of the gas downstream of the arched

element. The collector modifies the available flow path and locally concentrates the streamwise motion within the free channel. Nevertheless, the velocity remains positive over the complete channel profile, indicating that the principal axial flow direction is preserved at this extraction point.

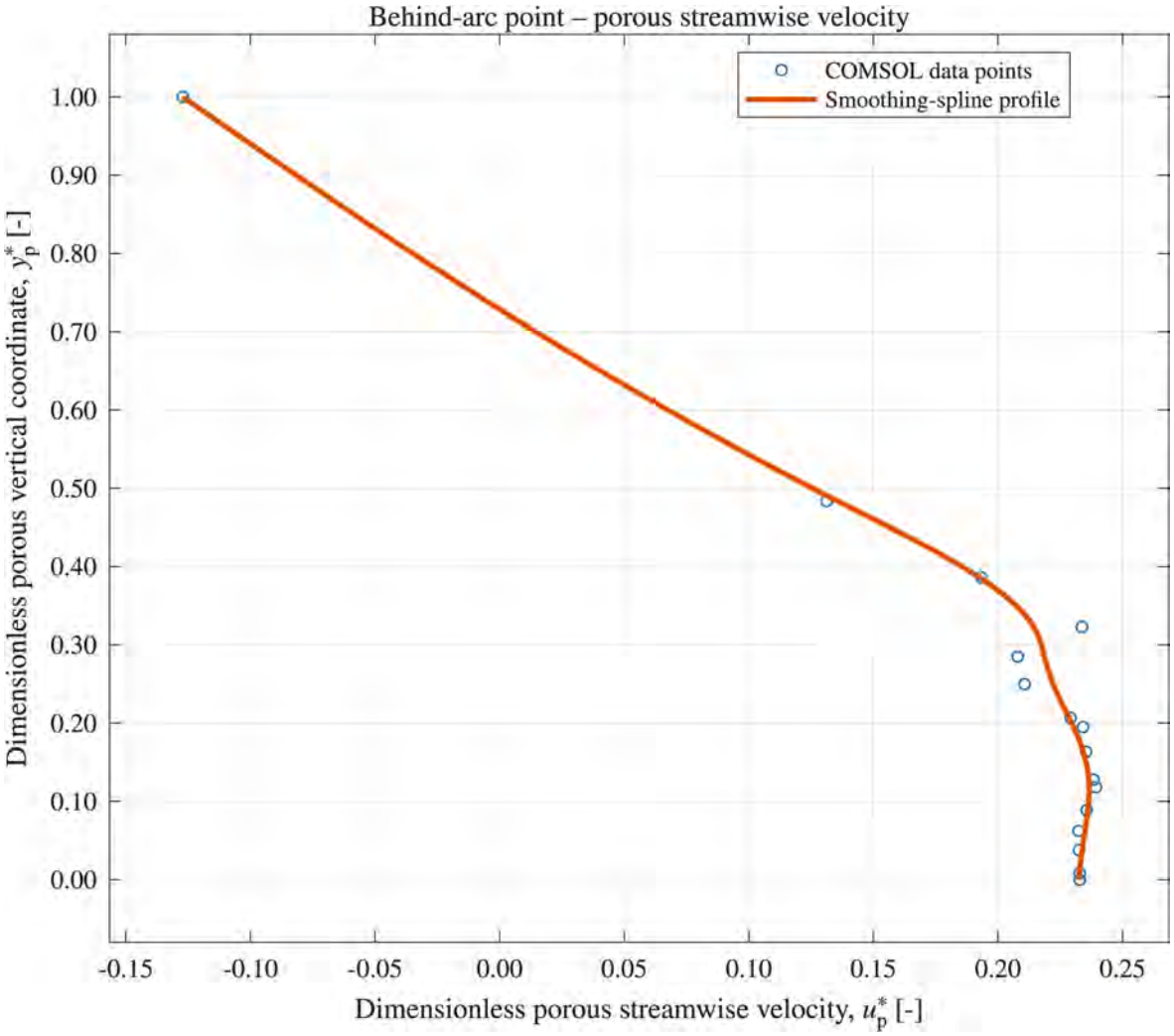

Figure 4.14: Dimensionless anodic streamwise velocity inside the porous electrode along the cross-stream profile through the behind-arc point (b).

Inside the porous electrode, the streamwise velocity exhibits a markedly different distribution, as shown in Figure 4.14. The local coordinate is referred to the electrode–matrix interface, so that the reactive surface corresponds to $y^* = 0$ and the coordinate increases towards the channel–porous interface. The restricted horizontal scale magnifies the local variation, while the corresponding physical streamwise motion remains limited by the resistance of the porous structure.

Positive values of u_p^* are observed over the lower portion of the porous layer, close

to the reactive surface. Moving towards the channel–porous interface, the streamwise component progressively decreases and becomes negative in the upper part of the electrode.

The occurrence of negative u_p^* near the channel-facing side is consistent with the shielding effect generated by the traditional collector. The behind-arc region receives a weaker direct gas supply from the feeding channel because the solid portions of the arched collector partially obstruct the flow above the porous electrode. Gas must therefore be supplied not only from the local opening, but also through tangential redistribution inside the porous medium from neighbouring, more accessible regions.

This redistribution generates local recirculation-like structures inside the porous electrode. In these regions, the streamwise component can locally become opposite to the principal channel-flow direction, even though the magnitude of the physical velocity remains small. The negative values of u_p^* therefore represent the local reverse branch of an internal redistribution cell rather than a large-scale recirculation comparable to that occurring in an open channel.

The result highlights the effect of the traditional collector topology. Since the gas can pass from the channel to the electrode only through discrete holes and through the passages located below or beside the arches, the porous electrode is not supplied uniformly from above. Instead, the gas entering through accessible openings is forced to redistribute within the electrode thickness, giving rise to local streamwise reversals and internal recirculation cells.

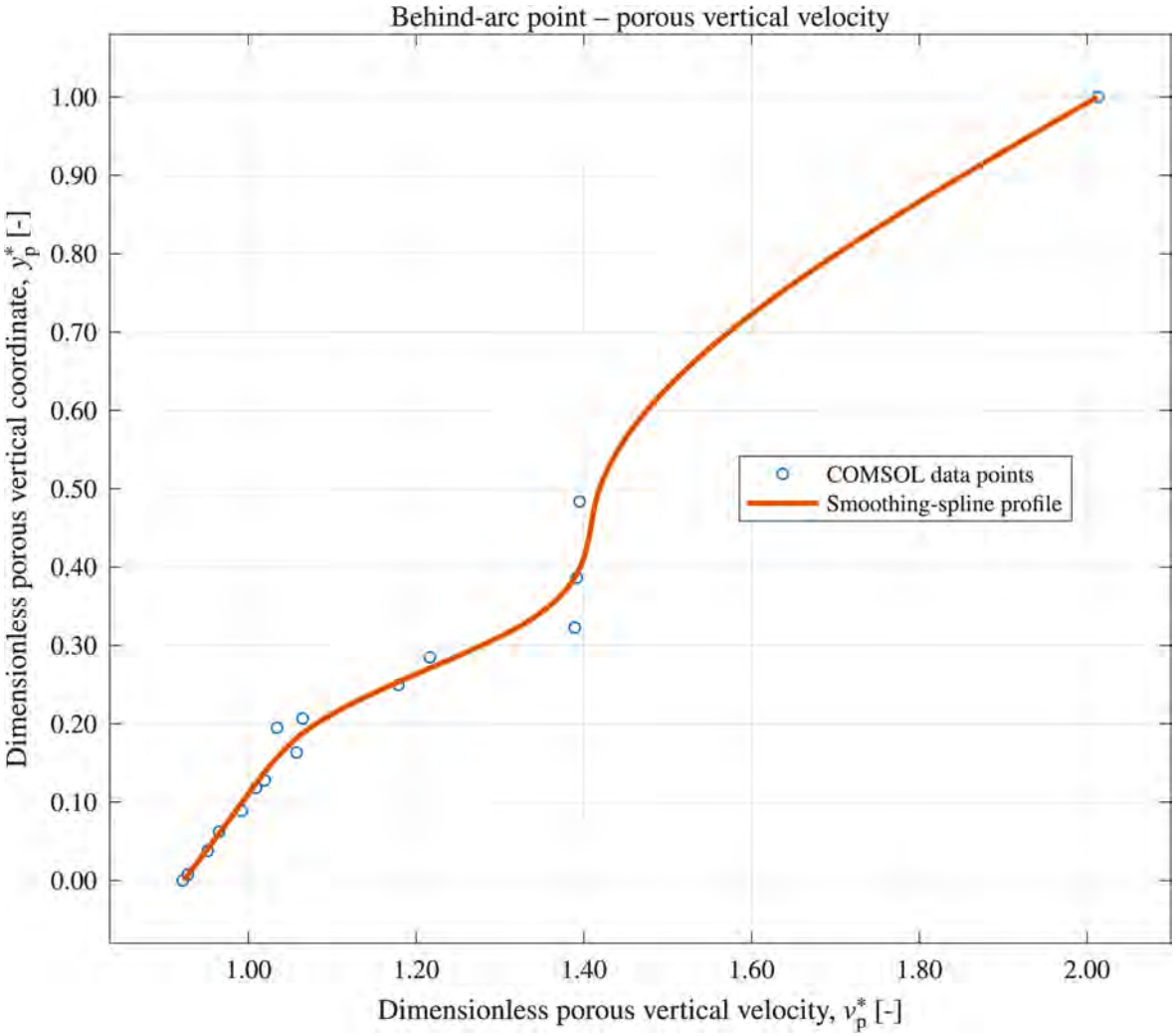

Figure 4.15: Dimensionless anodic cross-stream velocity inside the porous electrode along the profile through the behind-arc point (b).

The cross-stream porous velocity at the behind-arc point is reported in Figure 4.15. As for the previous porous profiles, the local coordinate starts from the electrode–matrix interface and increases towards the channel–porous interface. The profile exhibits a progressive increase from values close to 0.9 near the reactive surface to approximately 2.0 close to the channel-facing side of the electrode.

The general trend is therefore similar to that observed at the arc-side point and confirms that the through-plane convective motion is larger near the channel–porous interface and progressively attenuated towards the reactive surface.

The maximum cross-stream velocity at the behind-arc point is comparable to that observed at the arc-side location. However, the shape of the profile is different. The behind-arc profile exhibits a more gradual variation through the electrode thickness,

indicating a different redistribution of the through-plane motion inside the porous layer.

This behaviour is consistent with the weaker and less direct hydraulic access produced by the shielding of the arched element. Even if the maximum value of v_p^* remains comparable, the gas supply behind the arch is more strongly affected by tangential redistribution inside the porous electrode.

The comparison between the two extraction points therefore identifies two complementary gas-transport mechanisms. At the arc-side opening, the feeding channel provides a comparatively direct through-plane supply to the porous electrode. Behind the arch, the direct through-plane supply is less direct and part of the gas is supplied through tangential redistribution inside the porous electrode.

The local negative values of u_p^* provide additional evidence of this redistribution mechanism. They are consistent with the reverse branch of internal recirculation cells generated by the non-uniform gas access imposed by the traditional collector. Although these variations appear pronounced because of the restricted velocity scales adopted for the porous profiles, the corresponding physical velocities remain small as a consequence of the strong hydraulic resistance of the electrode.

To verify whether these local sign changes were isolated profile features or part of a broader spatial organisation, the two-dimensional streamwise velocity field inside the porous electrode was also inspected.

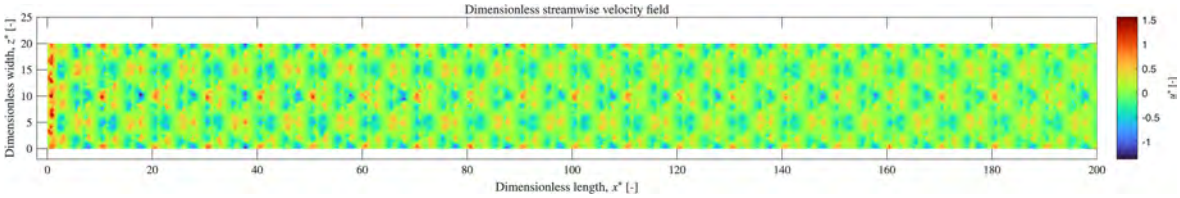

Figure 4.16: Two-dimensional distribution of the dimensionless streamwise velocity component u_p^* inside the porous electrode for the traditional current collector.

The alternating positive and negative regions shown in Figure 4.16 confirm that the sign changes observed in the one-dimensional profiles are part of a periodic redistribution pattern within the porous electrode. These internal recirculation cells arise because the gas cannot enter uniformly from the whole channel-facing surface, but only through the holes and the passages located below or beside the arches. As a result, part of the gas penetrates through the accessible regions and is then redistributed laterally and

streamwise within the porous structure towards the shielded regions.

Overall, the cross-stream profile analysis confirms that the traditional current collector produces a non-uniform transition between the feeding channel and the porous electrode. The solid arches and the limited openings constrain the gas supply to discrete access regions. As a consequence, the porous electrode acts not only as a through-plane transport layer, but also as a redistribution domain in which gas is transferred from directly supplied regions towards shielded areas, producing local internal recirculation cells within the porous medium.

4.2.4 Current Density Distribution on the Reactive Surface

The effect of the non-uniform gas distribution generated by the traditional current collector can finally be observed in the current-density distribution on the reactive surface, corresponding to the electrode–matrix interface.

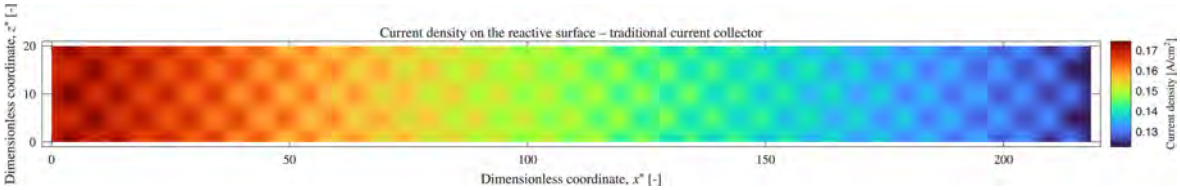

Figure 4.17: Current density distribution on the reactive surface for the traditional current collector.

The current-density distribution reported in Figure 4.17 shows a clear global decrease along the axial direction. The highest values are located near the inlet region, where reactant availability and pressure conditions are more favourable. Moving towards the outlet, the current density progressively decreases as reactant concentrations and local electrochemical conditions evolve along the cell.

Superimposed on the global axial trend, a repeated local modulation is visible over the reactive surface. The distribution contains alternating higher- and lower-current-density regions that reflect the geometrical structure of the traditional collector.

The local variations are consistent with the velocity analysis presented above. Openings that provide more effective communication between the feeding channel and the porous electrode favour reactant renewal, whereas regions affected by geometrical shielding are

less effectively supplied.

The current-density field therefore represents the electrochemical consequence of the non-uniform fluid-dynamic structure generated by the traditional collector. The planar velocity profiles showed extended low-velocity and reverse-flow regions, while the local profiles along y demonstrated that the porous electrode contributes to redistributing the gas between directly accessible and shielded regions. These differences in local gas accessibility are transmitted through the porous electrodes and remain visible as spatial variations in current density.

Overall, the traditional current collector provides gas access to the porous electrodes, but its arched geometry generates a pronounced shielding effect. Gas is preferentially supplied through discrete openings, while the porous electrode partially redistributes the flow towards less directly accessible regions. This non-uniform fluid-dynamic behaviour provides the reference basis for the subsequent analysis of the proposed grooved current collector.

4.3 Grooved Current Collector

After the traditional reference configuration, the grooved current collector is analysed in detail. The discussion follows the physical path of the gas from the feeding channel to the porous electrode and finally to the reactive surface. This organisation allows the influence of the collector geometry to be interpreted progressively: first in terms of pressure and reactant distribution in the feeding channel, then through the local flow redistribution around the embossments, subsequently through gas transport within the porous electrode and, finally, in terms of the local electrochemical response.

The spatial directions and corresponding dimensionless coordinates follow the convention introduced in the simulation parameters and non-dimensional formulation sections. The discussion is organised according to the main physical quantities analysed, namely pressure, reactant concentration, velocity and current density.

In the feeding channel, the gas motion is mainly streamwise and follows the axial direction. Therefore, pressure and concentration profiles are first analysed along x^* in order to describe the global behaviour of the gas stream along the cell. Then,

local velocity profiles around representative embossments are considered to clarify how the grooved geometry redistributes the gas and produces local shielding effects. The analysis then moves to the channel–porous interface and to the porous electrode, where the relevant transport direction becomes mainly vertical. Finally, the reactive surface is analysed, where pressure, concentration and current density represent the final outcome of the coupled fluid-dynamic, transport and electrochemical phenomena.

4.3.1 Pressure Distribution at the Channel–Porous Electrode Interface

The pressure field at the channel–porous electrode interface was analysed by combining a one-dimensional section-averaged representation with a two-dimensional local fluctuation field. The two representations provide complementary information. The section-averaged profile describes the global hydraulic evolution along the main flow direction, whereas the fluctuation field isolates the local pressure redistribution induced by the periodic embossment pattern.

For each axial position, the dimensionless pressure was evaluated at the channel–porous electrode interface, namely at a fixed cross-stream coordinate $y = y_0$, and then averaged along the spanwise z direction. The resulting quantity, $\overline{p}^*(x)$, therefore represents the mean pressure transmitted from the feeding channel to the porous electrode at the corresponding dimensionless axial coordinate.

To remove the dominant axial pressure decrease and identify the local geometrical perturbation, the dimensionless pressure fluctuation was defined as

$$p'^*(x, z) = p^*(x, z) - \overline{p}^*(x), \tag{4.2}$$

where $\overline{p}^*(x)$ is the section-averaged pressure at the same axial position. Positive values of p'^* therefore identify regions where the local pressure is higher than the corresponding transverse mean, whereas negative values indicate locally lower-pressure regions.

Anodic channel–porous electrode interface

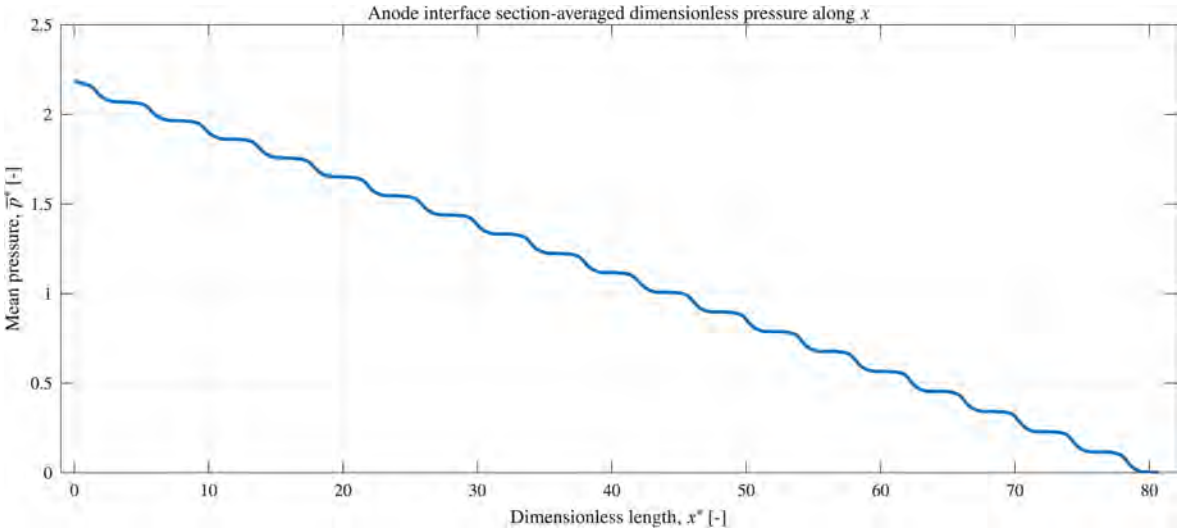

Figure 4.18: Section-averaged dimensionless pressure along the anodic channel–porous interface for the grooved current collector.

The anodic section-averaged pressure reported in Figure 4.18 progressively decreases from the inlet to the outlet. The dominant behaviour is therefore the expected axial pressure loss associated with viscous dissipation along the gas path.

However, the pressure decrease is not perfectly linear. A regular step-like modulation is superimposed on the global trend. The repeated spatial frequency of these variations corresponds to the periodic arrangement of the embossments.

Each embossment locally modifies the gas passage in the free-flow domain. The incoming stream is redistributed around the raised feature and through the surrounding open regions. Consequently, the pressure transmitted to the porous layer alternates between portions characterised by a more rapid local pressure decrease and portions in which the profile becomes comparatively flatter.

The section-averaged curve therefore provides evidence of a periodic hydraulic forcing imposed on the porous electrode. Nevertheless, because the pressure is averaged in the transverse direction, the local stoss–lee redistribution around the individual embossments is partially hidden. This local structure becomes visible in the pressure fluctuation field.

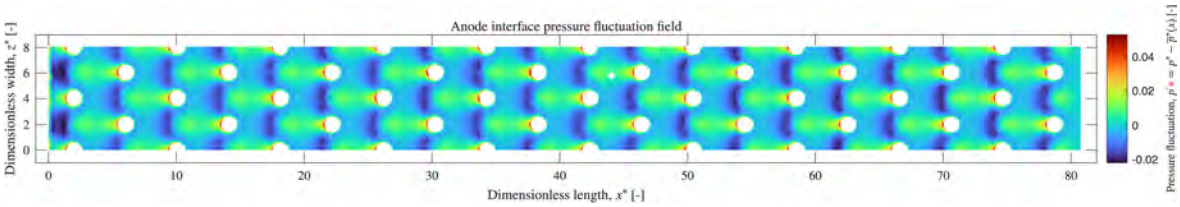

Figure 4.19: Local dimensionless pressure fluctuation field at the anodic channel–porous electrode interface.

The two-dimensional fluctuation field shown in Figure 4.19 reveals a highly organised pressure distribution around the embossments. Because the mean pressure $\overline{p}^*(x)$ has been removed at every axial location, the global inlet-to-outlet pressure decrease is no longer dominant and the local geometrical effect can be analysed directly.

Alternating positive and negative pressure deviations develop around each raised feature. Regions of positive p'^* are mainly associated with portions of the interface exposed to the incoming flow and with the open passages through which the gas is redirected around the embossments. In these regions, the interaction between the incoming stream and the collector produces a local pressure level above the transverse mean.

On the downstream side of the embossments, regions of negative pressure fluctuation become visible. These lower-pressure zones are spatially aligned with the hydraulically screened portions of the flow field. The local pressure is therefore below the corresponding section-averaged value.

The staggered embossment arrangement is clearly reproduced in the pressure field. Each row generates a similar local sequence of positive and negative pressure fluctuations, and this structure is repeated over the active length. The local pressure disturbance is therefore not limited to isolated regions of the collector, but represents a periodic forcing applied to the porous anode.

At the anodic operating conditions, the fluctuation magnitude remains relatively limited compared with the global axial pressure variation. Nevertheless, the spatial regularity of the field demonstrates that the collector geometry imposes a well-defined local pressure pattern at the entrance of the porous electrode.

Cathodic channel–porous electrode interface

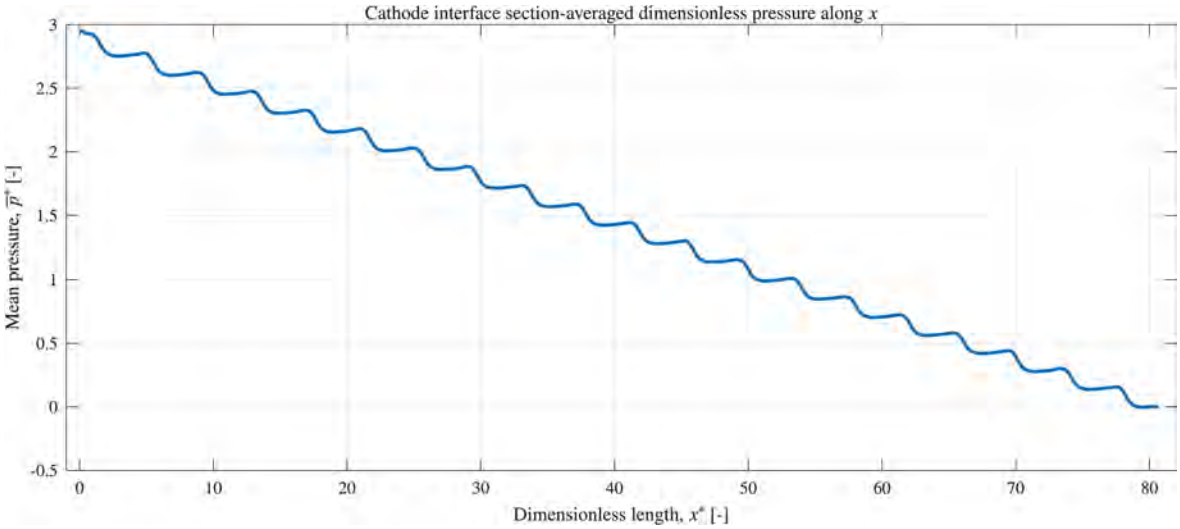

Figure 4.20: Section-averaged dimensionless pressure along the cathodic channel–porous electrode interface for the grooved current collector.

The cathodic section-averaged pressure profile is reported in Figure 4.20. As observed on the anodic side, the pressure progressively decreases along the axial direction. The overall pressure loss is accompanied by a pronounced periodic modulation associated with the repeated embossment rows.

The local variations are more evident than in the anodic profile. The curve repeatedly alternates between relatively steep pressure reductions and regions of partial local recovery or reduced pressure slope. The collector geometry therefore produces a stronger hydraulic signature at the cathodic channel–porous electrode interface.

This difference is consistent with the cathodic flow conditions. The larger cathodic reference velocity and higher gas density increase the momentum of the gas stream. The interaction with the same embossment geometry consequently produces a stronger local redistribution of the pressure field.

The comparison between the anodic and cathodic mean profiles shows that the collector introduces the same periodic hydraulic mechanism in both compartments, but with different intensity. The higher cathodic hydraulic forcing amplifies the effect of the local geometrical restrictions and open passages.

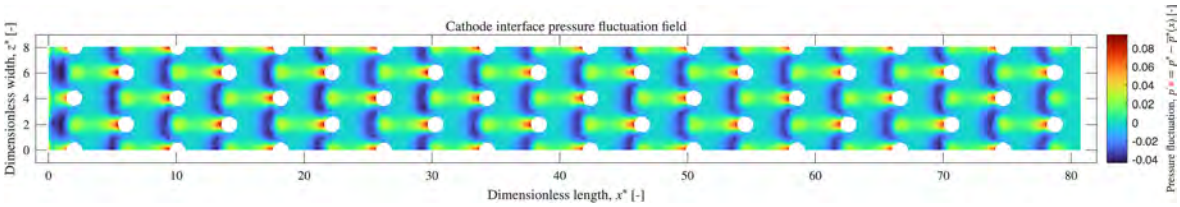

Figure 4.21: Local dimensionless pressure fluctuation field at the cathodic channel–porous electrode interface.

The cathodic fluctuation field in Figure 4.21 shows the same periodic organisation identified on the anodic side, but with larger local deviations from the section-averaged pressure.

Positive-pressure fluctuations develop in the regions exposed to the incoming stream and in the preferential passages between neighbouring embossments. These areas form elongated higher-pressure structures aligned with the local gas redistribution around the raised features.

Immediately downstream of the embossments, pronounced negative fluctuations are observed. The pressure reduction extends over the lee region and identifies the local hydraulic shadow of each raised feature. The higher cathodic flow velocity increases the pressure difference between the directly exposed and screened portions of the interface.

The difference between the anodic and cathodic fluctuation fields is therefore primarily quantitative rather than qualitative. Both sides exhibit the same repeated stoss–lee pressure organisation imposed by the grooved pattern. On the cathodic side, however, the larger momentum of the gas intensifies the contrast between these regions.

These results are particularly relevant for the subsequent porous-medium analysis. The pressure field at the channel–porous electrode interface constitutes the hydraulic boundary condition directly transmitted to the porous electrode. The non-uniform pressure distribution identified in Figure 4.19 and Figure 4.21 can therefore contribute to spatial variations in the vertical convective transport through the porous domains.

4.3.2 Reactant Distribution at the Channel–Porous Electrode Interface

The distribution of the main reacting species was analysed using the same combination of a one-dimensional section-averaged profile and a two-dimensional interface field. Hydrogen was considered on the anodic side, while carbon dioxide was analysed on the cathodic side, since these species represent the limiting reactants adopted for the non-dimensionalisation of the two compartments.

The one-dimensional profiles describe the global evolution of the mean reactant availability along the active length. The two-dimensional maps are then used to determine whether the local flow redistribution around the embossments produces spatial concentration non-uniformities that are not visible in the section-averaged quantities.

Unlike the pressure maps discussed previously, the following two-dimensional concentration fields represent the local dimensionless concentration itself. They therefore contain both the global axial depletion of the reacting species and the local concentration perturbations induced by the collector geometry.

The reactant utilisation factors were evaluated from the inlet and outlet molar flow rates obtained from the numerical solution. Under the analysed operating conditions, the hydrogen utilisation was approximately $U_{\mathrm{H_2}} = 0.20$, whereas the carbon dioxide utilisation was approximately $U_{\mathrm{CO_2}} = 0.31$.

These values indicate moderate global reactant consumption over the modelled active length. This condition is particularly suitable for the purpose of the present analysis, because severe downstream reactant starvation does not dominate the electrochemical response. As a result, the local variations in reactant concentration and current density remain mainly associated with the gas-distribution effects introduced by the current-collector geometry, rather than being masked by an excessive global depletion of the reactants. Consequently, the influence of the collector design can be distinguished over the complete reactive surface.

The difference between the two utilisation factors must be interpreted considering the different inlet molar supplies and the different transport and chemical conditions established in the two compartments. Since utilisation is defined relative to the inlet

molar flow rate of the individual species, identical utilisation values are not required even though the anodic and cathodic electrochemical processes are coupled through the cell current.

Moreover, the anodic compartment includes the Water Gas Shift equilibrium, which can locally redistribute the gas composition and modify the availability of H_2. No equivalent gas-phase equilibrium reaction is present on the cathodic side. In addition, the subsequent porous-electrode analysis will show that the vertical convective transport of CO_2 is directed towards the reactive surface and acts in the same overall direction as the diffusive contribution. These mechanisms may contribute to the different utilisation levels obtained for the two reactants and will be further discussed in the following sections.

Hydrogen distribution at the anodic channel–porous electrode interface

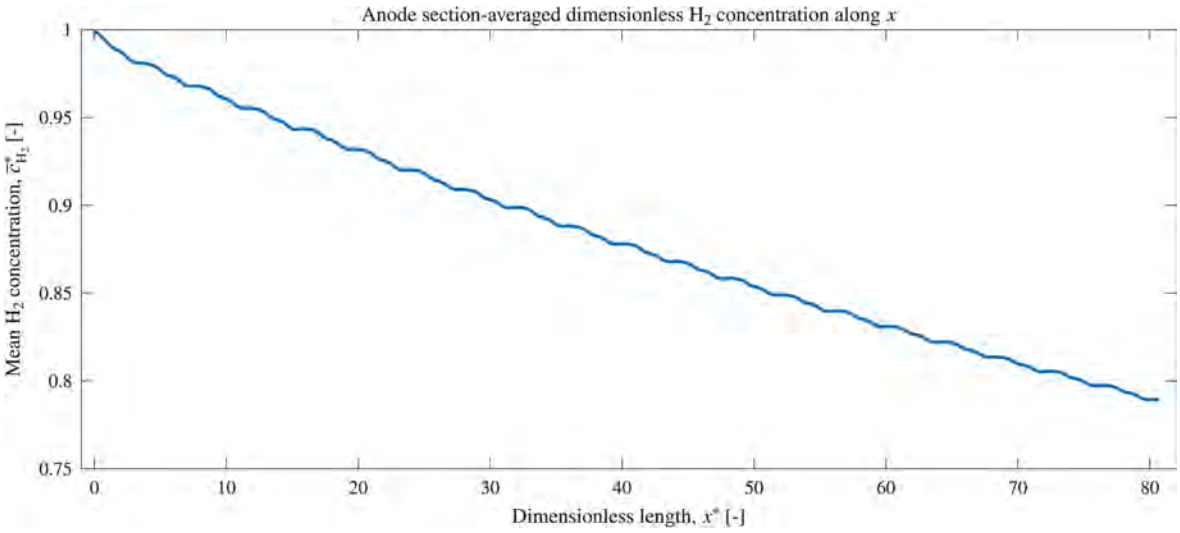

Figure 4.22: Section-averaged dimensionless H_2 concentration along the anodic channel–porous electrode interface for the grooved current collector.

The mean dimensionless hydrogen concentration reported in Figure 4.22 progressively decreases from approximately the inlet reference value to lower concentrations towards the outlet. The decreasing trend reflects the continuous consumption of hydrogen at the anodic reactive surface due to electrochemical oxidation.

The overall axial concentration reduction is consistent with the hydrogen utilisation of approximately 20% obtained from the numerical solution. The moderate utilisa-

tion limits severe hydrogen depletion over the modelled active length and maintains sufficient reactant availability towards the downstream region.

The concentration profile is substantially smoother than the corresponding pressure profile. Small local oscillations remain visible, but their amplitude is limited compared with the total axial concentration decrease. The periodic perturbation generated by the embossments therefore has a comparatively weak effect on the section-averaged hydrogen concentration.

This behaviour indicates that the hydrogen-containing anodic gas mixture is able to redistribute relatively effectively in the feeding region. The lower anodic streamwise velocity reduces the intensity of the preferential flow paths generated by the embossments, while transverse and diffusive transport contribute to smoothing local concentration differences.

In addition to these transport mechanisms, the Water Gas Shift equilibrium implemented in the anodic feeding channel provides an additional mechanism for local compositional redistribution among CO, H_2O, CO_2 and H_2. A local variation in hydrogen concentration can therefore be accompanied by a corresponding adjustment of the WGS equilibrium composition.

The WGS reaction should not be interpreted as a mechanism capable of compensating for the overall electrochemical consumption of hydrogen. Nevertheless, its presence may contribute to smoothing local H_2 concentration deficits and to maintaining a comparatively regular anodic concentration field.

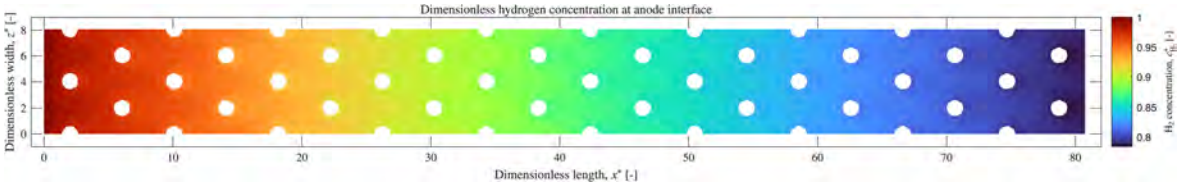

Figure 4.23: Two-dimensional dimensionless H_2 concentration distribution at the anodic channel–porous electrode interface.

The two-dimensional hydrogen field shown in Figure 4.23 provides a spatial interpretation of the smooth mean profile. The dominant feature is the progressive axial reduction in hydrogen concentration. The colour field changes gradually from the inlet towards the outlet, with no extended strongly depleted regions associated with individual em-

bossments.

Local concentration perturbations are nevertheless visible around the projected embossment positions. The concentration field is slightly distorted in the regions directly influenced by the raised features and by the neighbouring open passages. However, these local variations remain weak compared with the overall axial depletion.

Importantly, the regions downstream of the embossments do not develop long and clearly defined low-concentration wakes. The hydraulic shadow observed in the pressure fluctuation field therefore produces only a moderate concentration response on the anodic side.

This result is consistent with the lower anodic streamwise velocity. The local redistribution imposed by the embossments is less strongly concentrated into preferential flow paths and the concentration contrast between the stoss and lee regions is partially attenuated by transverse and diffusive transport.

The WGS equilibrium provides an additional distinction from the cathodic compartment. Since the equilibrium reaction is also implemented in the anodic feeding channel, the local gas composition can adjust according to the coupled CO–H_2O–CO_2–H_2 balance. This compositional adjustment may further contribute to reducing local hydrogen deficits generated by the fluid-dynamic redistribution.

The two-dimensional field consequently confirms that the relatively weak oscillations observed in the section-averaged hydrogen profile are not simply an artefact of transverse averaging. The local hydrogen distribution itself remains comparatively smooth.

Carbon dioxide distribution at the cathodic channel–porous electrode interface

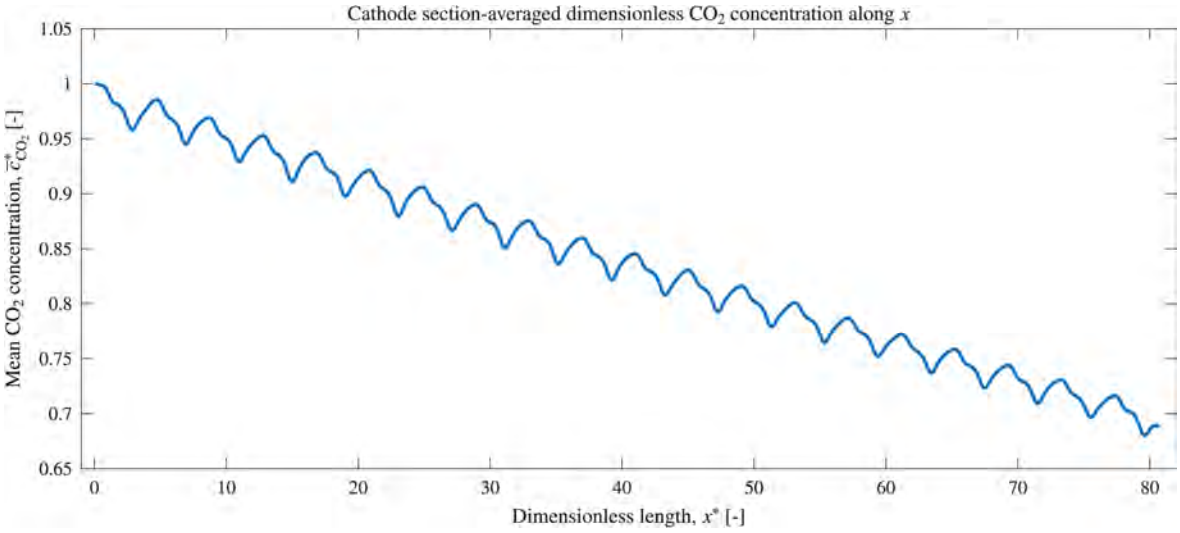

Figure 4.24: Section-averaged dimensionless CO_2 concentration along the cathodic channel–porous electrode interface for the grooved current collector.

The section-averaged dimensionless carbon dioxide concentration is shown in Figure 4.24. The mean CO_2 concentration progressively decreases along the axial direction as carbon dioxide is consumed at the cathodic reactive surface due to electrochemical reduction.

The overall depletion is consistent with the carbon dioxide utilisation of approximately 31% obtained from the numerical solution. The higher utilisation with respect to hydrogen must be interpreted together with the different inlet molar supply and the specific transport conditions established in the cathodic compartment.

In contrast with the anodic hydrogen profile, a pronounced periodic modulation is superimposed on the global concentration decrease. The concentration repeatedly decreases and partially recovers over a spatial interval corresponding to the embossment periodicity.

The presence of these oscillations indicates that the cathodic reactant distribution is considerably more sensitive to the local flow redistribution produced by the grooved geometry. As the cathodic stream interacts with each embossment row, the gas is preferentially redirected through the open passages. The regions downstream of the raised features are less effectively renewed and the local carbon dioxide concentration

decreases.

A partial concentration recovery occurs when the gas reaches a more accessible passage and local convective renewal increases. The repeated oscillation in the mean profile is therefore the species-transport counterpart of the periodic hydraulic redistribution identified in the cathodic pressure field.

Unlike the anodic compartment, the cathodic domain does not include a gas-phase equilibrium reaction analogous to the Water Gas Shift reaction capable of locally redistributing the consumed reactant through the conversion of other species. The local CO_2 concentration is therefore more directly governed by the balance between electrochemical consumption and transport from the feeding stream.

As will be discussed in the subsequent porous-electrode analysis, the vertical convective transport of CO_2 is directed towards the reactive surface and acts in the same overall direction as the diffusive contribution. The two transport mechanisms therefore jointly supply carbon dioxide through the porous cathode and may contribute to sustaining the larger relative CO_2 utilisation observed under the analysed operating conditions.

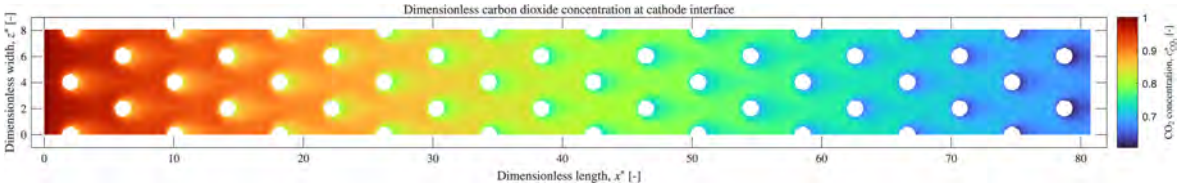

Figure 4.25: Two-dimensional dimensionless CO_2 concentration distribution at the cathodic channel–porous electrode interface.

The two-dimensional carbon dioxide distribution reported in Figure 4.25 clearly reveals the origin of the oscillations observed in the section-averaged profile. In addition to the global axial concentration decrease, well-defined local concentration structures develop around the embossments.

The gas regions associated with the open passages maintain comparatively higher CO_2 concentrations. These areas are more effectively connected to the incoming cathodic stream and are continuously renewed by convective transport.

Conversely, lower-concentration regions develop downstream of the embossments. These depleted structures are spatially aligned with the lee-side regions identified in the pressure fluctuation field. The raised elements partially screen these portions of the inter-

face from the main stream, reducing local convective renewal. The resulting concentration field therefore develops wake-like depleted regions that extend downstream of the embossments.

The effect becomes increasingly visible along the axial direction. As the bulk CO_2 concentration progressively decreases, the ability of the surrounding gas to compensate for the local depletion is reduced. Consequently, the concentration deficit in the screened regions becomes more pronounced towards the outlet.

The comparison with the anodic hydrogen distribution is particularly significant. Both compartments are subjected to the same grooved geometry and show a similar local pressure organisation around the embossments. However, the concentration response is markedly different.

On the anodic side, the lower streamwise velocity, transverse and diffusive redistribution, and the local adjustment of the WGS equilibrium contribute to maintaining a comparatively smooth hydrogen field. On the cathodic side, the larger flow velocity intensifies the separation between preferential flow passages and lee-side screened regions, while no corresponding gas-phase equilibrium mechanism is present to locally redistribute depleted CO_2.

The resulting reduction in local convective renewal therefore produces a clearly modulated carbon dioxide concentration field. At the same time, the through-plane convective and diffusive transport mechanisms supply CO_2 towards the reactive surface. Their common overall transport direction favours reactant transfer through the porous cathode, although the local magnitude of both contributions remains influenced by the hydraulic shielding imposed by the embossment geometry.

Therefore, the stronger cathodic concentration non-uniformity does not result from a lower global gas supply alone. It arises from the combined influence of the local velocity redistribution imposed by the embossment pattern, the absence of an equilibrium redistribution mechanism analogous to the anodic WGS reaction and the different transport balance established in the porous cathode.

These phenomena also provide a possible physical interpretation of the different utilisation values obtained for H_2 and CO_2. The role of vertical convective and diffusive transport in the porous electrodes is analysed in greater detail in the following subsec-

tions.

4.3.3 Velocity Profiles around a Representative Embossment

The local redistribution of the gas around a representative embossment was analysed through circumferential profiles of the dimensionless streamwise velocity. The purpose of this analysis is to isolate the direct fluid-dynamic effect of the raised feature and to quantify the asymmetry generated between the upstream and downstream sides of the embossment.

A representative embossment located in the central region of the computational domain was selected in order to minimise the influence of the inlet and the outlet. As for the traditional current collector, the velocity profiles were extracted on an xz plane located at the mid-height of the feeding channel.

This reference plane was selected to limit the influence of the upper solid wall, where the no-slip condition causes the velocity to decrease towards zero, and of the lower channel region, where the flow field is affected by the coupling with the porous electrode and by the associated resistance to gas motion. The channel mid-plane therefore provides a more representative view of the streamwise flow redistribution induced by the embossment while preserving the same extraction criterion adopted for the traditional configuration.

Four concentric extraction paths were defined around the centre of the selected embossment. The reference radius of the embossment section on the selected channel mid-plane is denoted by r and is equal to

$$r = 1.88 \text{ mm}. \tag{4.3}$$

The four extraction paths, labelled a, b, c and d, were therefore defined at radial distances

$$D = r, \qquad D = 1.5r, \qquad D = 2r, \qquad D = 2.5r, \tag{4.4}$$

respectively. The adopted geometry and the corresponding circumferential paths are

reported in Figure 4.26.

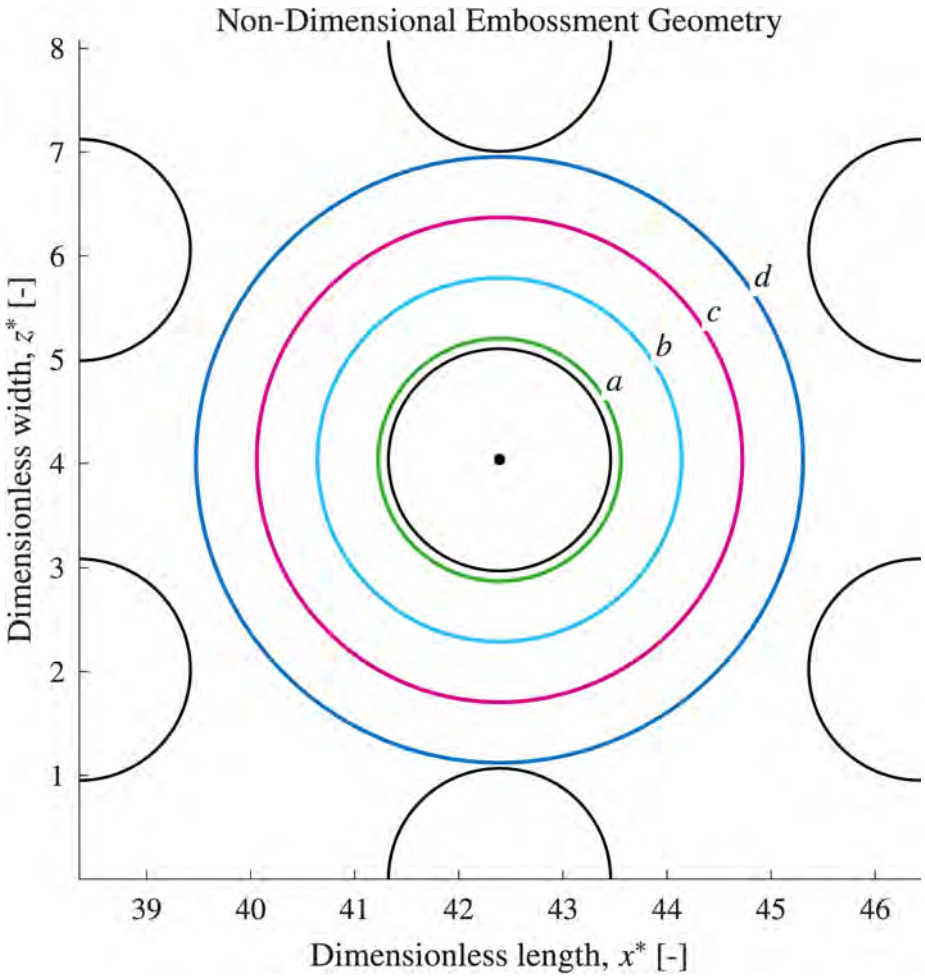

Figure 4.26: Representative embossment section and concentric circumferential paths used for the extraction of the streamwise velocity profiles: path a, $D = r$; path b, $D = 1.5r$; path c, $D = 2r$; and path d, $D = 2.5r$, with $D = 1.88$ mm.

For each circumferential path, the profile was divided according to the position relative to the main flow direction. The upstream portion, directly exposed to the incoming gas stream, is referred to as the *stoss side*. The downstream portion, located behind the embossment with respect to the incoming flow, is referred to as the *lee side*.

The stoss–lee distinction directly identifies the hydraulic asymmetry generated by the embossment. The stoss side corresponds to the region in which the gas approaches the raised feature and is forced to deviate around it. The lee side instead represents the hydraulically screened region downstream of the obstacle, where direct communication with the incoming main stream is reduced.

It should be noted that the analysed quantity is the streamwise velocity component

along the x direction. Therefore, a local reduction in u^* does not necessarily indicate a corresponding reduction in the total velocity magnitude. As the gas approaches the embossment, the flow is forced to bypass the solid feature and part of its momentum can be redistributed towards the transverse z direction. The present profiles quantify the resulting loss of the streamwise component, while the transverse velocity component is not explicitly evaluated in this analysis.

The analysis was performed for both the anodic and cathodic feeding channels in order to determine whether the different flow conditions modify the local response to the same grooved geometry.

Anodic circumferential velocity profiles

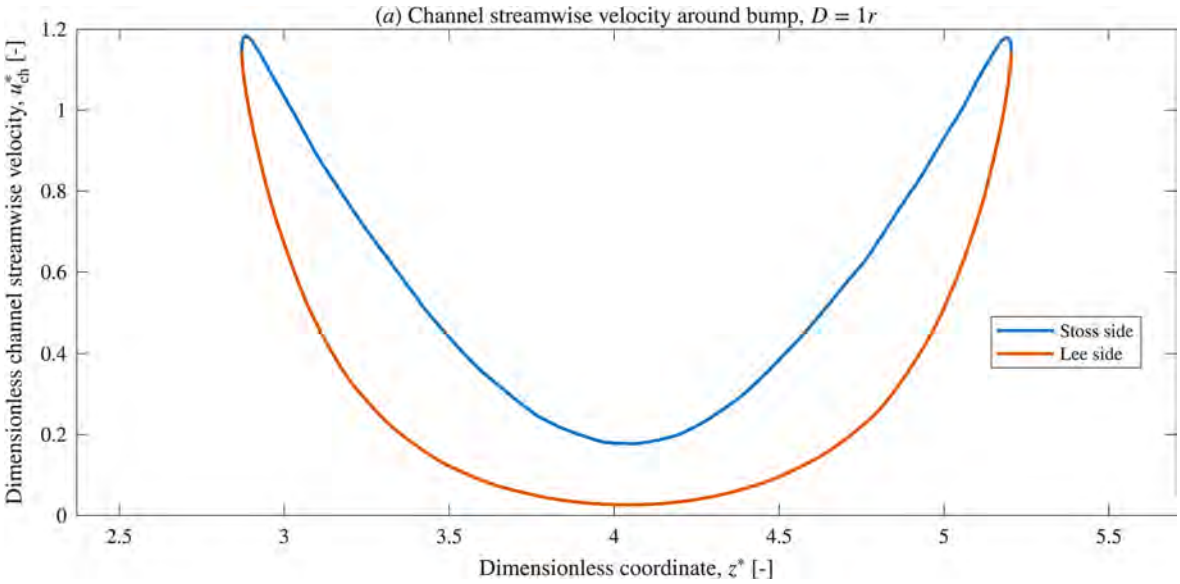

Figure 4.27: Dimensionless anodic streamwise velocity profile around the representative embossment along path a, corresponding to $D = r$.

The velocity profile extracted along path a is reported in Figure 4.27. Since $D = r$, the extraction path is located immediately around the selected embossment and the velocity distribution is primarily controlled by the direct interaction between the gas and the raised feature.

A clear difference is observed between the stoss and lee sides. In the central region of the profile, the stoss-side streamwise velocity remains systematically higher than the corresponding lee-side value. The gas approaching the embossment cannot preserve an

exclusively axial trajectory and is forced to bypass the solid feature.

The reduction of the streamwise component close to the obstacle is therefore consistent with a local redistribution of the velocity vector around the embossment. Part of the incoming gas is diverted through the surrounding free regions, including the transverse direction. Since only u^* is considered here, the corresponding transverse contribution is not quantified directly, but the reduction in the axial component reflects the loss of purely streamwise motion caused by the obstacle.

On the lee side, u^* decreases much more strongly and approaches values close to zero in the central portion of the profile. This pronounced velocity deficit identifies the hydraulic shadow immediately downstream of the embossment. The raised feature screens this region from the main streamwise flow, reducing the local axial momentum and gas renewal.

Moving laterally along the circumferential path, and therefore away from the central region directly influenced by the selected embossment, the streamwise velocity progressively recovers. The flow approaches regions that are less strongly affected by the obstacle and becomes increasingly representative of the surrounding channel motion.

The difference between the stoss and lee curves therefore provides a direct quantitative description of the streamwise shielding generated by the embossment.

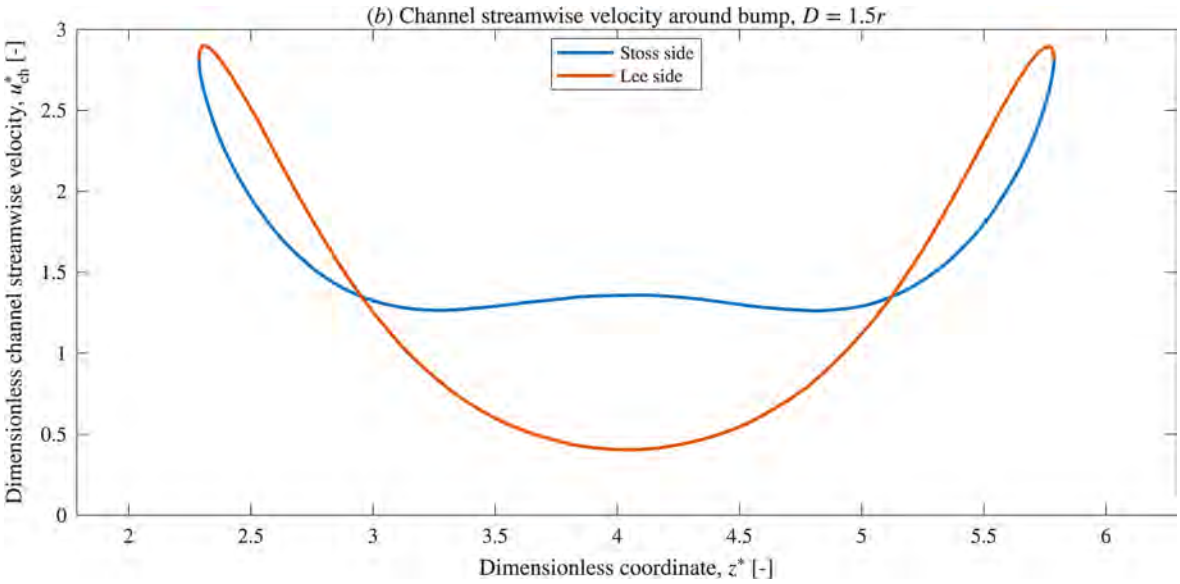

Figure 4.28: Dimensionless anodic streamwise velocity profile around the representative embossment along path b, corresponding to $D = 1.5r$.

The path b, corresponding to $D = 1.5r$, is located farther from the embossment and therefore includes a larger portion of the surrounding flow field. The resulting profile is shown in Figure 4.28.

The stoss–lee asymmetry remains clearly visible. The lee-side velocity presents a broad minimum in the central region, whereas the stoss-side velocity remains considerably higher. The downstream velocity deficit is therefore not confined to the immediate vicinity of the solid feature but persists over a finite region behind the embossment.

Moving towards the lateral portions of the profile, the distance from the selected embossment increases and its direct hydraulic influence progressively decreases. The streamwise velocity consequently tends to recover towards the values characteristic of the less disturbed surrounding flow.

The shape of the stoss-side profile also changes compared with $D = r$. A broader high-velocity region develops because the extraction path increasingly intersects the gas redirected around the selected embossment and transported through the adjacent open regions.

At this radial distance, the velocity field therefore contains both the residual downstream shielding of the selected feature and the progressive recovery of the bypassing flow away from the embossment.

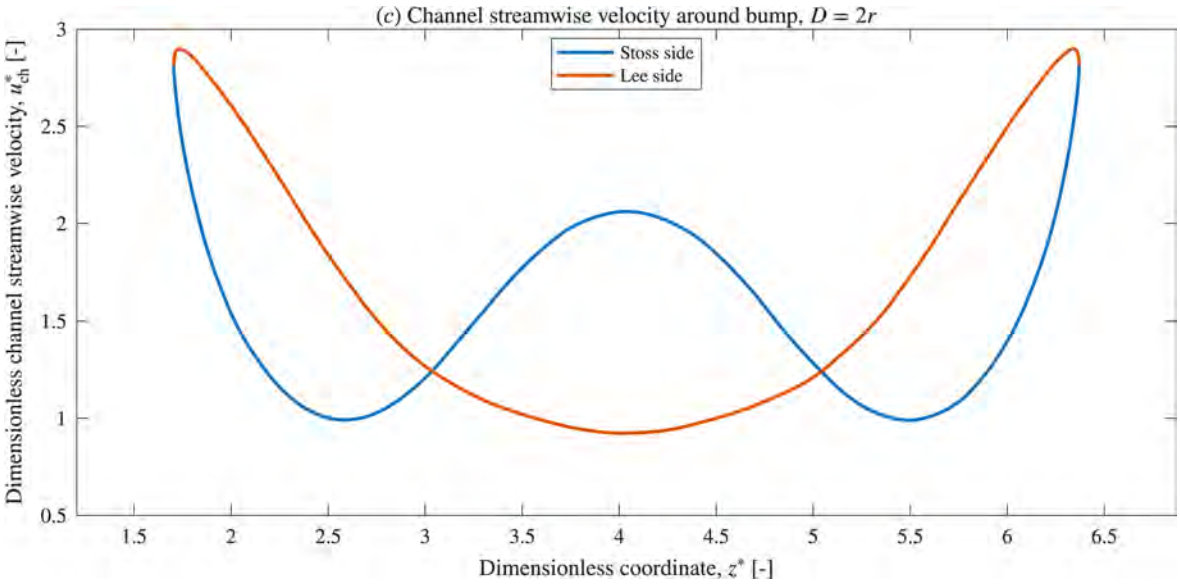

Figure 4.29: Dimensionless anodic streamwise velocity profile around the representative embossment along path c, corresponding to $D = 2r$.

The profile obtained along path c, corresponding to $D = 2r$, is reported in Figure 4.29. The central portion of the profile still preserves the direct stoss–lee asymmetry generated by the selected embossment. The stoss-side streamwise velocity remains higher than the corresponding lee-side value, confirming the persistence of the downstream hydraulic shadow.

However, the circumferential path now extends farther along the transverse z direction. Moving laterally away from the selected embossment, the flow initially approaches less disturbed open regions and the streamwise velocity recovers.

At the outer portions of the profile, the influence of the surrounding staggered collector pattern progressively becomes detectable. The extraction path begins to approach the hydraulic regions affected by neighbouring embossments. Consequently, the velocity distribution is no longer determined exclusively by the selected raised feature.

The local maxima identify comparatively open passages in which the gas can maintain a stronger axial component. Conversely, the lateral reductions in u^* indicate that the approaching neighbouring embossments introduce an additional resistance to the streamwise flow. The gas is again forced to redistribute around the surrounding solid features, reducing its velocity component along x.

The profile therefore describes the transition from the direct influence of the selected embossment to the collective influence of the surrounding grooved pattern.

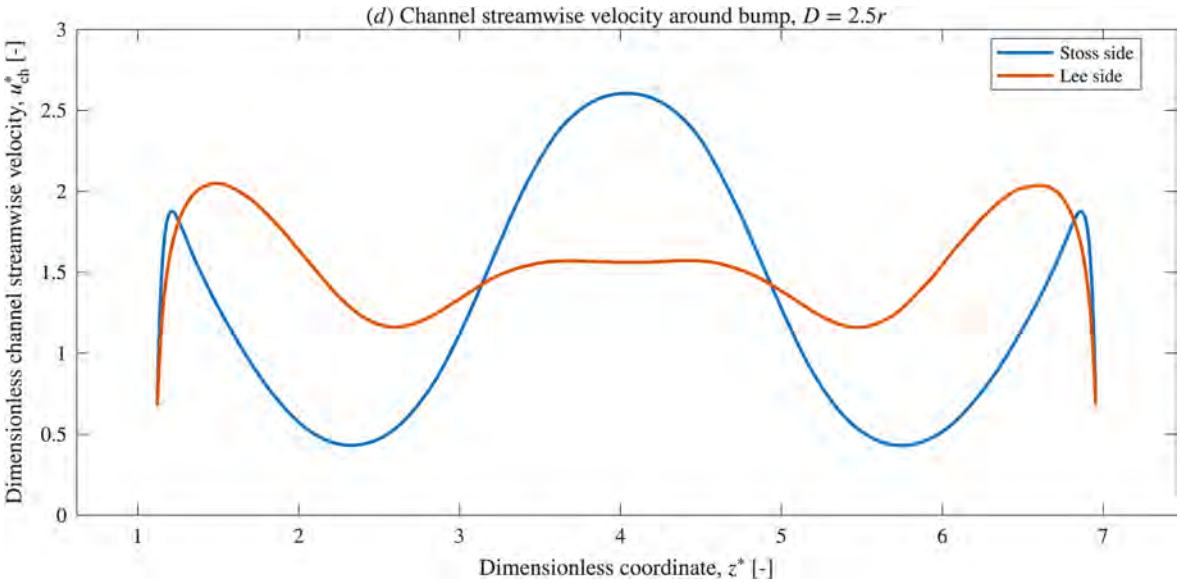

Figure 4.30: Dimensionless anodic streamwise velocity profile around the representative embossment along path d, corresponding to $D = 2.5r$.

For path d, corresponding to $D = 2.5r$, the circumferential extraction line extends well beyond the immediate region surrounding the selected embossment. The profile reported in Figure 4.30 is therefore strongly influenced by the neighbouring raised features of the staggered pattern.

In the central part of the profile, the stoss–lee asymmetry associated with the selected embossment remains visible. The stoss-side velocity is higher than the lee-side value, confirming that the hydraulic shadow of the selected feature can still be identified at this radial distance.

Moving laterally along z, however, the direct influence of the selected embossment becomes progressively less dominant. The circumferential path approaches the neighbouring embossments and the streamwise flow begins to interact with their solid surfaces.

The pronounced lateral minima are therefore associated with the additional hydraulic resistance introduced by the adjacent raised features. As the gas approaches these neighbouring obstacles, the purely streamwise motion is restricted and part of the flow is redirected through the available transverse and inter-embossment passages. The reduction in u^* consequently reflects the collective effect of the surrounding collector pattern rather than the direct shadow of the central embossment alone.

Between these neighbouring influence regions, higher streamwise velocities are recovered in the open passages available to the gas. The alternating maxima and minima observed at $D = 2.5r$ therefore represent the periodic redistribution of the axial flow imposed by the staggered embossment arrangement.

Considering the four anodic profiles together, two spatial mechanisms can be distinguished. In the central region of the circumferential profiles, the direct effect of the selected embossment dominates. The gas reaches the stoss side with a higher streamwise velocity, whereas a pronounced axial velocity deficit develops on the lee side because of hydraulic shielding.

Moving laterally along the z direction, the distance from the selected embossment initially increases and the flow progressively approaches a less disturbed region, producing a recovery of u^*. At the larger extraction radii, particularly for $D = 2.5r$, the circumferential path subsequently enters the regions influenced by the neighbouring

embossments. These adjacent solid features introduce a renewed resistance to streamwise motion and generate the lateral velocity minima observed in the profiles.

The circumferential velocity distribution is therefore governed by the superposition of the direct stoss–lee asymmetry of the selected embossment and the periodic hydraulic influence of the surrounding staggered collector pattern.

Cathodic circumferential velocity profiles

The same circumferential analysis was repeated for the cathodic feeding channel. The geometrical mechanisms identified on the anodic side remain valid: the central part of each profile primarily describes the stoss–lee asymmetry of the selected embossment, whereas the lateral regions progressively move away from the central feature and, at the larger radii, become influenced by the neighbouring embossments.

The purpose of the cathodic comparison is therefore to assess the intensity of the same fluid-dynamic redistribution under the different cathodic flow conditions. Since the velocity is non-dimensionalised using the corresponding cathodic reference quantity, the analysis focuses on the relative response of the flow to the same collector topology.

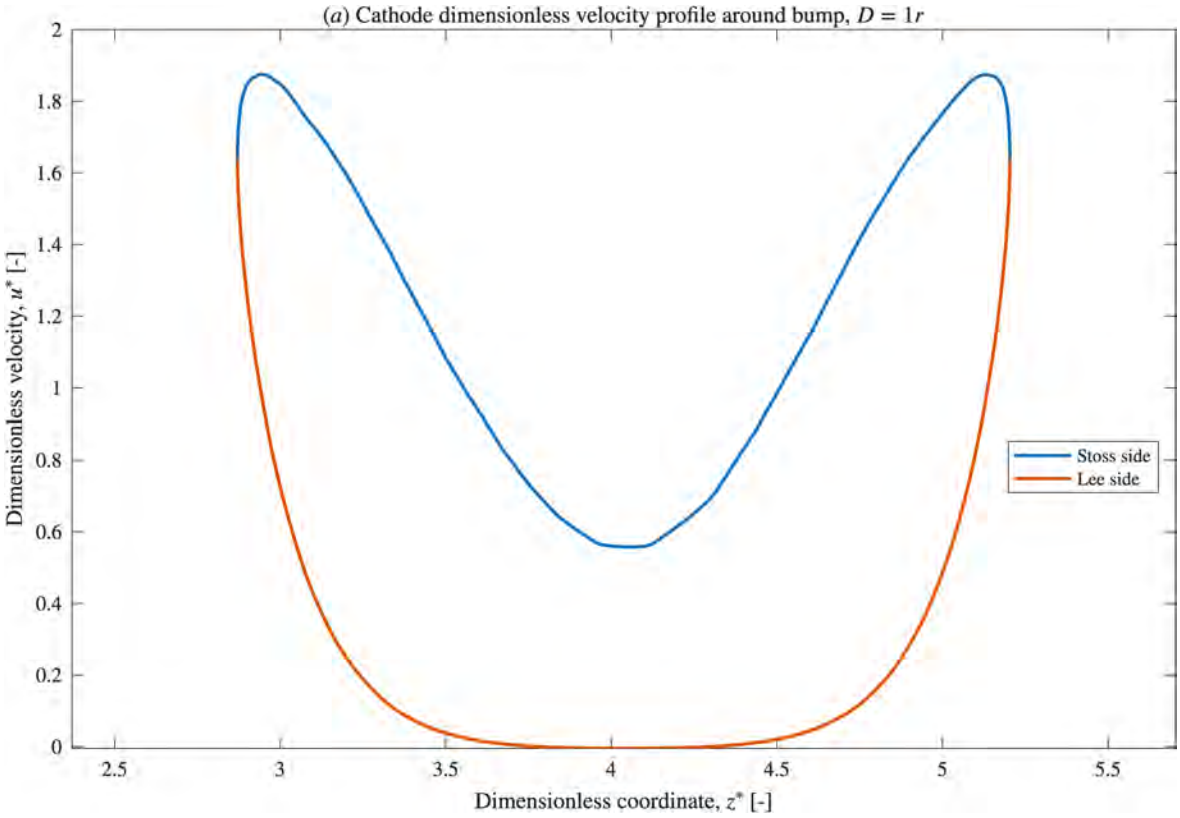

Figure 4.31: Dimensionless cathodic streamwise velocity profile around the representative embossment along path a, corresponding to $D = r$.

The cathodic profile for $D = r$ is shown in Figure 4.31. As on the anodic side, the immediate vicinity of the embossment is characterised by a pronounced stoss–lee asymmetry.

The stoss-side streamwise velocity remains substantially higher in the central region, whereas the lee-side velocity decreases to values approaching zero over an extended portion of the profile. The region immediately downstream of the cathodic embossment is therefore strongly screened from the principal axial flow.

The reduction in u^* close to the raised feature is associated with the same local flow-redirection mechanism discussed for the anode. The gas bypasses the solid obstacle and the streamwise component is reduced as the velocity vector is redistributed around the embossment.

Compared with the anodic profile, the separation between the stoss and lee curves is more pronounced. The cathodic operating conditions therefore amplify the local hydraulic shadow produced by the same collector geometry.

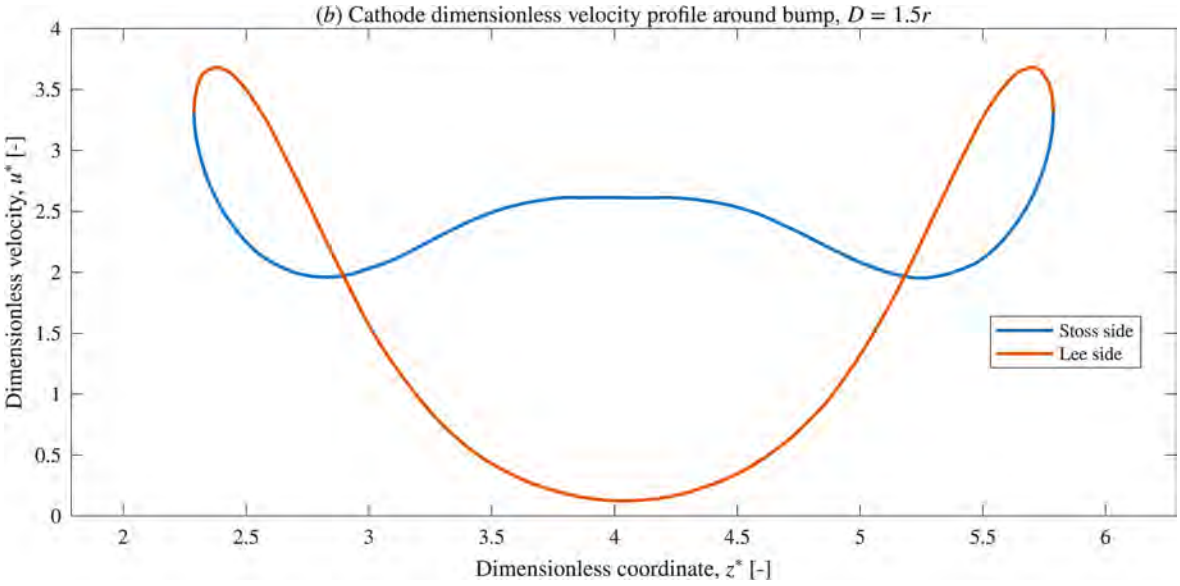

Figure 4.32: Dimensionless cathodic streamwise velocity profile around the representative embossment along path b, corresponding to $D = 1.5r$.

At $D = 1.5r$, the cathodic profile reported in Figure 4.32 continues to show a large difference between the two sides of the embossment.

The lee-side velocity reaches a very low minimum in the central region, demonstrating that the downstream velocity deficit persists away from the immediate solid surface. The stoss-side profile remains considerably higher and reflects the gas transported around the upstream side of the raised feature.

Towards the lateral regions, the velocity progressively recovers as the circumferential path moves away from the selected embossment. The same spatial evolution identified for the anodic flow is therefore observed, although the cathodic stoss–lee contrast remains more pronounced.

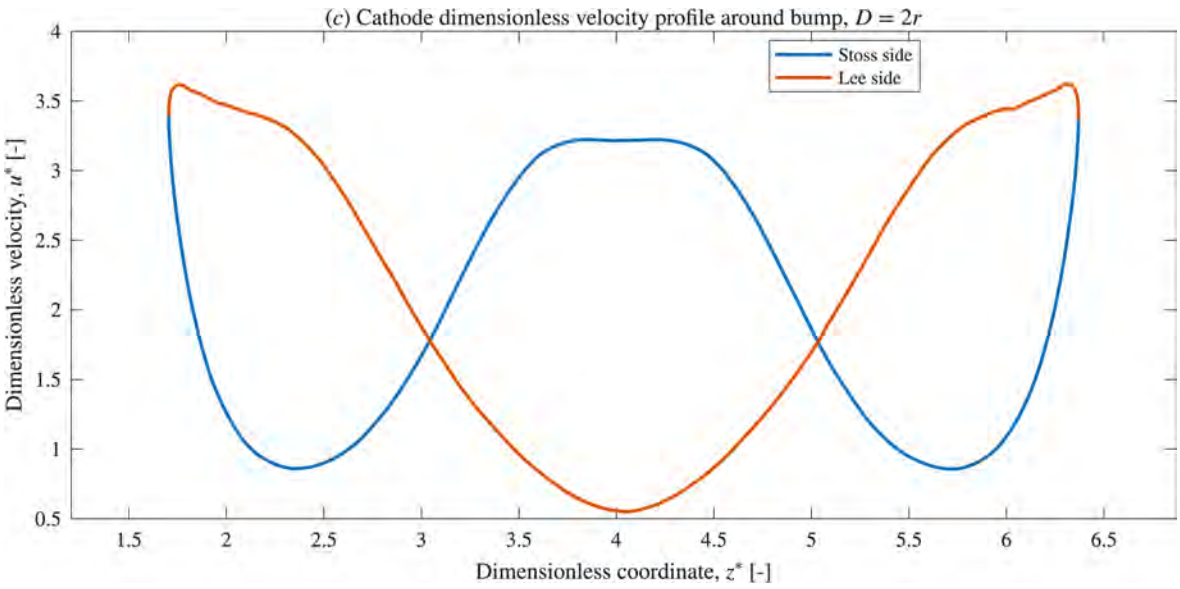

Figure 4.33: Dimensionless cathodic streamwise velocity profile around the representative embossment along path c, corresponding to $D = 2r$.

The profile extracted along path c is shown in Figure 4.33. The central region continues to exhibit a clear stoss–lee asymmetry, with a higher streamwise velocity upstream and a broad velocity deficit downstream of the selected embossment.

At the lateral positions, the profile begins to reflect the influence of the neighbouring embossed features. Streamwise velocity reductions occur as the circumferential path approaches regions in which the adjacent obstacles oppose the principal axial gas motion.

Conversely, higher u^* values are observed in the comparatively open passages between neighbouring embossments. The larger contrast between these preferential passages and the locally restricted regions indicates a stronger relative redistribution of the cathodic flow.

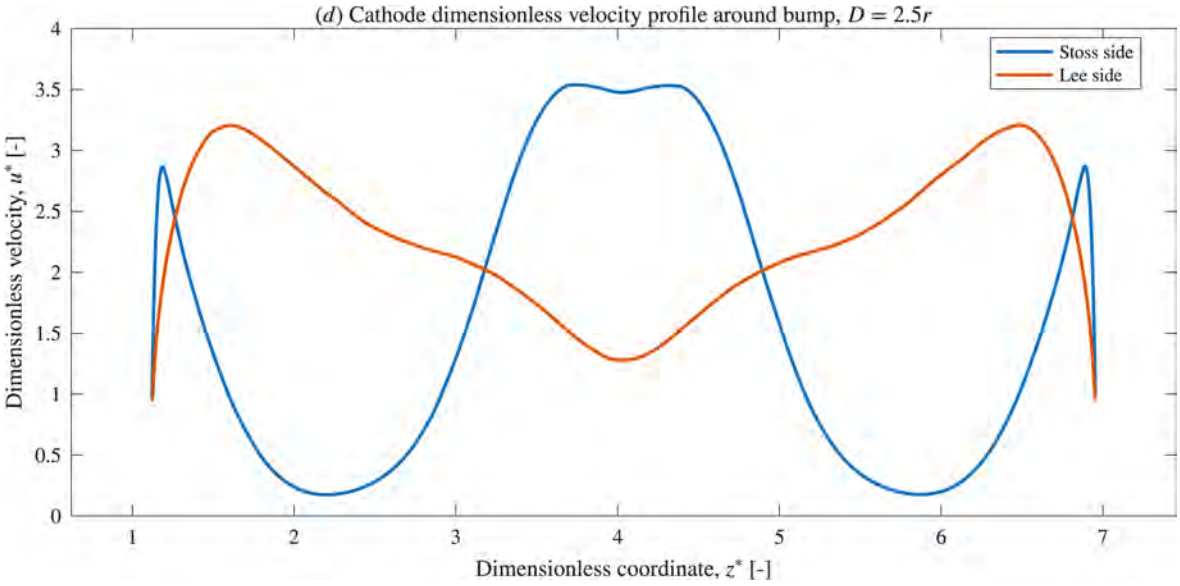

Figure 4.34: Dimensionless cathodic streamwise velocity profile around the representative embossment along path d, corresponding to $D = 2.5r$.

For $D = 2.5r$, the profile reported in Figure 4.34 is strongly influenced by the collective arrangement of the neighbouring embossments.

The central lee-side minimum associated with the selected embossment remains identifiable. However, pronounced lateral velocity reductions also develop where the extraction path approaches the hydraulic influence regions of adjacent raised features.

As discussed for the anodic profiles, these lateral minima are associated with the additional resistance imposed on the streamwise flow by the neighbouring embossments. The gas must redistribute through the available passages around the solid features and the axial velocity component is consequently reduced.

The cathodic profile exhibits a larger contrast between these low-velocity regions and the adjacent preferential passages. The same geometrical mechanism identified on the anodic side is therefore present, but the cathodic operating conditions produce a stronger relative modulation of the streamwise flow.

The comparison between the anodic and cathodic circumferential profiles confirms that the collector topology imposes the same basic spatial organisation in both compartments. The selected embossment generates a central stoss–lee asymmetry, while the neighbouring elements increasingly influence the lateral regions as the extraction radius increases.

The main difference is the intensity of the resulting velocity redistribution. On the cathodic side, the lee-side streamwise velocity approaches zero over a broader region and the contrast between preferential open passages and embossment-influenced regions is more pronounced.

This stronger cathodic flow-path selectivity is consistent with the two-dimensional CO_2 concentration field discussed in Section 4.3.2. The reduced streamwise renewal in the lee-side and locally restricted regions provides the fluid-dynamic basis for the more pronounced carbon dioxide concentration modulation observed around the embossment pattern.

Conversely, the smoother anodic redistribution contributes to the more uniform hydrogen concentration field observed at the anodic channel–porous interface.

4.3.4 Local Velocity Profiles from the Feeding Channel to the Porous Electrode

After analysing the streamwise redistribution of the gas around the embossments, local velocity profiles were extracted along the cross-stream y direction to investigate how the local feeding-channel flow is transmitted to the porous electrode.

The extraction lines extend over the complete feeding-channel height, from the upper solid wall to the channel–porous interface, and subsequently through the porous electrode towards the electrode–matrix interface. At the upper channel boundary, the no-slip condition requires the gas velocity to approach zero. The streamwise channel profiles therefore contain both the near-wall velocity damping and the local redistribution induced by the embossment geometry.

The analysis distinguishes between the streamwise velocity in the feeding channel and the streamwise and cross-stream velocity components inside the porous electrode. This separation is important because the two regions are characterised by markedly different hydraulic resistances and velocity scales. The feeding channel is dominated by axial gas transport, whereas the porous structure strongly attenuates the velocity perturbations transmitted from the channel.

For clarity, different local cross-stream coordinates were adopted for the channel and

porous-medium profiles. In the feeding-channel profiles, the local coordinate y^*_{ch} is referred to the channel–porous electrode interface and increases towards the upper channel wall. In the porous-electrode profiles, instead, the local coordinate y^*_p is referred to the electrode–matrix interface, corresponding to the reactive surface, and increases towards the channel–porous interface. This convention allows each profile to start from $y^* = 0$ within its own region, while preserving the physical distinction between the free-flow and porous domains.

Four representative extraction locations were selected around the same central embossment considered in the circumferential analysis. Their positions are reported in Figure 4.35.

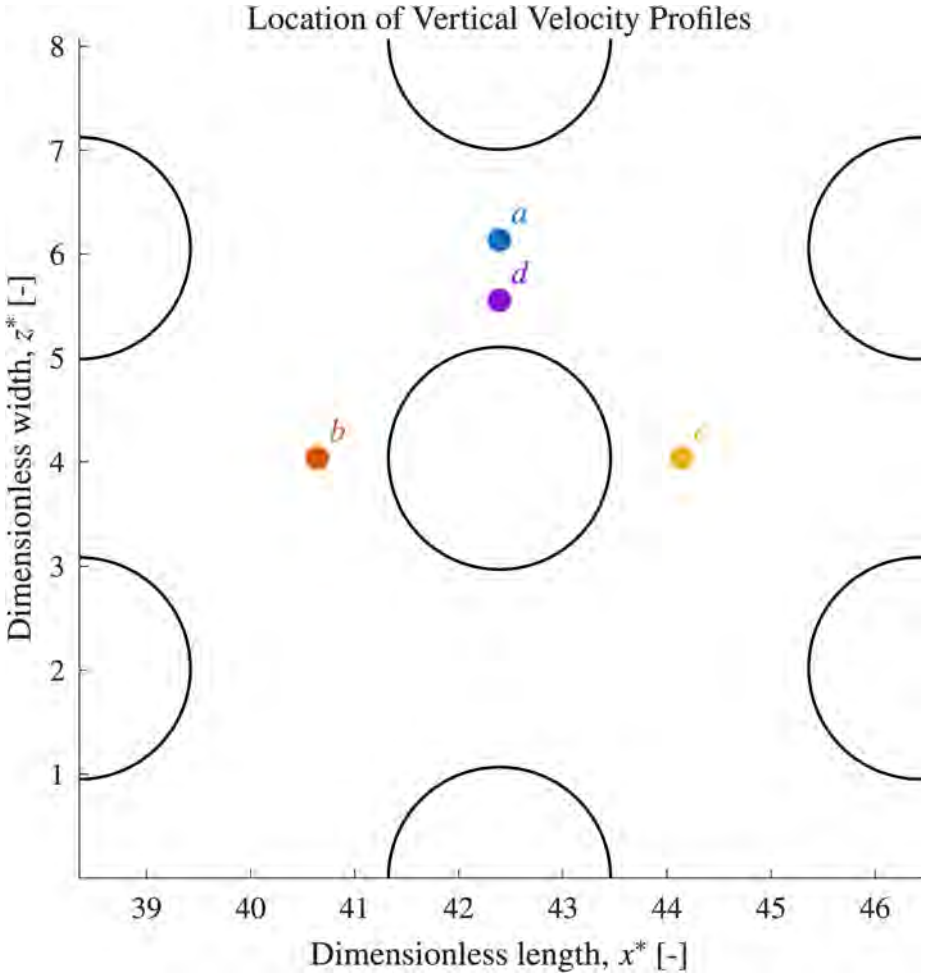

Figure 4.35: Location of the four vertical extraction profiles considered around the representative embossment: point a, between neighbouring embossments; point b, on the stoss side of the embossment; point c, on the lee side of the embossment; and point d, close to the embossment surface.

Point a is located in the open passage between neighbouring embossments. Point b is

positioned on the stoss side of the selected embossment, where the incoming gas directly approaches the raised feature. Point c lies on the lee side and therefore represents a hydraulically screened downstream region. Finally, point d is located close to the embossment and is used to investigate the local flow deflection induced in the immediate vicinity of the solid feature.

Only the anodic profiles are discussed in detail. The corresponding cathodic profiles exhibit the same qualitative transition between streamwise channel transport and porous-medium damping and are therefore not repeated.

The porous-medium profiles are represented over restricted horizontal intervals to resolve the small velocity levels occurring inside the porous electrode. This graphical choice makes small differences visible, but these variations remain limited when compared with the characteristic velocities in the feeding channel. The profiles must therefore be interpreted together with the strong hydraulic resistance imposed by the porous electrode.

Open passage between neighbouring embossments

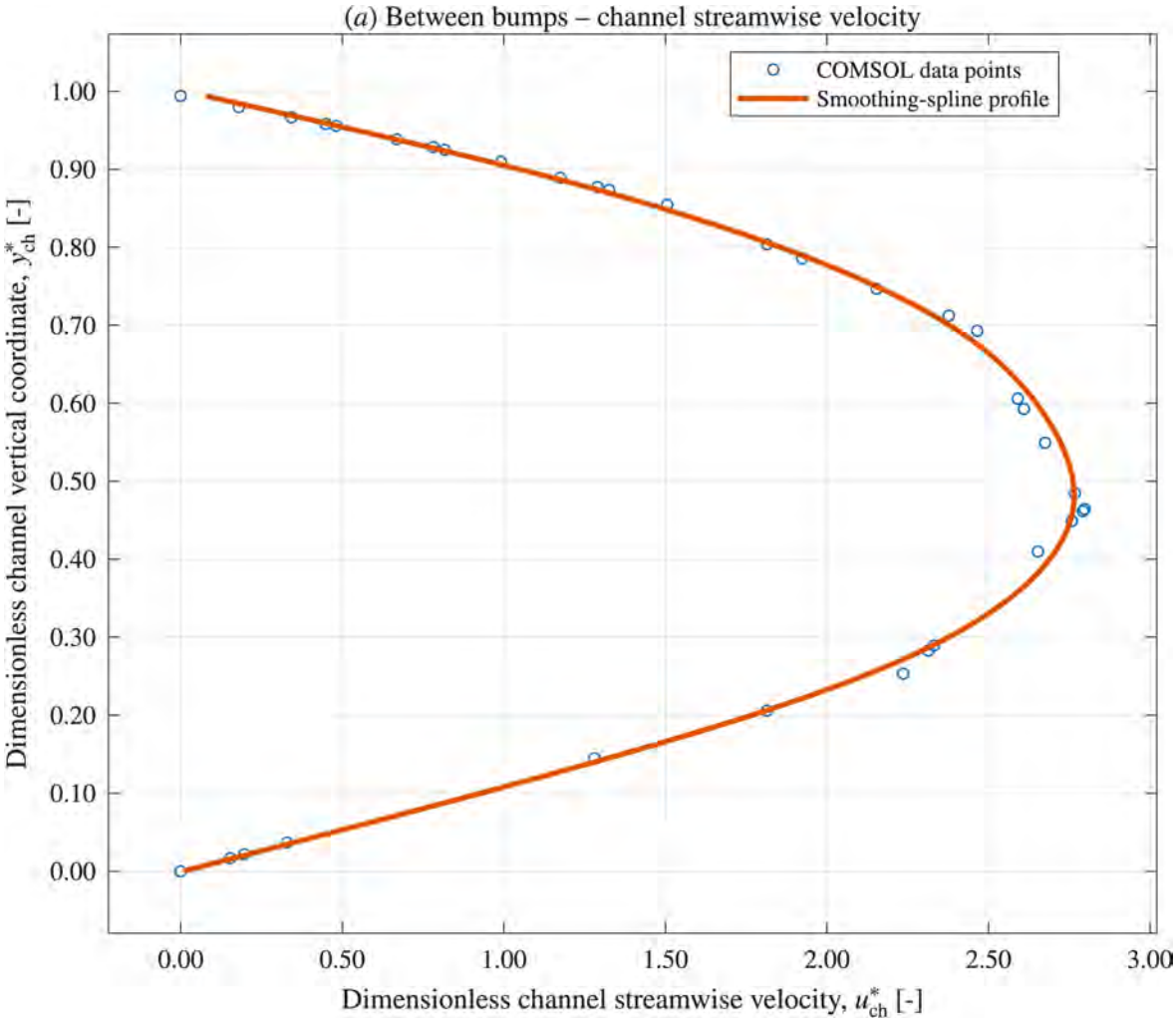

Figure 4.36: Dimensionless anodic streamwise velocity in the feeding channel along the vertical profile at point a, between neighbouring embossments.

The channel streamwise velocity at point a is reported in Figure 4.36. At the upper solid wall, u^*_{ch} approaches zero, consistently with the imposed no-slip boundary condition. Moving away from the wall, the streamwise velocity progressively increases as the influence of the solid boundary decreases.

A maximum value close to $u^*_{ch} = 2.8$ is reached inside the feeding channel. The velocity then decreases towards the channel–porous interface, where the free-flow region interacts with the porous electrode.

The profile therefore shows that the open passage between neighbouring embossments acts as a preferential axial gas path. In this region, the grooved geometry allows a strong streamwise flow to develop in the feeding channel.

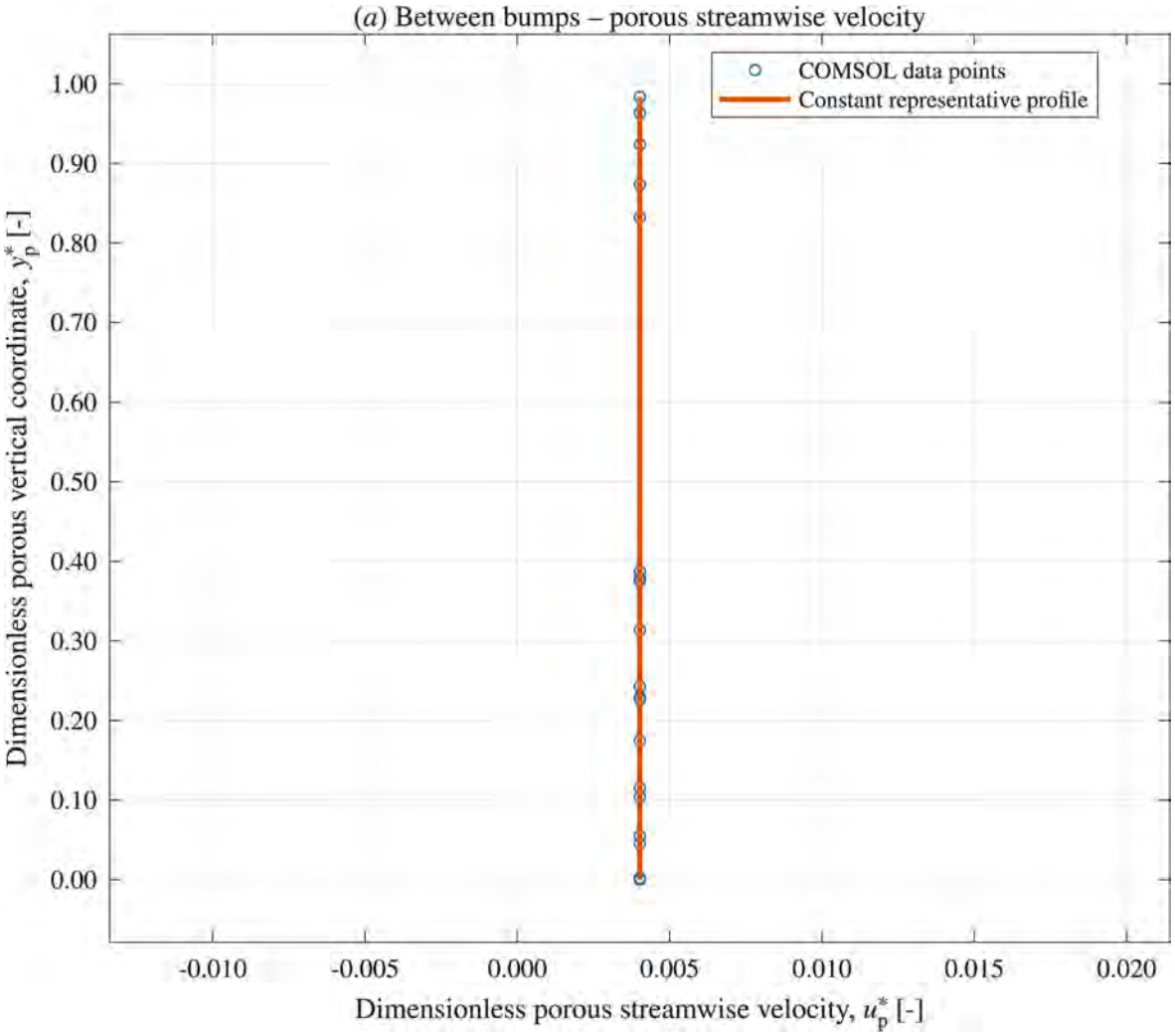

Figure 4.37: Dimensionless anodic streamwise velocity inside the porous electrode along the vertical profile at point a.

The corresponding streamwise component inside the porous electrode is reported in Figure 4.37. Differently from the channel profile, u_p^* remains essentially constant through the porous-electrode thickness.

The representative value is positive and very small, of the order of 10^{-3}. The almost vertical profile indicates that the streamwise velocity component does not develop a significant through-thickness redistribution inside the porous medium.

This result is important because it shows that the strong axial flow observed in the open channel passage is not transmitted into the porous electrode as an internal streamwise circulation. The porous resistance damps the tangential motion and prevents the formation of the kind of streamwise redistribution observed in the traditional collector.

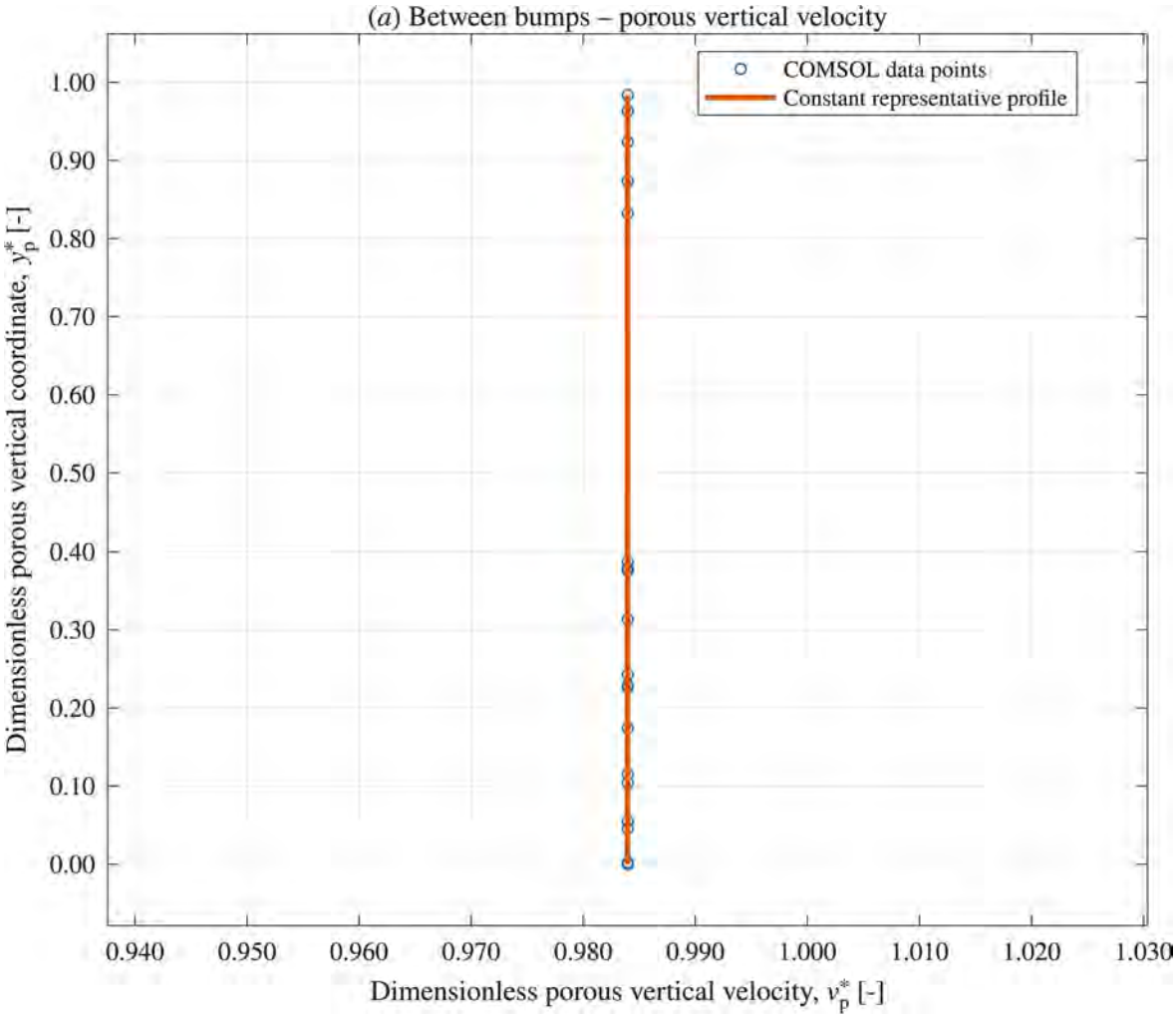

Figure 4.38: Dimensionless anodic cross-stream velocity inside the porous electrode along the vertical profile at point a.

The cross-stream porous velocity at point a is reported in Figure 4.38. The profile is again practically constant through the porous thickness.

The value of v_p^* remains close to unity over the complete profile, with only negligible variations. This indicates that, between neighbouring embossments, the gas penetrates the porous electrode with an almost uniform through-plane velocity.

The simultaneous presence of an almost constant u_p^* and an almost constant v_p^* confirms that the open passage does not generate internal recirculation cells in the porous electrode. Instead, the porous flow is dominated by a stable through-plane penetration towards the reactive surface.

Stoss side of the embossment

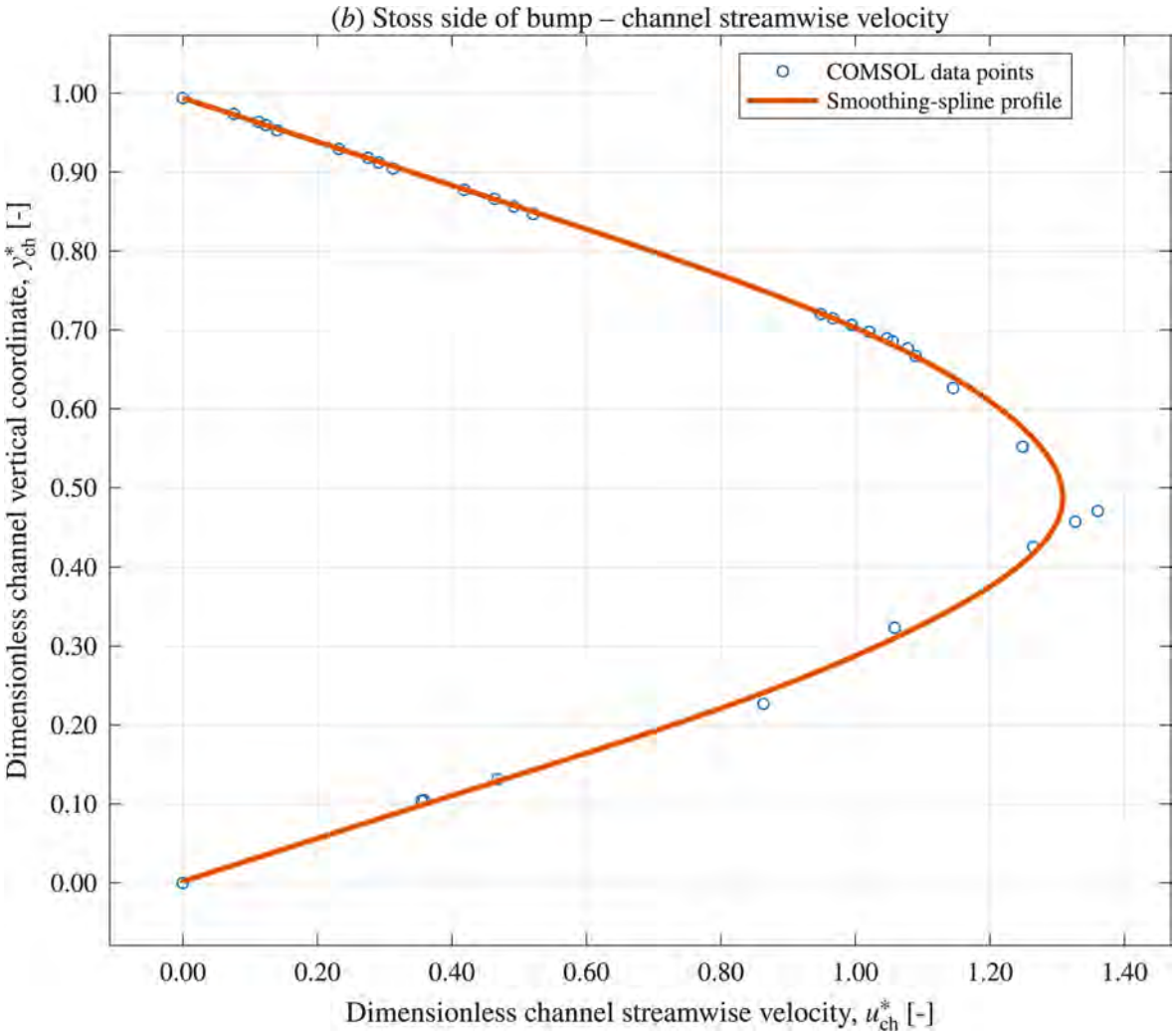

Figure 4.39: Dimensionless anodic streamwise velocity in the feeding channel along the vertical profile at point b, on the stoss side of the representative embossment.

The streamwise channel velocity at the stoss-side point is shown in Figure 4.39. Close to the upper solid wall, u^*_{ch} remains low as a consequence of the no-slip condition. The velocity progressively increases when moving towards the channel interior and reaches a maximum close to 1.3.

The maximum value is substantially lower than that obtained between neighbouring embossments. This difference reflects the direct interaction between the incoming gas and the upstream side of the raised feature.

The embossment modifies the available axial path and redirects part of the incoming stream around the solid obstacle. The streamwise component is therefore reduced compared with the preferential open passage identified at point a.

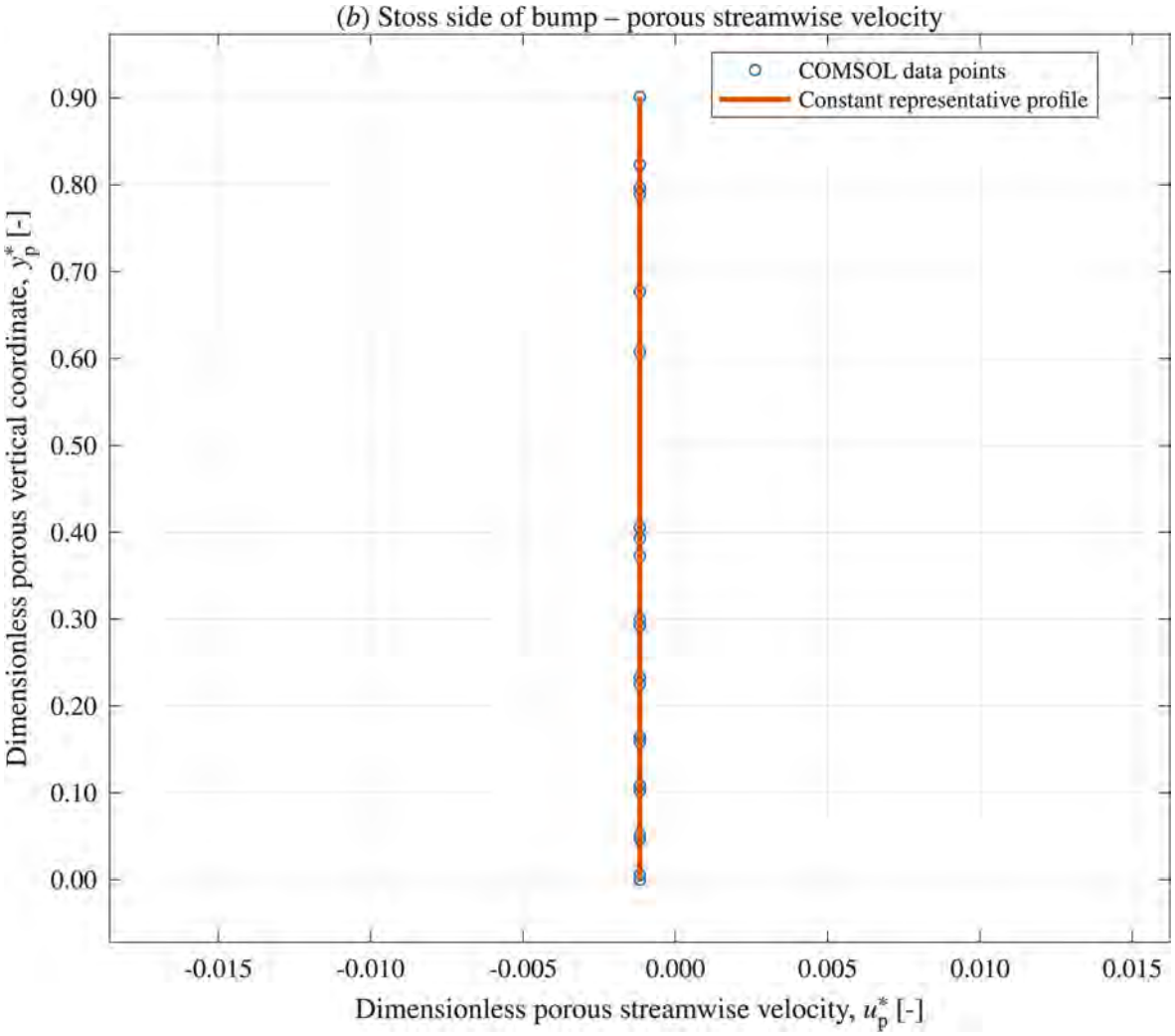

Figure 4.40: Dimensionless anodic streamwise velocity inside the porous electrode along the vertical profile at point *b*.

Inside the porous electrode, the streamwise component at the stoss side is reported in Figure 4.40. The profile is almost perfectly vertical, indicating that u_p^* is essentially constant along the porous thickness.

The representative value is slightly negative and very small in magnitude. This does not indicate a developed recirculation cell. Rather, it reflects a weak local tangential redistribution associated with the pressure perturbation generated by the embossment.

The important point is that the sign and magnitude of u_p^* remain practically unchanged through the electrode thickness. Therefore, the stoss-side perturbation affects only the local representative value of the streamwise component, without producing a structured internal recirculation inside the porous domain.

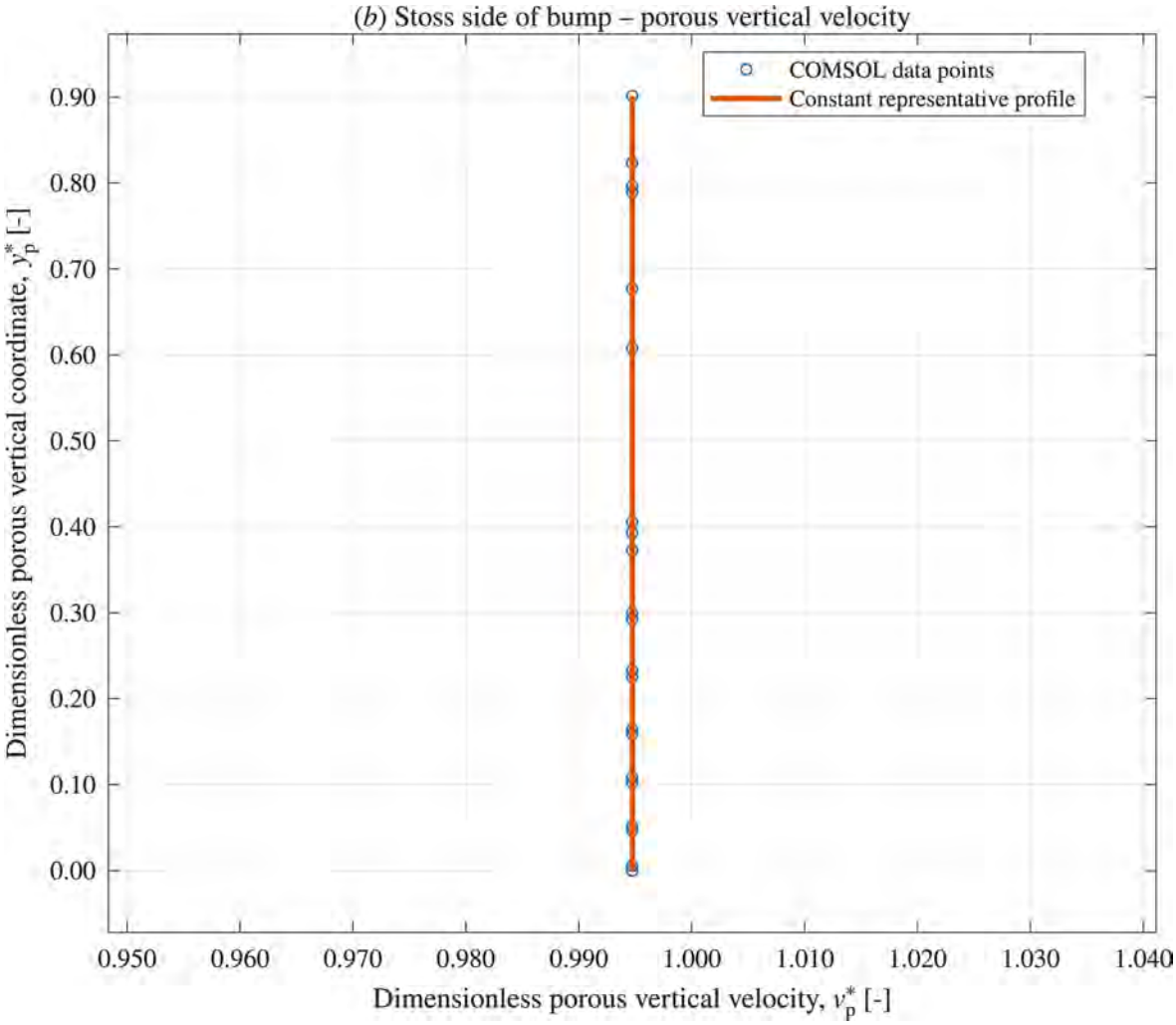

Figure 4.41: Dimensionless anodic cross-stream velocity inside the porous electrode along the vertical profile at point *b*.

The corresponding cross-stream velocity profile is shown in Figure 4.41. As observed for the streamwise component, the cross-stream velocity remains nearly constant through the porous electrode.

The value of v_p^* is close to unity and exhibits only negligible variations along y_p^*. The profile therefore indicates that the pressure perturbation generated at the stoss side of the embossment does not produce an appreciable through-thickness distortion of the porous flow.

Compared with the traditional collector, this behaviour is significant. In the grooved configuration, even where the incoming flow directly interacts with the raised feature, the porous electrode does not show evidence of internal recirculation cells. The flow remains predominantly through-plane and spatially regular inside the porous layer.

Lee side of the embossment

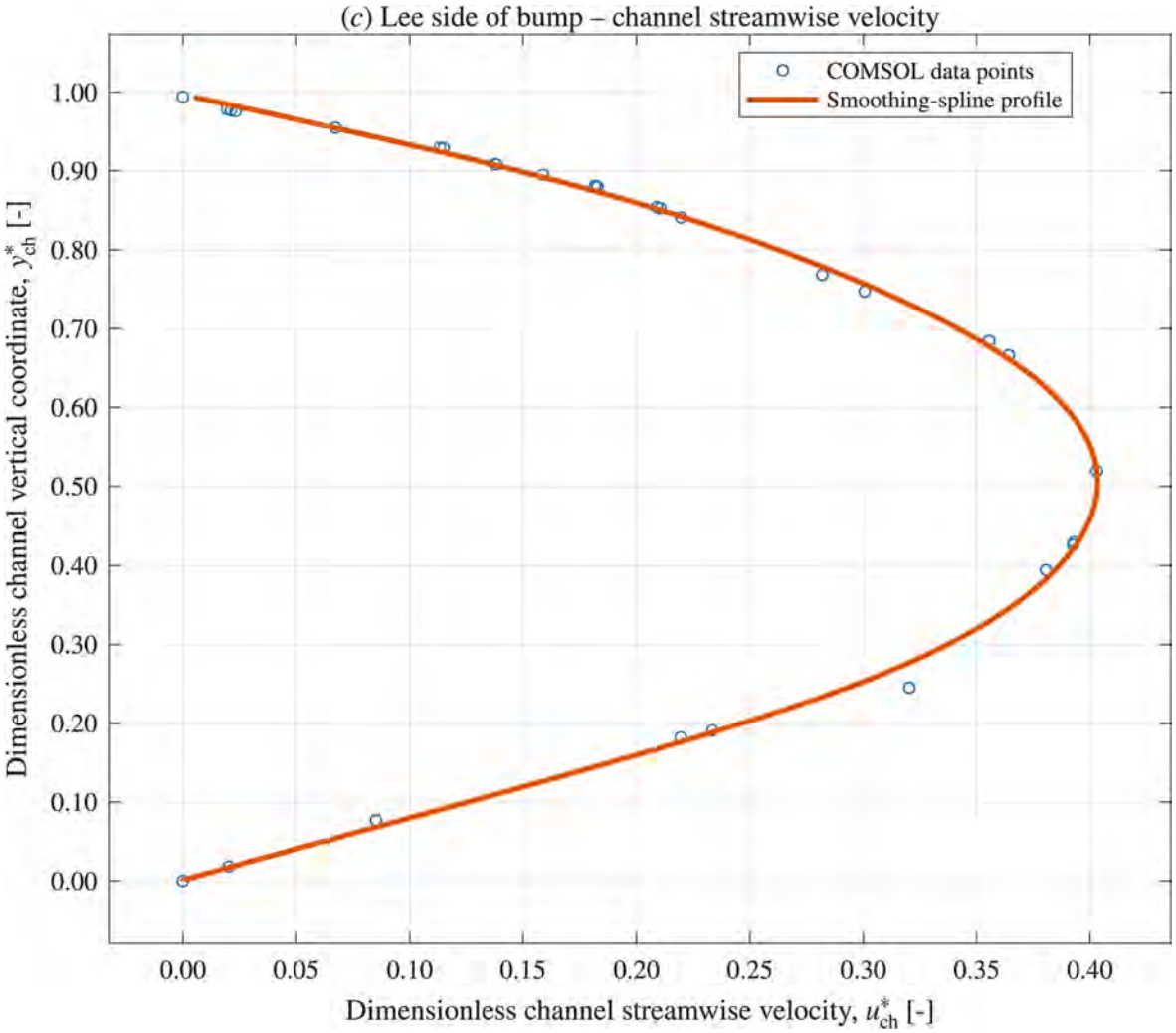

Figure 4.42: Dimensionless anodic streamwise velocity in the feeding channel along the vertical profile at point c, on the lee side of the representative embossment.

The streamwise channel velocity at point c is reported in Figure 4.42. The velocity approaches a low value at the upper solid wall, consistently with the no-slip condition, and increases towards the channel interior.

However, the maximum streamwise velocity remains close to 0.4, considerably lower than at the other analysed positions. The lee-side region therefore exhibits a pronounced axial velocity deficit.

This result confirms the hydraulic shielding generated downstream of the embossment. The region is less directly connected to the incoming main stream and receives a weaker axial gas renewal.

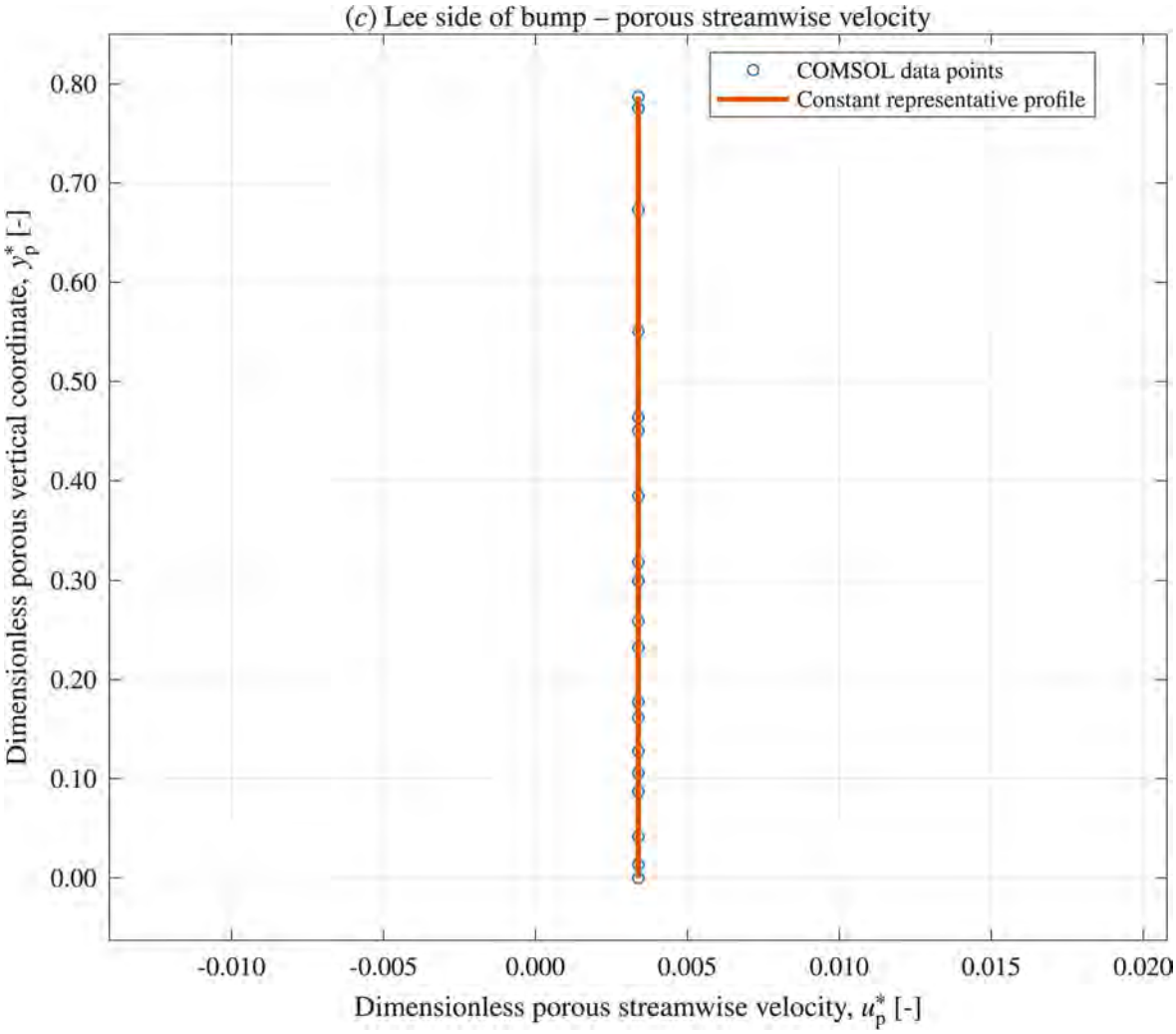

Figure 4.43: Dimensionless anodic streamwise velocity inside the porous electrode along the vertical profile at point c.

Inside the porous electrode, the streamwise component at the lee side is reported in Figure 4.43. Despite the strong velocity deficit observed in the feeding channel, the porous profile remains nearly constant through the electrode thickness.

The value of u_p^* is small and positive, with no meaningful variation along y_p^*. This indicates that the lee-side shielding affects the local level of the velocity entering the porous electrode, but it does not generate a through-thickness streamwise redistribution.

The absence of sign changes or profile curvature is particularly relevant. In the traditional collector, shielded regions were associated with internal redistribution cells and local streamwise reversals inside the porous electrode. In the grooved configuration, instead, the lee-side profile remains uniform, showing that the porous layer damps the channel-scale disturbance before it can develop into a recirculation pattern.

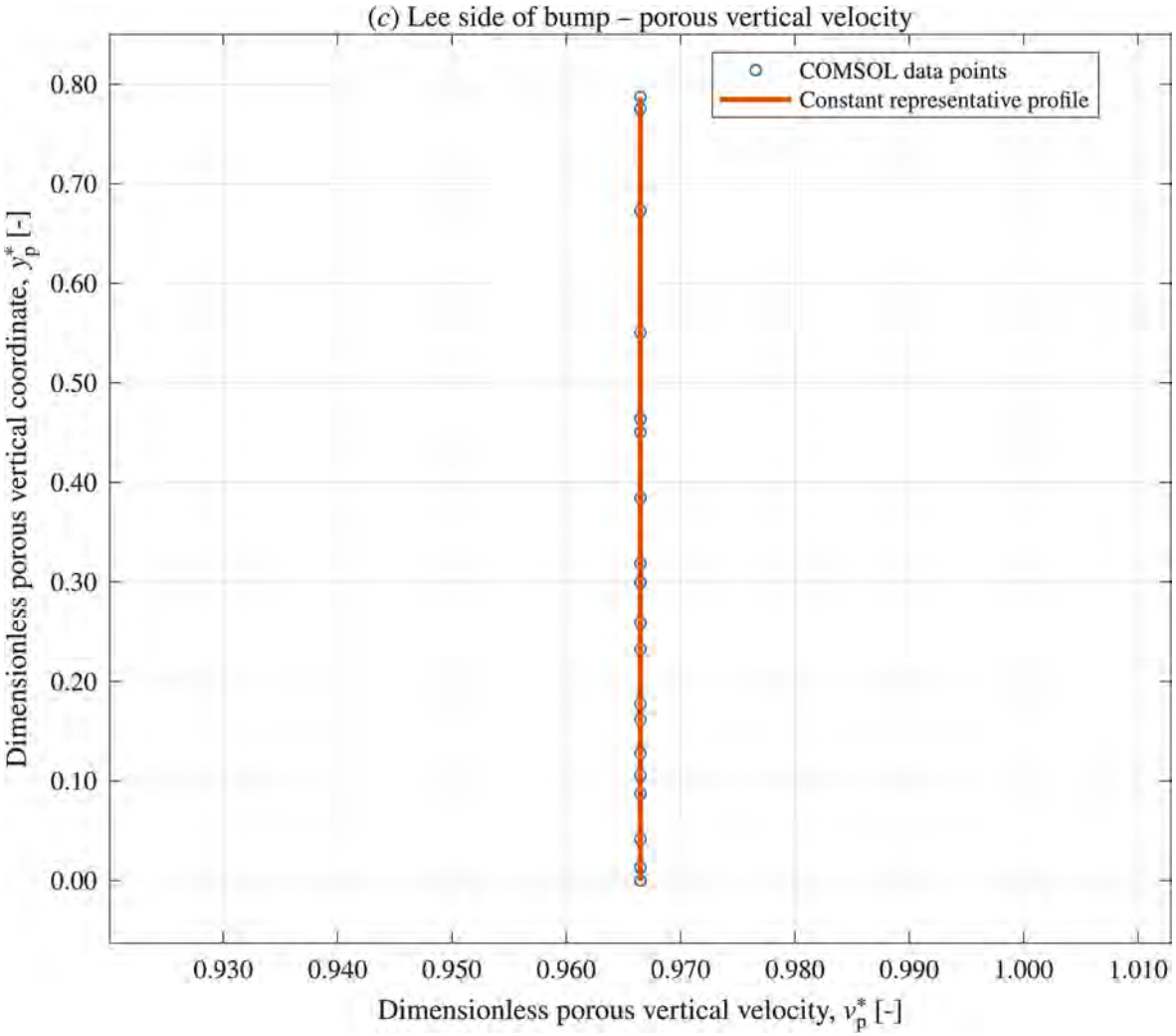

Figure 4.44: Dimensionless anodic cross-stream velocity inside the porous electrode along the vertical profile at point *c*.

The cross-stream porous velocity at the lee-side point is shown in Figure 4.44. The profile is again essentially constant through the porous thickness.

The representative value of v_p^* is slightly lower than at the other analysed locations, consistently with the weaker hydraulic supply in the lee-side region. However, the profile does not show a significant through-thickness decrease or local distortion.

This means that the hydraulic shadow generated downstream of the embossment is transmitted to the porous electrode mainly as a lower local level of cross-stream velocity, rather than as a strongly non-uniform internal flow structure. The porous medium therefore smooths the local channel disturbance while preserving a reduced but regular through-plane supply.

Immediate vicinity of the embossment

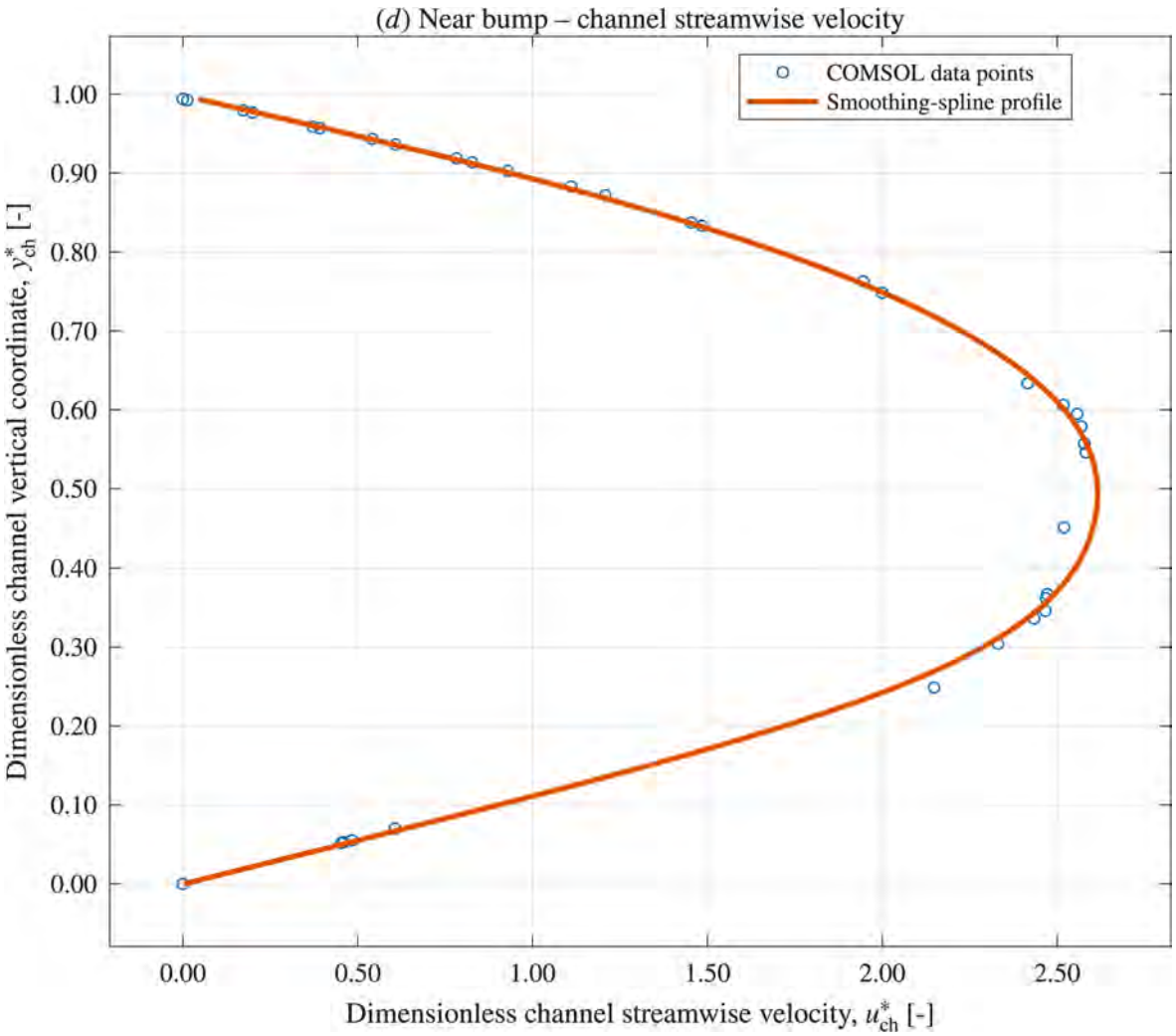

Figure 4.45: Dimensionless anodic streamwise velocity in the feeding channel along the vertical profile at point d, in the immediate vicinity of the representative embossment.

The streamwise channel velocity in the immediate vicinity of the embossment is reported in Figure 4.45. The velocity remains low close to the upper solid wall, consistently with the no-slip condition, and progressively increases towards the channel interior.

A maximum value of approximately 2.6 develops inside the channel. The high local streamwise velocity reflects the deflection of the feeding stream around the embossment.

The gas cannot cross the solid raised feature and is therefore redirected through the adjacent available flow region. This local reduction in available flow passage produces a strong axial acceleration close to the embossment.

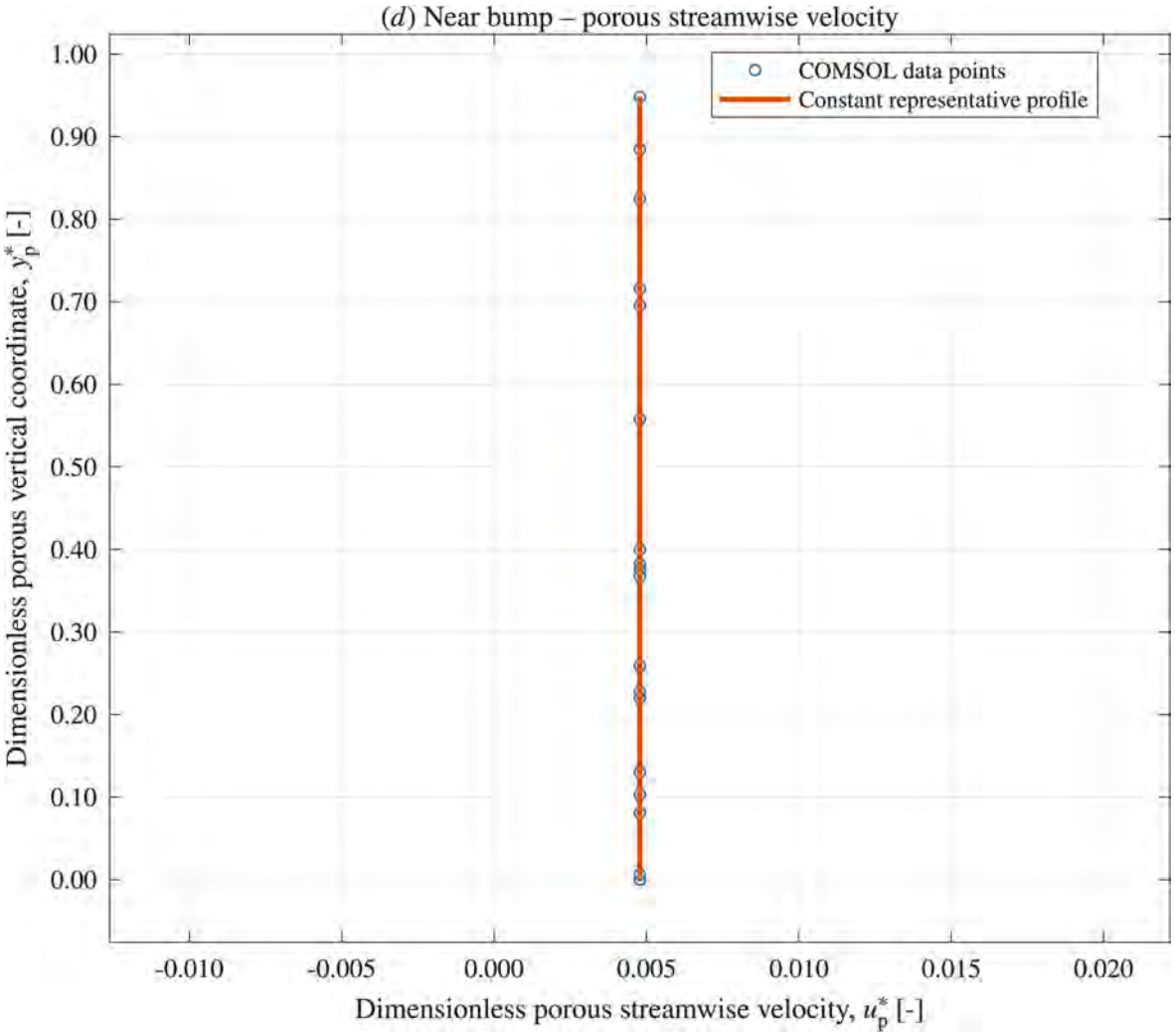

Figure 4.46: Dimensionless anodic streamwise velocity inside the porous electrode along the vertical profile at point d.

Inside the porous electrode, the streamwise component close to the bump is reported in Figure 4.46. Although the adjacent channel flow exhibits a strong acceleration, the porous profile remains almost constant through the electrode thickness.

The value of u_p^* is small and positive, of the order of 10^{-3}. The absence of a developed profile indicates that the local tangential perturbation generated by the channel flow is strongly damped at the entrance of the porous medium.

This result confirms that the grooved geometry does not transmit the channel-scale acceleration into the porous electrode as an internal streamwise circulation. The porous layer acts as a hydraulic damper and converts the highly non-uniform channel flow into a regular porous-medium velocity field.

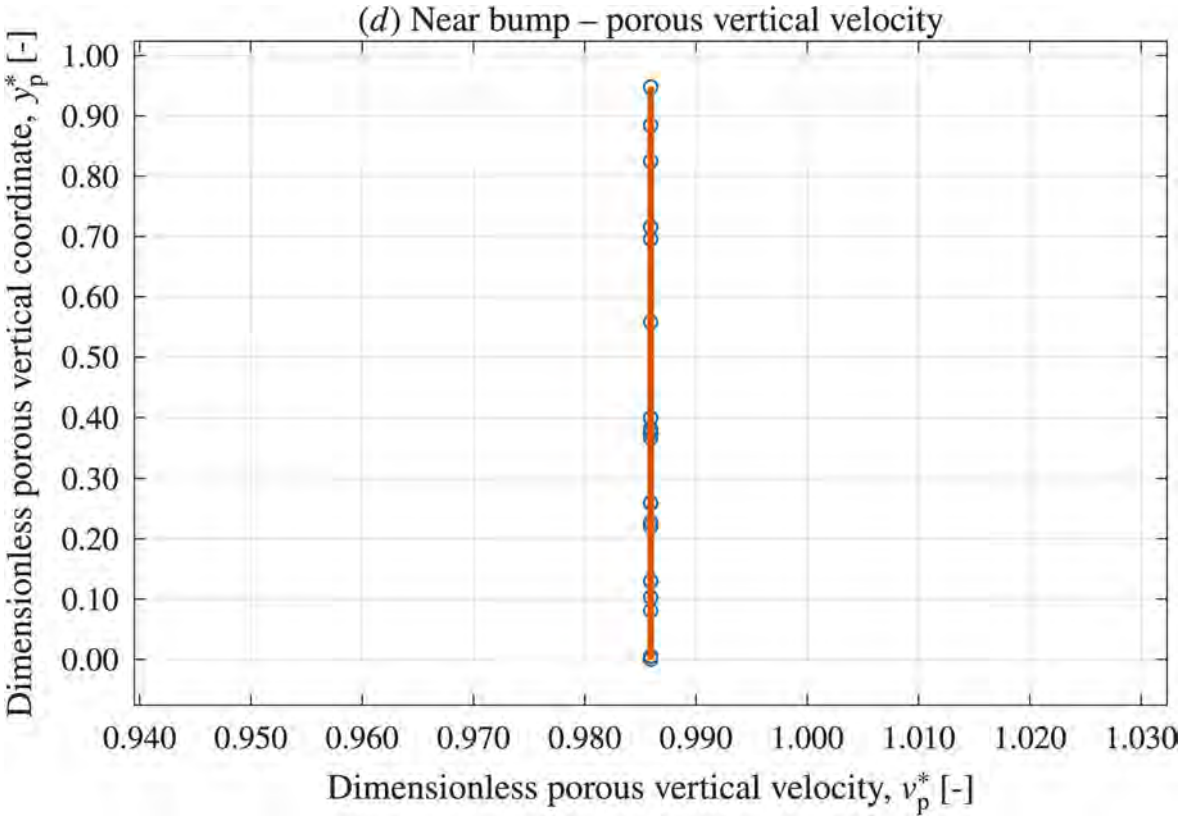

Figure 4.47: Dimensionless anodic cross-stream velocity inside the porous electrode along the vertical profile at point d.

The cross-stream porous velocity at point d is reported in Figure 4.47. The profile is almost vertical, confirming that v_p^* remains approximately constant through the porous-electrode thickness.

The representative value is close to unity and comparable with the other non-shielded locations. This indicates that, despite the strong local acceleration of the channel flow near the embossment, the through-plane velocity inside the porous medium remains regular.

The result further confirms the strong damping action of the porous electrode. The local acceleration and deflection generated in the feeding channel are not transformed into a recirculating motion inside the porous domain.

Transition from channel flow to porous-medium damping

The four extraction locations collectively show that the grooved collector generates substantial spatial variations in the feeding-channel streamwise velocity but almost

constant velocity profiles inside the porous electrode.

In the feeding channel, all profiles approach low velocity values at the upper solid wall, consistently with the imposed no-slip boundary condition. Moving away from the wall, the streamwise velocity increases and develops a local distribution controlled by the collector geometry.

The maximum dimensionless streamwise velocity ranges from approximately 0.4 on the lee side to values above 2.5 between or immediately adjacent to the embossments. The grooved geometry therefore strongly redistributes the principal axial gas flow and generates preferential passages and hydraulically screened regions.

Inside the porous electrode, instead, the high hydraulic resistance strongly attenuates the disturbances transmitted from the feeding channel. Both the streamwise and cross-stream velocity components remain nearly constant through the porous thickness at all analysed locations.

This behaviour represents a major difference with respect to the traditional current collector. In the traditional configuration, the communication between the feeding channel and the porous electrode occurs through discrete openings and limited passages defined by the arched geometry. The gas is therefore forced to enter the porous electrode through specific access regions and subsequently redistribute laterally and streamwise towards the shielded areas. This mechanism promotes internal redistribution and can generate local recirculation-like cells inside the porous layer.

In the grooved configuration, instead, the available gas-access area towards the porous electrode is significantly larger and more continuously distributed. The gas is therefore not forced to pass through a limited number of specific openings, but can penetrate the porous electrode over a broader portion of the channel-facing surface. As a consequence, the local hydraulic forcing is more evenly distributed, and the formation of internal recirculation cells is avoided.

The porous profiles confirm this behaviour. They do not show comparable through-thickness variations, local extrema or sign-changing structures. Both u_p^* and v_p^* remain nearly constant along the porous thickness, indicating that the grooved geometry promotes a more regular transition from the feeding channel to the porous electrode.

The small differences among the porous profiles mainly affect the local representative value of the velocity, rather than its variation through the electrode thickness. The stoss side, lee side, open passage and near-bump region can therefore exhibit slightly different local velocity levels, but the flow remains approximately uniform along y_p^*.

The absence of developed streamwise reversals and the quasi-constant cross-stream velocity profiles indicate that internal recirculation cells are not formed inside the porous electrode. This is mainly related to the larger and more continuously distributed gas-access area provided by the grooved collector. Since the gas is supplied to the porous electrode over a broader interface, the flow does not need to be redistributed from a few discrete openings towards shielded regions, as occurred in the traditional configuration.

The porous domain therefore acts as a strong hydraulic damper: it receives a spatially modulated supply from the channel, but the larger available access area prevents the development of localised internal circulation patterns and favours a much more regular through-plane motion.

This result is favourable from the transport point of view. A more uniform porous-medium velocity field reduces the tendency for local gas trapping or recirculation inside the electrode and supports a more regular reactant supply towards the reactive surface.

This analysis therefore provides the basis for the two-dimensional evaluation of the vertical convective and diffusive species fluxes presented in the following subsection.

4.3.5 Vertical Transport inside the Porous Electrodes

After examining the local transition from the streamwise channel flow to the channel–porous interface, the transport occurring inside the porous electrodes was investigated. In this region, the strong hydraulic resistance of the porous structure suppresses the axial gas motion observed in the feeding channel and makes transport through the electrode thickness increasingly relevant.

The analysis was therefore focused on the vertical transport of the limiting reactants through the porous electrodes. Two contributions were considered separately: the convective flux associated with the local gas motion and the diffusive flux generated

by the concentration gradient of the reacting species. On the anodic side, the analysis refers to H_2, whereas on the cathodic side it refers to CO_2, consistently with the limiting reactants adopted for the non-dimensionalisation of the species concentration.

Before analysing the species transport fields, the pressure distribution inside the porous electrodes was considered. This is necessary because the vertical convective contribution is influenced by the pressure field transmitted from the feeding channel to the porous domain. The section-averaged pressure profiles and the corresponding local pressure-fluctuation fields are reported for both the anodic and cathodic porous electrodes.

Pressure distribution inside the porous electrodes

The pressure field inside the porous electrodes was analysed using two complementary quantities. First, the section-averaged dimensionless pressure, $\overline{p}^*(x)$, was evaluated along the streamwise direction by averaging the local pressure over the spanwise coordinate at each axial position. This quantity describes the global hydraulic evolution along the porous electrode and includes any pressure modulation that is coherent over the section.

Second, a local residual pressure-fluctuation field was computed as

$$p'^*(x,z) = p^*(x,z) - \overline{p}^*(x). \tag{4.5}$$

This operation removes the section-averaged contribution at each axial position and isolates the residual local deviation around the mean profile. It is therefore important to interpret the fluctuation maps together with the corresponding mean-pressure profiles. If the collector-induced perturbation is already strongly represented in $\overline{p}^*(x)$, subtracting the section average also removes part of the periodic geometrical contribution from the two-dimensional residual field.

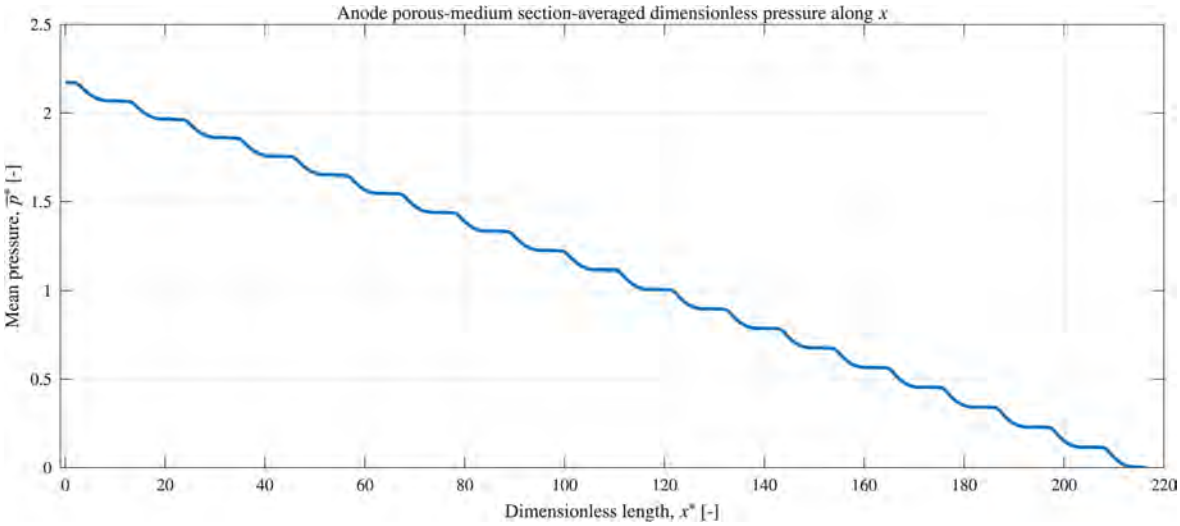

Figure 4.48: Section-averaged dimensionless pressure along the anodic porous electrode.

The section-averaged anodic pressure reported in Figure 4.48 exhibits an almost monotonic decrease along the streamwise direction. The mean pressure progressively decreases from the inlet towards the outlet, reflecting the global pressure loss associated with gas transport through the cell.

Weak periodic oscillations are superimposed on this global decrease. Their wavelength is associated with the periodic distribution of the embossments, showing that the porous electrode retains a hydraulic signature of the collector geometry. However, in the anodic case, this modulation remains small compared with the overall pressure decay. The main contribution to $\overline{p}^*(x)$ is therefore the global inlet-to-outlet pressure loss, while the geometry-induced perturbations remain predominantly local.

This behaviour indicates that, on the anodic side, the periodic pressure disturbances generated by the collector are not strongly embedded in the section-averaged pressure profile. Consequently, the two-dimensional fluctuation field is particularly useful to visualise the local pressure redistribution induced by the embossment pattern.

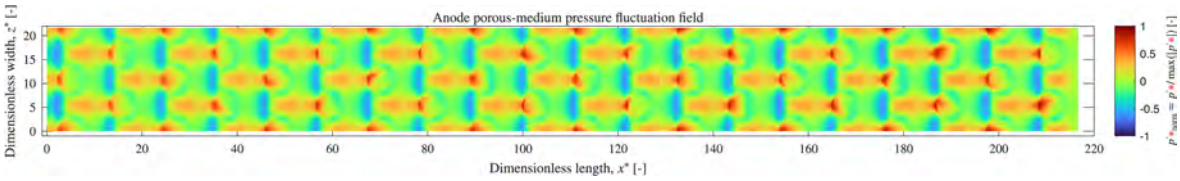

Figure 4.49: Dimensionless residual pressure-fluctuation field inside the anodic porous electrode.

The anodic residual pressure-fluctuation field shown in Figure 4.49 highlights the local pressure redistribution associated with the collector geometry. Since the global axial pressure decrease has been removed, the map emphasises the periodic alternation of positive and negative deviations around the local section-averaged value.

The field exhibits a regular spatial organisation linked to the projected embossment pattern. Positive-pressure regions are observed near the areas where the gas tends to accumulate or where the local flow is redirected by the solid features. Negative-pressure regions occur in neighbouring zones where the local pressure is lower than the section-averaged value. The resulting pattern confirms that the collector-induced hydraulic perturbation is transmitted from the feeding channel into the porous electrode.

The use of a uniform colour scale makes the amplitude of the residual perturbations directly comparable between different pressure-fluctuation maps. In the anodic case, the residual field remains clearly structured, confirming that the local geometrical effect is not completely captured by the mean profile and must be analysed through the two-dimensional distribution.

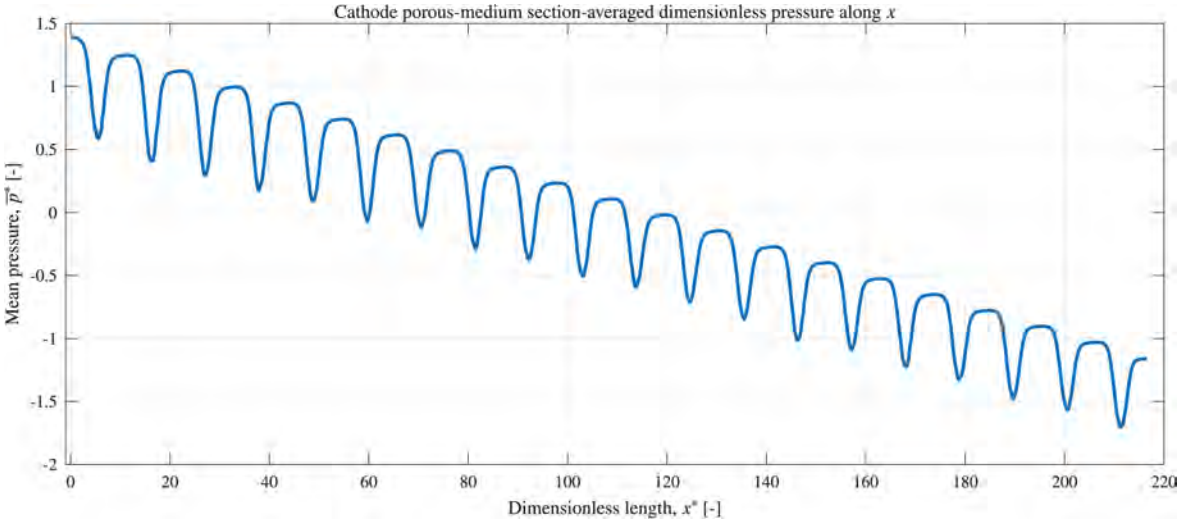

Figure 4.50: Section-averaged dimensionless pressure along the cathodic porous electrode.

The corresponding cathodic pressure profile is reported in Figure 4.50. As on the anodic side, the mean pressure decreases along the cell. However, the cathodic profile is characterised by much stronger periodic oscillations superimposed on the global pressure decrease.

The repeated pressure minima are associated with the periodic collector geometry

and indicate that the cathodic pressure field is more strongly affected by the local interaction between the gas stream and the embossments. In contrast to the anodic case, a significant part of the geometry-induced perturbation is already included in the section-averaged pressure profile $\overline{p}^*(x)$.

This point is essential for the interpretation of the corresponding two-dimensional fluctuation field. Since the cathodic mean profile already contains a strong periodic component, the subtraction of $\overline{p}^*(x)$ removes not only the global axial pressure decrease, but also a relevant part of the periodic pressure modulation induced by the collector. Therefore, the residual pressure-fluctuation map must not be interpreted as indicating a weaker cathodic perturbation. On the contrary, the cathodic porous electrode is more strongly influenced by the collector geometry, but this influence is already evident in the section-averaged pressure profile.

The stronger cathodic modulation is consistent with the higher characteristic cathodic flow intensity and with the stronger hydraulic interaction between the gas stream and the raised collector features. The effect of the embossments is therefore not restricted to local residual fluctuations, but affects the section-averaged hydraulic evolution along the porous cathode.

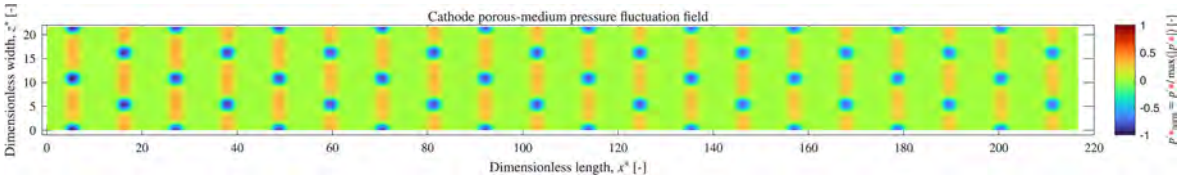

Figure 4.51: Dimensionless residual pressure-fluctuation field inside the cathodic porous electrode.

The cathodic residual pressure-fluctuation field reported in Figure 4.51 represents the local deviation from the already strongly modulated section-averaged pressure profile. As a result, the map mainly displays the residual local deviations that remain after removal of the dominant periodic contribution contained in $\overline{p}^*(x)$.

For this reason, the cathodic residual field should not be compared with the anodic map by considering only the apparent intensity of the colour pattern. The pressure perturbation induced by the collector is stronger on the cathodic side, but it is distributed between two components: a large periodic contribution included in the section-averaged

pressure profile and a residual local contribution visible in the fluctuation map.

The comparison between the anodic and cathodic pressure results therefore shows two different behaviours. In the anode, the mean pressure is mainly governed by a smooth axial decay, while the local collector-induced perturbation is more clearly visible in the residual two-dimensional field. In the cathode, the mean pressure itself contains a strong periodic modulation, so that the residual fluctuation field represents only the part of the local pressure redistribution that is not already captured by the section-averaged profile.

Additional post-processing based on a uniform grid confirmed that the strong periodic cathodic oscillations are not an artefact of the averaging procedure. They are an intrinsic feature of the cathodic pressure field and indicate that the porous cathode experiences a stronger geometrical hydraulic forcing than the porous anode.

The pressure fields therefore provide the hydraulic background required to interpret the vertical convective species-flux distributions. In particular, the pressure analysis shows that the collector geometry affects both the local residual pressure field and, especially on the cathodic side, the section-averaged hydraulic evolution along the porous electrode.

Vertical convective and diffusive fluxes

The vertical transport of the limiting species was analysed in terms of species fluxes rather than velocity components. The convective contribution represents the vertical transport of species i associated with the local gas motion, while the diffusive contribution represents the transport generated by the concentration gradient through the porous electrode.

The dimensional vertical convective flux of species i was non-dimensionalised using the reference scale

$$J_{\mathrm{conv},i,\mathrm{ref}} = c_{i,\mathrm{ref}} M_i U_p, \tag{4.6}$$

where $c_{i,\mathrm{ref}}$ is the reference concentration of the considered species, M_i is its molar mass and U_p is the characteristic velocity in the porous electrode. The dimensionless vertical

convective flux is therefore

$$J^*_{\mathrm{conv},i,y} = \frac{J_{\mathrm{conv},i,y}}{c_{i,\mathrm{ref}} M_i U_p}. \tag{4.7}$$

The vertical diffusive flux was instead non-dimensionalised using a diffusive reference scale based on the porous-electrode thickness:

$$J_{\mathrm{diff},i,\mathrm{ref}} = \frac{D_{i,\mathrm{ref}} c_{i,\mathrm{ref}} M_i}{H_p}, \tag{4.8}$$

where $D_{i,\mathrm{ref}}$ is the reference diffusivity of the species and H_p is the porous-electrode thickness. The corresponding dimensionless diffusive flux is

$$J^*_{\mathrm{diff},i,y} = \frac{J_{\mathrm{diff},i,y}}{D_{i,\mathrm{ref}} c_{i,\mathrm{ref}} M_i / H_p}. \tag{4.9}$$

The reference diffusivities used for the diffusive flux scaling were taken as representative mean values for the corresponding limiting species in the porous electrode. In particular, the values adopted in the post-processing were

$$D_{\mathrm{H_2,ref}} = 7.3711 \times 10^{-4}\ \mathrm{m^2\,s^{-1}}, \tag{4.10}$$

for hydrogen on the anodic side, and

$$D_{\mathrm{CO_2,ref}} = 9.6508 \times 10^{-5}\ \mathrm{m^2\,s^{-1}}, \tag{4.11}$$

for carbon dioxide on the cathodic side. These values correspond to 7.3711 $\mathrm{cm^2\,s^{-1}}$ for H_2 and 0.96508 $\mathrm{cm^2\,s^{-1}}$ for CO_2, respectively.

The difference between the two reference diffusivities is important for the interpretation of the flux fields. Hydrogen is characterised by a substantially larger diffusivity than carbon dioxide; therefore, local concentration non-uniformities tend to be smoothed more effectively on the anodic side. Conversely, the lower diffusivity of CO_2 contributes to preserving sharper concentration gradients inside the cathodic porous electrode, making the wake-like structures induced by the collector geometry more evident in

the diffusive flux field. This formulation makes it possible to compare the spatial organisation of convective and diffusive species transport using scales representative of each mechanism. The convective maps describe where the species is transported by the gas penetrating the porous electrode, while the diffusive maps identify the regions where concentration gradients drive the reactant towards the reactive surface.

It is important to underline that the sign and direction of the convective and diffusive contributions must be interpreted according to the adopted cross-stream coordinate convention and to the electrochemical stoichiometry of each electrode.

On the anodic side, H_2 is consumed at the reactive surface, and the diffusive flux is therefore directed towards the reaction zone. In the adopted convention, this appears as a negative vertical diffusive flux over most of the anodic porous electrode. The convective contribution, however, is affected not only by the pressure-driven gas penetration from the channel, but also by the local gas-phase balance at the anode. Since the anodic reaction consumes H_2 but produces H_2O and CO_2, the reactive surface is associated with a net generation of gaseous species. This can promote a local convective redistribution opposite to, or not fully aligned with, the diffusive supply of hydrogen.

Conversely, on the cathodic side, CO_2 is consumed at the reactive surface together with O_2, without gaseous products being generated. The cathodic reactive surface therefore behaves as a net gas-phase sink. As a consequence, the pressure-driven convective contribution and the concentration-gradient-driven diffusive contribution both support the transfer of CO_2 towards the reactive surface. This explains why the cathodic convective and diffusive fluxes are more directly coupled and why the CO_2 transport field exhibits a clearer spatial imprint of the collector geometry.

The wake-like structures observed in the diffusive flux fields should be interpreted as the consequence of the interaction between local hydraulic shielding and species consumption at the reactive surface. These structures are present on both the anodic and cathodic sides, because in both compartments the embossments locally reduce the direct communication between the feeding channel and the porous electrode.

However, the wake-like pattern is more evident on the cathodic side. This is mainly due to the larger cathodic flow intensity, which enhances the redistribution of the gas around the embossments and makes the shielding effect of the raised features more

pronounced. As a result, the cathodic reactant supply becomes less uniform, and the local concentration gradients inside the porous electrode retain a clearer geometrical imprint of the collector pattern.

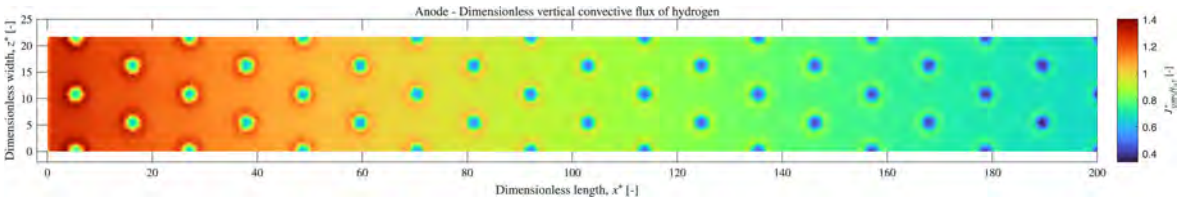

Figure 4.52: Dimensionless vertical convective flux of H_2 inside the anodic porous electrode.

The dimensionless vertical convective flux of hydrogen inside the anodic porous electrode is reported in Figure 4.52. The field exhibits a clear and smooth axial decrease from the inlet towards the outlet. This trend reflects the progressive reduction of the local hydraulic driving conditions and of the hydrogen availability along the anodic porous electrode.

The convective contribution must be interpreted considering the anodic gas-phase balance. Although hydrogen is consumed at the reactive surface, the anodic reaction produces gaseous H_2O and CO_2. Therefore, the reactive surface is not only a hydrogen-consuming boundary, but also a region associated with net gas-phase generation. This can promote a local pressure-driven redistribution of the gas inside the porous electrode and makes the convective hydrogen transport less directly aligned with the diffusive supply towards the reactive surface.

Superimposed on the global axial evolution, the field exhibits a regular periodic structure associated with the embossment arrangement. In the regions between neighbouring embossments, the vertical convective flux remains comparatively high. These regions are more effectively connected to the main channel flow and correspond to preferential paths for hydrogen transport into the porous electrode.

Around the projected position of each embossment, approximately circular regions characterised by a local reduction in the vertical convective flux are observed. These low-flux regions indicate that the collector locally limits pressure-driven gas penetration into the porous electrode over a finite area around each raised feature.

The anodic convective flux field therefore identifies alternating regions of favourable

through-plane hydrogen access and locally screened zones. The overall trend is smooth and uniform, while the local circular deficits provide the geometrical signature of the grooved current collector.

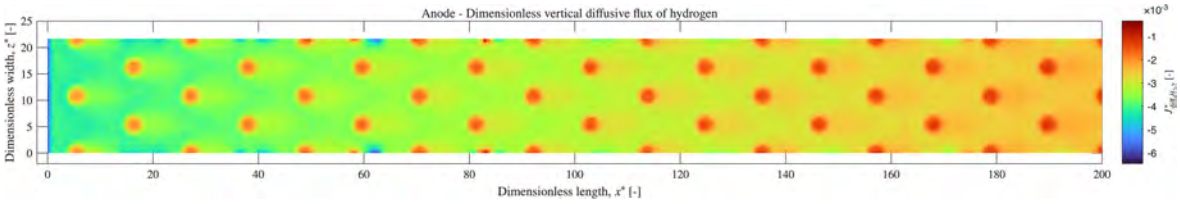

Figure 4.53: Dimensionless vertical diffusive flux of H_2 inside the anodic porous electrode.

The dimensionless vertical diffusive flux of hydrogen is reported in Figure 4.53. The flux is negative over most of the porous domain according to the adopted coordinate convention, indicating that diffusion is directed towards the hydrogen-consuming reactive surface.

The magnitude of the anodic diffusive flux is largest close to the inlet region and progressively decreases along the axial direction. This behaviour is consistent with the evolution of the hydrogen concentration field. Near the inlet, hydrogen availability is higher and the concentration difference between the channel-facing side and the reactive region is more pronounced. Moving downstream, hydrogen is progressively consumed and the through-thickness concentration gradient becomes weaker.

The embossment pattern remains visible in the diffusive field. Wake-like structures can be identified around and downstream of the projected embossment positions, indicating that the shielding effect of the collector also affects the diffusive supply of hydrogen. In these regions, the gas renewal at the channel-facing side of the porous electrode is locally less effective, and the resulting concentration gradients are modified accordingly.

Nevertheless, the spatial contrast remains moderate. This is consistent with the comparatively smooth hydrogen concentration field previously observed at the anodic channel–porous interface and with the higher diffusivity of hydrogen, which tends to attenuate local concentration differences. Consequently, the anodic diffusive flux carries the geometrical signature of the collector, but the associated wake-like structures are smoother and less persistent than those observed on the cathodic side.

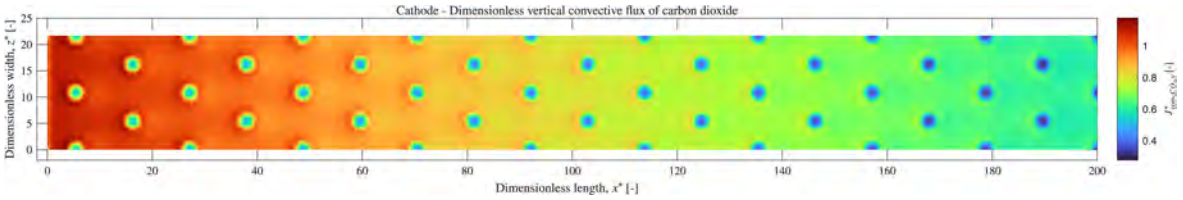

Figure 4.54: Dimensionless vertical convective flux of CO_2 inside the cathodic porous electrode.

The dimensionless vertical convective flux of carbon dioxide inside the cathodic porous electrode is shown in Figure 4.54. The overall spatial structure is similar to that obtained on the anodic side, with a progressive axial decrease and a periodic modulation imposed by the embossment geometry.

On the cathodic side, the interpretation of the convective contribution is different from the anodic case. The electrochemical reaction consumes CO_2 and O_2 at the reactive surface without producing gaseous products. The reactive surface therefore behaves as a net gas-phase sink, favouring a pressure-driven supply of gas from the channel towards the electrode–matrix interface. The convective flux of CO_2 consequently contributes to feeding the reactive surface in the same overall direction as the diffusive transport.

The projected positions of the embossments are surrounded by clearly identifiable low-flux regions, whereas the spaces between neighbouring features maintain a larger vertical convective contribution. These regions are more effectively connected to the cathodic feeding channel and represent preferential paths for carbon dioxide penetration into the porous electrode.

The approximately circular shape of the local flux minima is again evident. In the cathodic case, these structures are sharper and more spatially defined than in the anodic field. This indicates that the cathodic side is more sensitive to the local hydraulic redistribution generated by the collector geometry.

This observation is consistent with the pressure analysis. The cathodic pressure field contains a strong periodic component already visible in the section-averaged profile, and this produces larger spatial differences in the hydraulic forcing transmitted to the porous electrode. Regions hydraulically connected to the open passages receive a stronger vertical supply, whereas the areas associated with the embossment footprint exhibit a pronounced convective flux deficit.

It is important to note that the low-flux regions remain approximately centred around the embossments rather than developing exclusively downstream. Therefore, although the lee-side shielding previously identified in the feeding channel contributes to the local gas redistribution, it is not sufficient by itself to explain the complete geometry of the vertical convective flux field.

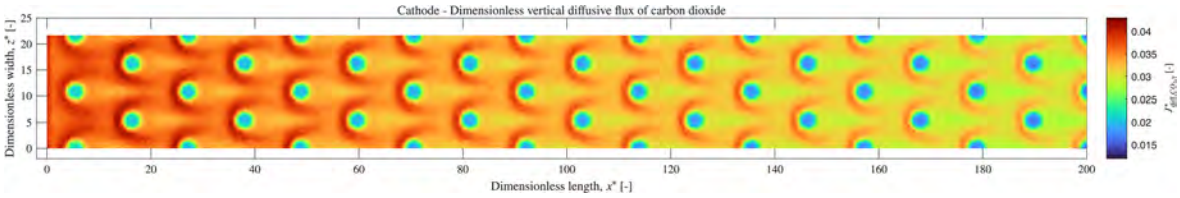

Figure 4.55: Dimensionless vertical diffusive flux of CO_2 inside the cathodic porous electrode.

The cathodic vertical diffusive flux field is reported in Figure 4.55. The diffusive contribution is directed towards the reactive surface and is associated with the concentration gradient generated by the electrochemical consumption of CO_2.

Differently from the anodic side, the cathodic convective and diffusive contributions act in the same overall transport direction. Both mechanisms contribute to supplying CO_2 from the channel-facing side of the porous electrode towards the reactive surface. This explains why the cathodic transport field exhibits a stronger and more coherent spatial organisation.

The field exhibits a smooth axial decrease of the dimensionless diffusive flux from the inlet towards the outlet, while maintaining a pronounced local modulation associated with the embossment pattern. Compared with the anodic hydrogen diffusive field, the cathodic CO_2 diffusive flux presents clearer wake-like structures and larger relative variations.

This behaviour is mainly related to the stronger hydraulic shielding produced by the embossments under cathodic operating conditions. The larger cathodic flow intensity increases the interaction between the gas stream and the raised features, forcing the flow to redistribute more markedly through the open passages. Consequently, the regions screened by the embossments receive a less uniform reactant supply, and the local CO_2 concentration gradients inside the porous cathode become more strongly modulated.

The wake-like structures observed in the cathodic diffusive flux are therefore associated

with the non-uniform renewal of CO_2 at the channel-facing side of the porous electrode. In the screened regions, the convective supply is weaker and the local concentration field is modified accordingly. These regions develop elongated diffusive-flux structures that remain visible downstream of the projected embossment positions.

The stronger visibility of these wakes on the cathodic side does not mean that the phenomenon is absent at the anode. Rather, it indicates that the higher cathodic velocity amplifies the shielding effect of the collector and produces a less uniform distribution of the reacting species before diffusion through the porous electrode takes place.

The comparison between anodic and cathodic transport shows that the porous electrode does not completely eliminate the spatial heterogeneity generated in the feeding channel. The porous resistance strongly suppresses streamwise gas motion, but the local pressure and concentration conditions imposed at the channel-facing surface continue to influence the vertical species flux through the electrode thickness.

On the anodic side, the lower flow intensity and the higher hydrogen diffusivity produce comparatively smoother pressure and concentration distributions. The vertical convective flux remains periodically modulated by the embossments, and the diffusive flux also shows wake-like structures, but these structures are less pronounced because hydrogen redistribution tends to smooth local concentration differences. In addition, the net gas-phase generation at the anodic reactive surface makes the convective contribution less directly aligned with the diffusive supply of hydrogen.

On the cathodic side, the larger flow intensity strengthens the interaction between the gas stream and the embossments. The shielding effect of the raised features is therefore more evident, producing a less uniform CO_2 supply at the channel-facing side of the porous electrode. This non-uniformity is transferred to the concentration field and finally to the vertical diffusive flux, where wake-like structures become clearer and more persistent.

Therefore, the wake-like patterns observed in the species fluxes are not exclusive to one electrode. They represent the transport signature of the collector-induced shielding effect. Their greater visibility on the cathodic side is mainly associated with the stronger gas redistribution caused by the higher cathodic velocity and with the more heterogeneous CO_2 concentration field generated by the interaction between flow, geometry

and electrochemical consumption.

A particularly relevant result is the presence, in both the anodic and cathodic convective flux maps, of approximately circular low-flux regions surrounding the embossment footprints. Their spatial structure cannot be explained exclusively by the streamwise lee-side wake previously identified in the feeding channel.

For this reason, the following subsection investigates the local flow topology around the embossments. The possible formation of vortical structures is first examined through the Q-criterion and the streamwise vorticity component. The analysis is then complemented by the evaluation of the vertical pressure-gradient field in order to determine whether the circular convective-flux deficits originate from vortex-induced secondary motion or from the local hydraulic shielding imposed by the embossment geometry.

The resulting fluid-dynamic interpretation is subsequently related to the local reactant concentration distribution, allowing the effect of the identified transport mechanisms on species availability to be assessed.

4.3.6 Origin of the Local Vertical Convective Velocity Distribution

The vertical convective velocity fields discussed in the previous subsection revealed the presence of local regions of reduced gas penetration around the embossment positions. Since the transport inside the porous electrode is predominantly directed through the electrode thickness, identifying the physical origin of these local velocity reductions is essential for understanding how the grooved current collector affects reactant supply towards the reactive surface.

A first possible explanation was associated with the three-dimensional vortical structures generated by the interaction between the channel flow and the embossments. Wall-mounted obstacles can induce local flow separation and secondary motion when the incoming gas is decelerated by the adverse pressure gradient developing upstream of the obstacle. The separated flow can subsequently wrap around the obstacle base, generating horseshoe-like vortex structures.

Since the proposed collector consists of a periodic staggered arrangement of raised

embossments, the possible formation of such vortical structures was first investigated through the Q-criterion.

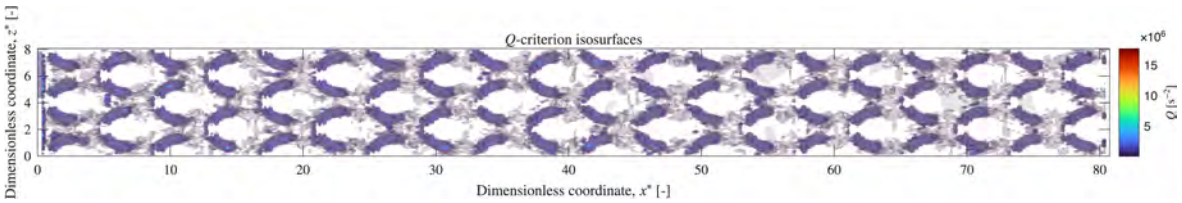

Figure 4.56: Q-criterion isosurfaces inside the grooved feeding channel.

The Q-criterion distribution reported in Figure 4.56 confirms the presence of organised vortical structures throughout the feeding channel. Regions characterized by positive Q repeatedly develop around the embossments and reproduce the periodicity of the grooved collector.

The incoming flow is locally decelerated and redirected when approaching each raised feature. The resulting velocity gradients generate three-dimensional rotational structures around the embossments and through the passages formed by neighbouring elements. Therefore, although the overall flow regime remains laminar, the collector geometry promotes local secondary motion.

To further characterize the orientation of these structures, the streamwise vorticity component, ω_x, was considered.

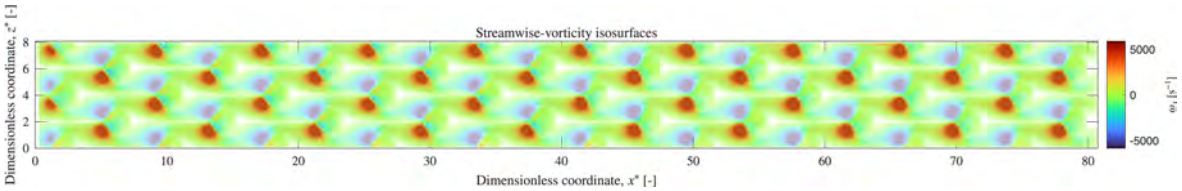

Figure 4.57: Distribution of the streamwise vorticity component, ω_x, inside the grooved feeding channel.

As shown in Figure 4.57, alternating positive and negative values of ω_x are generated around the embossments. The opposite signs observed on the two sides of the raised features indicate counter-rotating secondary motions with a significant streamwise vorticity component.

The repeated arrangement of these counter-rotating regions is compatible with the formation of horseshoe-like vortical structures associated with the interaction between

the incoming channel flow and the embossments. The vortices therefore represent a real feature of the free-channel fluid dynamics and contribute to the redistribution of momentum around the raised collector elements.

However, the presence of vortical structures does not necessarily imply that they control the vertical gas penetration into the porous electrode. To directly assess the mechanism governing the vertical convective transport, the dimensionless vertical pressure-gradient driving term was evaluated at the channel–porous interface.

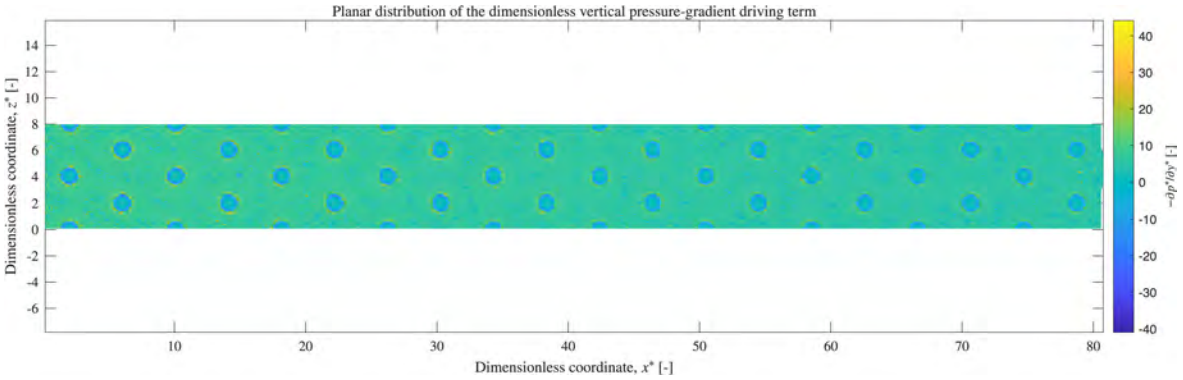

Figure 4.58: Planar distribution of the dimensionless vertical pressure-gradient driving term at the channel–porous interface.

The distribution reported in Figure 4.58 provides the main evidence for identifying the origin of the vertical convective velocity pattern. Over most of the accessible channel–porous interface, the vertical pressure-gradient driving term remains comparatively uniform. In particular, the field does not reproduce the alternating positive and negative structures observed in the streamwise vorticity distribution.

This result indicates that the vertical pressure forcing responsible for gas penetration into the porous electrode is not controlled by the local vortical structures generated in the feeding channel. If the vortices were the dominant mechanism governing the through-plane flow, a corresponding spatial modulation of the vertical pressure-gradient driving term would be expected in association with the vortex pattern. Such a correspondence is not observed.

The background vertical pressure driving is instead broadly distributed over the channel–porous interface. This behaviour is consistent with the coupled transport established between the feeding channel, the porous electrode and the reactive interface, which requires gas transport through the electrode thickness. In the present incompressible

momentum formulation, the electrochemical reaction is not introduced as a volumetric mass source in the continuity equation; therefore, the vertical pressure gradient should not be interpreted as being directly generated by the reaction itself. Nevertheless, the resulting pressure and velocity fields are part of the coupled transport condition supplying the reactive interface.

Local reductions of the vertical pressure-gradient driving term are observed specifically in correspondence with the embossment positions. These regions coincide with the local minima identified in the vertical convective velocity maps.

The correspondence between the pressure-gradient reduction and the embossment geometry indicates that the local decrease in vertical convective transport is primarily caused by the hydraulic shielding produced by the raised collector elements. The embossment locally separates the main channel stream from the underlying porous region and reduces the effective hydraulic communication between the free-flow domain and the porous electrode.

Consequently, immediately beneath and around the projected position of an embossment, the vertical pressure driving available for gas penetration is reduced. Moving away from the solid feature and towards the open channel passages, the porous interface becomes more directly exposed to the gas flow and the vertical pressure-gradient driving term recovers.

The combined analysis therefore allows the two fluid-dynamic phenomena to be clearly distinguished. The Q-criterion and the streamwise vorticity field confirm the existence of horseshoe-like and secondary vortical structures around the embossments. These structures affect the local redistribution of the gas inside the feeding channel. However, the vertical pressure-gradient analysis demonstrates that they are not the dominant mechanism controlling the vertical gas penetration into the porous electrode.

The spatial modulation of the vertical convective velocity is instead governed mainly by the geometrical shielding imposed by the embossments. The broadly distributed vertical pressure driving supports gas penetration across the accessible interface, whereas the locally screened regions beneath the raised features experience a reduced hydraulic forcing and, consequently, a lower vertical convective velocity.

This distinction is fundamental for the subsequent interpretation of species transport,

since the locally reduced convective penetration modifies the renewal of reactants at the channel–porous interface and influences the concentration gradients developing through the porous electrode.

4.3.7 Pressure and Reactant Concentration on the Reactive Surface

The reactive surface represents the final stage of gas transport through the cell, where the effects generated in the feeding channel and transmitted across the porous electrodes directly determine the local conditions available for the electrochemical reactions. For this reason, the pressure and limiting-reactant concentration distributions were evaluated on the anodic and cathodic reactive surfaces before analysing the resulting current density field.

The purpose of this analysis is to determine whether the local spatial modulations introduced by the embossments remain confined to the channel–porous electrode interface or are progressively attenuated during transport through the porous electrode. The reactive-surface fields therefore provide a direct measure of how effectively the porous domains redistribute pressure and species before the electrochemical interface is reached.

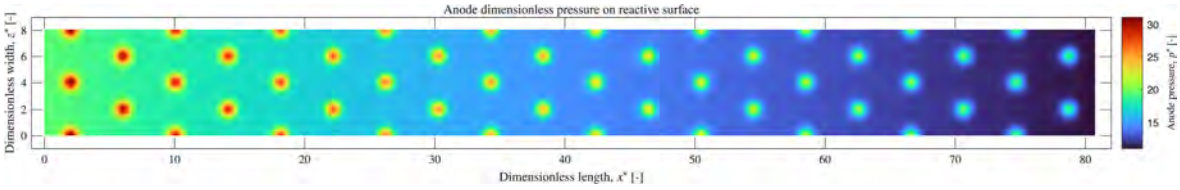

Figure 4.59: Dimensionless pressure distribution on the anodic reactive surface.

The anodic dimensionless pressure distribution on the reactive surface is reported in Figure 4.59. A clear axial decrease is observed from the inlet towards the outlet, consistently with the overall pressure loss developed along the anodic compartment. The large-scale pressure distribution therefore retains the streamwise trend already identified at the channel–porous electrode interface and within the porous electrode.

Superimposed on this axial decrease, a periodic spatial modulation remains visible in correspondence with the projected positions of the embossments. Local pressure

maxima are observed beneath or close to these positions, whereas the surrounding areas exhibit lower values following the global streamwise pressure decay. The periodicity of these local features reproduces the staggered arrangement of the grooved collector.

The persistence of the embossment pattern at the reactive surface demonstrates that the pressure perturbations imposed at the channel–porous electrode interface are not completely dissipated through the porous anode. Although Darcy–Brinkman resistance strongly damps the fluid motion, the pressure field retains a spatial memory of the upstream collector geometry.

Nevertheless, the local pressure perturbations remain superimposed on a comparatively smooth axial background. This indicates that, on the anodic side, the porous medium attenuates part of the local hydraulic non-uniformity while preserving the main imprint of the collector arrangement.

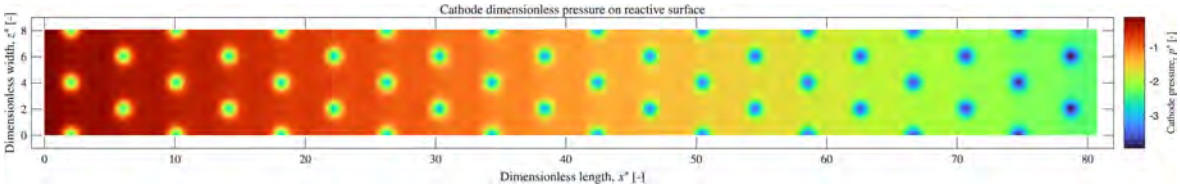

Figure 4.60: Dimensionless pressure distribution on the cathodic reactive surface.

The corresponding cathodic pressure field is shown in Figure 4.60. As for the anode, the dominant feature is a progressive axial pressure decrease. However, the local perturbations associated with the embossments are more clearly distinguished from the surrounding pressure field.

Each embossment position is associated with a localized pressure depression relative to the adjacent surface. These low-pressure regions preserve the staggered periodic arrangement of the collector and indicate that the stronger hydraulic forcing on the cathodic side transmits a more pronounced geometrical imprint through the porous cathode.

The difference between the anodic and cathodic pressure maps is consistent with the fluid-dynamic behaviour discussed in the previous subsections. The cathodic gas enters with a higher reference velocity and is characterized by a higher gas density. Consequently, larger pressure losses and stronger local pressure redistribution are generated when the gas interacts with the embossments. The resulting spatial modulation there-

fore remains more evident after passage through the porous cathode.

The reactive-surface pressure maps confirm that the porous electrodes reduce, but do not completely eliminate, the spatial pressure non-uniformities generated by the grooved collector. The local hydraulic shielding associated with the embossments can therefore still be detected at the final transport interface.

Pressure alone, however, is not sufficient to determine the local electrochemical response. The availability of the reacting species at the reactive surface must also be considered. Hydrogen concentration was therefore analysed on the anodic side, whereas carbon dioxide concentration was considered on the cathodic side.

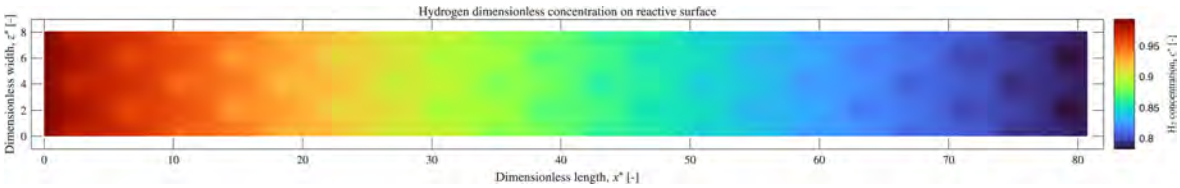

Figure 4.61: Dimensionless H_2 concentration distribution on the anodic reactive surface.

The hydrogen concentration distribution on the anodic reactive surface is reported in Figure 4.61. The dominant behaviour is a smooth and progressive decrease along the cell length, caused by the continuous consumption of hydrogen as the gas moves from inlet to outlet.

The normalized hydrogen concentration decreases from values close to unity at the inlet to approximately 0.8 near the outlet. This axial reduction is considerably more important than the local transverse modulation associated with individual embossments.

A weak periodic imprint can still be identified, particularly in the downstream region, where small local concentration depressions reproduce the staggered collector arrangement. However, these perturbations remain limited in amplitude and spatial extent.

This behaviour is consistent with the concentration field previously observed at the channel–porous electrode interface. The lower anodic channel velocity produces a less pronounced hydraulic separation between directly exposed and shielded regions. Consequently, the hydrogen distribution entering the porous anode is comparatively homogeneous.

Transport through the porous electrode further smooths these local differences. Diffu-

sion redistributes hydrogen from relatively well-supplied regions towards neighbouring areas of lower concentration, reducing the contrast generated by the collector geometry. The reactive-surface hydrogen distribution is therefore predominantly governed by the global axial depletion rather than by severe local concentration shadowing.

The anodic result is important because it shows that the hydraulic shielding generated by the embossments does not translate into an equally strong hydrogen concentration deficit at the reactive surface. The porous anode provides sufficient transverse and through-plane redistribution to attenuate the local concentration perturbations before the reaction interface is reached.

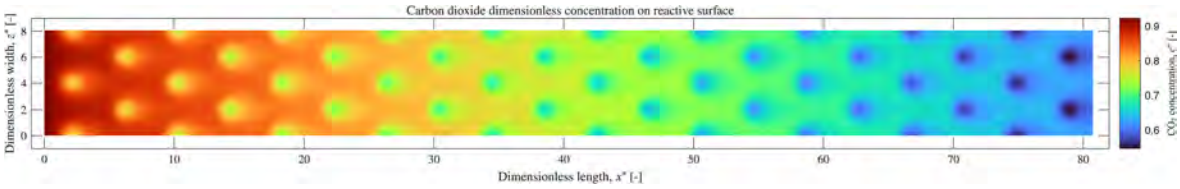

Figure 4.62: Dimensionless CO_2 concentration distribution on the cathodic reactive surface.

A different behaviour is observed for carbon dioxide on the cathodic reactive surface, as shown in Figure 4.62. The global axial reduction remains clearly visible and reflects the progressive consumption of CO_2 along the cathodic gas path. However, the local periodic modulation is considerably stronger than that observed for hydrogen.

Distinct concentration depressions develop at the positions influenced by the embossments. These regions reproduce the staggered collector pattern and become increasingly evident towards the downstream part of the cell.

The progressive amplification of the local concentration non-uniformity can be interpreted by considering the reduction of the mean CO_2 concentration along the channel. Near the inlet, the comparatively high reactant availability limits the relative influence of a local supply reduction. Further downstream, the mean carbon dioxide concentration is lower and the same geometrically induced transport limitation produces a more visible local concentration deficit.

The cathodic concentration distribution therefore retains a strong memory of the hydraulic shadowing identified in the feeding channel and at the channel–porous interface. The regions located downstream of or hydraulically screened by the embossments re-

ceive a weaker convective renewal. As a consequence, carbon dioxide consumed at the reactive surface is less rapidly replenished from the channel side.

Diffusion continues to supply CO_2 towards the reactive surface, but the stronger spatial non-uniformity of the concentration field generates the pronounced diffusive structures discussed previously. The cathodic concentration map can therefore be interpreted as the final result of the interaction between local hydraulic shielding, reactant consumption and diffusion through the porous cathode.

The comparison between Figure 4.61 and Figure 4.62 highlights an important difference between the two compartments. The anodic hydrogen field remains comparatively smooth, whereas the cathodic carbon dioxide distribution exhibits more localised concentration gradients directly correlated with the collector pattern. These variations indicate a non-uniform reactant distribution induced by the current-collector geometry.

This difference is consistent with the stronger fluid-dynamic modulation observed on the cathodic side. The higher cathodic velocity amplifies the distinction between preferential flow paths and shielded regions around the embossments. The resulting non-uniformity is transmitted to the channel–porous electrode interface and subsequently through the porous cathode, producing a more pronounced local variation in reactant availability at the reactive surface.

The reactive-surface pressure and concentration fields therefore establish the final local operating conditions entering the electrochemical model. Their combined influence is reflected in the current density distribution discussed in the following subsection.

4.3.8 Current Density Distribution

The local current density represents the final response of the coupled fluid-dynamic, species-transport and electrochemical model. Under the imposed potentiostatic operating condition, the cell voltage is fixed and the local current density varies according to the local equilibrium potential and electrochemical resistance contributions, both of which depend on the thermodynamic and species conditions at the reactive interface.

The spatial current density distribution therefore provides an integrated representation

of the transport mechanisms discussed in the previous subsections. Axial reactant depletion, pressure evolution, local hydraulic shielding and porous-medium redistribution all contribute to defining the local electrochemical response.

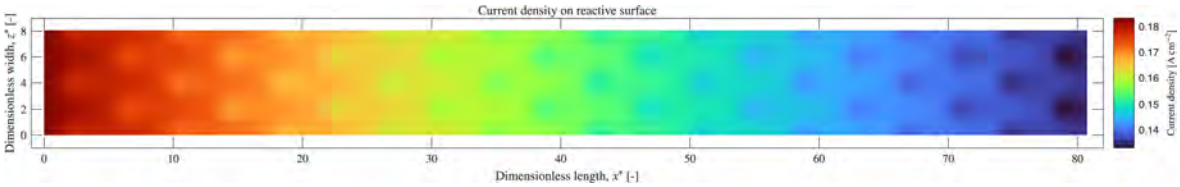

Figure 4.63: Current density distribution on the reactive surface for the grooved current collector.

The current density distribution obtained for the grooved current collector is reported in Figure 4.63. The dominant feature is a progressive decrease from the inlet towards the outlet. Current density values are approximately 0.18 $\mathrm{A, cm^{-2}}$ in the inlet region and progressively decrease to values close to 0.13–0.14 $\mathrm{A, cm^{-2}}$ near the outlet.

This axial trend directly follows the evolution of the local gas composition. Hydrogen and carbon dioxide are progressively consumed along their respective gas paths, reducing the reactant partial pressures available at the electrochemical interfaces. The corresponding variation in the local equilibrium potential and kinetic resistance contributions leads to the observed reduction in current density.

The current density map is comparatively smooth over most of the reactive surface. This indicates that the porous electrodes and diffusive transport substantially attenuate the local fluid-dynamic disturbances generated in the feeding channels before they are transferred to the electrochemical response.

Nevertheless, a weak periodic modulation remains visible, particularly towards the downstream region. Localized current-density depressions reproduce the staggered arrangement of the embossments and are most evident where the reactant concentration has already been reduced by axial consumption. Local hydraulic perturbations affect current production primarily through their influence on reactant transport and local thermodynamic conditions.

The stronger local current-density modulation observed near the outlet is also physically consistent with the progressive reduction in reactant availability. At the inlet, the high concentration of reacting species provides a comparatively large transport margin,

so local perturbations introduced by the collector geometry have a limited effect on the electrochemical response. Towards the outlet, reactant depletion makes the cell more sensitive to local transport non-uniformities. Consequently, the concentration deficits associated with the shadow effect become more clearly reflected in the current density field.

Overall, the grooved current collector maintains electrochemical activity over the complete reactive surface while generating only moderate local current-density non-uniformities. The embossments introduce hydraulic shielding and localized concentration perturbations, particularly on the cathodic side, but the distributed gas access and transport through the porous electrodes prevent the formation of extended inactive regions.

The significance of this behaviour becomes clearer when the grooved collector is compared with the traditional reference configuration, for which the more constrained gas-access geometry produces different hydraulic losses and a different spatial distribution of current density.

4.4 Comparison between Traditional and Grooved Current Collectors

After the detailed analysis of the transport mechanisms developing within the two current-collector configurations, the traditional and grooved geometries can be directly compared in terms of hydraulic, electrochemical and structural response.

The comparison is based on simulations performed under the same operating conditions and therefore isolates the effect of the current-collector geometry. For the hydraulic assessment, the anodic side is considered as representative, since the same relative tendency between the two geometries is also observed on the cathodic side. The discussion therefore focuses on the differences introduced by the collector topology rather than repeating the local analyses presented in the previous sections.

4.4.1 Hydraulic and Electrochemical Comparison

The first relevant difference between the traditional and grooved current collectors concerns the hydraulic resistance generated along the feeding channel. As discussed previously, the traditional configuration constrains the gas through the passages defined by the arched collector structure. The resulting repeated contractions, deviations and locally shielded regions increase the resistance encountered by the gas along the main flow direction.

By contrast, the grooved current collector provides a larger fraction of open passage and a more distributed network of flow paths between neighbouring embossments. Although each embossment produces a local redistribution of the velocity and generates a lee-side region characterised by lower streamwise velocity, the gas is not globally confined within a sequence of narrow passages comparable to those of the traditional collector.

The anodic pressure profiles presented for the two geometries show a total pressure drop of approximately

$$\Delta p_{\text{traditional}} \simeq 55 \text{ Pa}, \tag{4.12}$$

for the traditional current collector, whereas the grooved configuration produces a pressure drop of approximately

$$\Delta p_{\text{grooved}} \simeq 30 \text{ Pa}. \tag{4.13}$$

The reduction in pressure losses obtained with the proposed geometry can therefore be evaluated as

$$\eta_{\Delta p} = \frac{\Delta p_{\text{traditional}} - \Delta p_{\text{grooved}}}{\Delta p_{\text{traditional}}} \times 100, \tag{4.14}$$

which gives

$$\eta_{\Delta p} \simeq 45.5\%. \tag{4.15}$$

The grooved collector therefore reduces the anodic pressure losses by approximately 45% with respect to the traditional reference configuration.

This difference is directly related to the distinct hydraulic interaction between the gas and the collector geometry. In the traditional configuration, the arched elements generate a more restrictive flow path and promote stronger deviations of the main stream. The local velocity profiles also showed regions characterised by pronounced streamwise deceleration and, in some locations, changes in the sign of the local velocity component, indicating a stronger redistribution of the flow around the structural elements.

In the grooved geometry, the embossments also perturb the flow locally. The circumferential profiles demonstrated a clear distinction between the stoss and lee sides of each bump, with a velocity deficit developing downstream of the obstacle. However, these disturbances remain embedded within a largely open flow domain. The gas can progressively redistribute through neighbouring passages, thereby limiting the cumulative hydraulic resistance along the cell.

The reduction in pressure losses is particularly relevant because it is obtained without suppressing the local interaction between the gas and the porous electrode. On the contrary, the pressure-fluctuation fields and the vertical velocity distributions showed that the periodic embossment pattern continuously modifies the pressure field at the channel–porous electrode interface. The resulting local pressure differences contribute to the vertical penetration of gas into the porous electrode.

The electrochemical response reflects the combined effect of this improved hydraulic accessibility and of the resulting species distribution. The average current density calculated for the traditional current collector is

$$\overline{j}_{\text{traditional}} = 0.14800 \text{ A cm}^{-2}, \tag{4.16}$$

whereas the grooved current collector reaches

$$\overline{j}_{\text{grooved}} = 0.15601 \text{ A cm}^{-2}. \tag{4.17}$$

The relative increase in average current density is therefore

$$\eta_j = \frac{\overline{j}_{\text{grooved}} - \overline{j}_{\text{traditional}}}{\overline{j}_{\text{traditional}}} \times 100, \tag{4.18}$$

corresponding to

$$\eta_j \simeq 5.4\%. \tag{4.19}$$

The proposed collector therefore produces an increase of approximately 5.4% in the average current density under the same imposed cell voltage and operating conditions.

The improvement should not be interpreted as the consequence of a spatially uniform increase in gas velocity. Indeed, the detailed analysis of the grooved collector showed the persistence of local shadow regions downstream of the embossments. Instead, the improvement results from the larger-scale redistribution of the gas over the active region and from the stronger communication between the feeding channel and the porous electrodes.

This distinction is particularly evident from the pressure and concentration fields. The periodic structure of the grooved collector remains visible at the channel–porous electrode interface and, to a lesser extent, on the reactive surface. However, the global reactant supply is maintained over a larger fraction of the active area. The current-density distribution consequently preserves the local imprint of the collector geometry while exhibiting a higher average electrochemical response.

The hydraulic and electrochemical results therefore indicate that the reduction in global flow resistance does not compromise electrode feeding. The grooved geometry simultaneously decreases the pressure losses and increases the average current density, demonstrating that a larger open flow area can be combined with effective communication between the feeding channel and the porous electrode.

4.4.2 Structural Performance under Stack Compression

In addition to the fluid-dynamic and electrochemical comparison, the mechanical response of the two current-collector geometries was investigated. The proposed grooved configuration modifies the path through which the external stack compression is trans-

mitted across the cell assembly. A preliminary structural assessment was therefore performed to determine how the collector topology affects stress localisation and load transfer.

A static structural analysis was carried out using Autodesk Inventor. Both current-collector configurations were subjected to the same uniformly applied compressive load, corresponding to a nominal assembly pressure of

$$p_{\text{app}} = 4.35 \text{ MPa}. \tag{4.20}$$

This value was selected consistently with the MCFC stack assembly pressure reported by Zhang et al. [27]. The same loading condition was imposed on both configurations in order to isolate the effect of the current-collector geometry on the mechanical response. The analysis focused on two complementary quantities: the equivalent von Mises stress and the contact-pressure distribution.

The von Mises stress was analysed to identify regions of concentrated mechanical loading within the metallic current collector and to compare the way in which the two geometries redistribute the externally applied compression. The contact-pressure distribution was instead examined to evaluate the localisation of the transmitted load at the contact interfaces and to identify configurations that could generate highly concentrated loading on the porous electrode.

The present investigation is intended as a comparative mechanical assessment of the two collector layouts. A complete description of the porous-electrode mechanical response would require a dedicated constitutive model capable of reproducing progressive compaction, local pore collapse and possible material damage. These aspects are beyond the scope of the present work and the results are therefore interpreted primarily in comparative terms.

Equivalent von Mises Stress

The equivalent von Mises stress provides a scalar measure of the local multiaxial stress state within the metallic structure. In the present analysis, it is used to identify stress-concentration regions and to compare how effectively the traditional and grooved

geometries redistribute the applied compressive load.

The equivalent von Mises stress distribution obtained for the grooved current collector is shown in Figure 4.64.

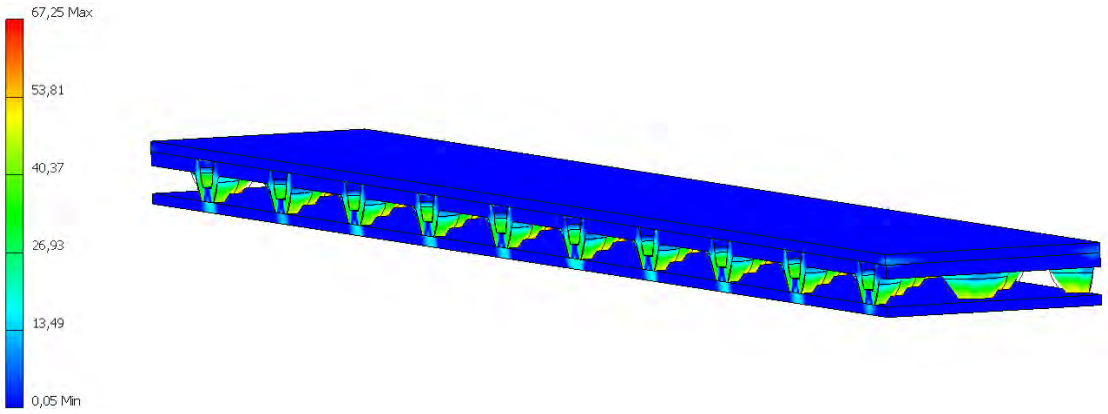

Figure 4.64: Equivalent von Mises stress distribution for the grooved current collector.

The corresponding stress field for the traditional current collector is reported in Figure 4.65.

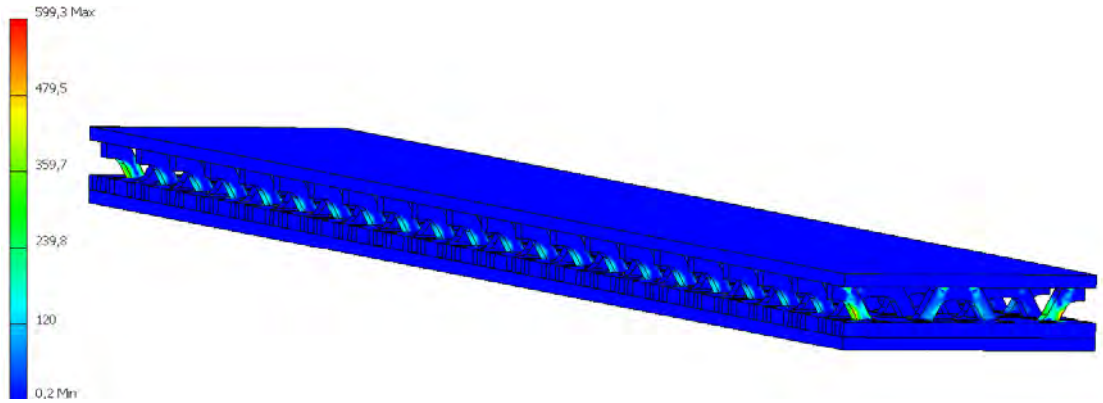

Figure 4.65: Equivalent von Mises stress distribution for the traditional current collector.

The maximum equivalent von Mises stress obtained for the grooved configuration is approximately

$$\sigma_{\mathrm{VM,max}}^{\mathrm{grooved}} \simeq 67.25 \text{ MPa}, \tag{4.21}$$

whereas the traditional collector reaches a maximum value of approximately

$$\sigma_{\mathrm{VM,max}}^{\mathrm{traditional}} \simeq 599.3 \text{ MPa}. \tag{4.22}$$

The corresponding reduction in maximum equivalent stress is

$$\eta_\sigma = \frac{\sigma_{\mathrm{VM,max}}^{\mathrm{traditional}} - \sigma_{\mathrm{VM,max}}^{\mathrm{grooved}}}{\sigma_{\mathrm{VM,max}}^{\mathrm{traditional}}} \times 100, \tag{4.23}$$

giving

$$\eta_\sigma \simeq 88.8\%. \tag{4.24}$$

A substantially lower peak equivalent stress is therefore obtained for the grooved current collector.

The stress maps show that this difference is associated with the load-transfer mechanism of the two geometries. In the traditional collector, the compression is transmitted through the arched structural elements. The changes in section and the local geometry of the arches generate highly localised stress-concentration regions. The maximum von Mises stress is consequently confined to a limited number of mechanically critical areas.

The grooved configuration exhibits a different response. The repeated embossed topology generates a larger number of load-transfer regions distributed over the collector. The highest stresses remain concentrated around local geometrical transitions of the embossed structure, where curvature and changes in the load path are present. However, their magnitude is considerably lower than that obtained for the traditional collector.

The comparison therefore indicates that the grooved geometry provides a more distributed transfer of the externally applied compressive load. The marked reduction in maximum von Mises stress limits the intensity of localised mechanical loading within the metallic structure and represents a favourable feature from a structural-design perspective.

Contact-Pressure Distribution

The contact-pressure distribution was analysed to determine how the externally applied compression is transferred through the local contact regions of the collector. This quantity is particularly relevant for the interaction with the porous electrode, since a highly localised contact load could promote local indentation, compaction or a punching-like effect on the porous structure.

The contact-pressure distribution obtained for the grooved current collector is shown in Figure 4.66.

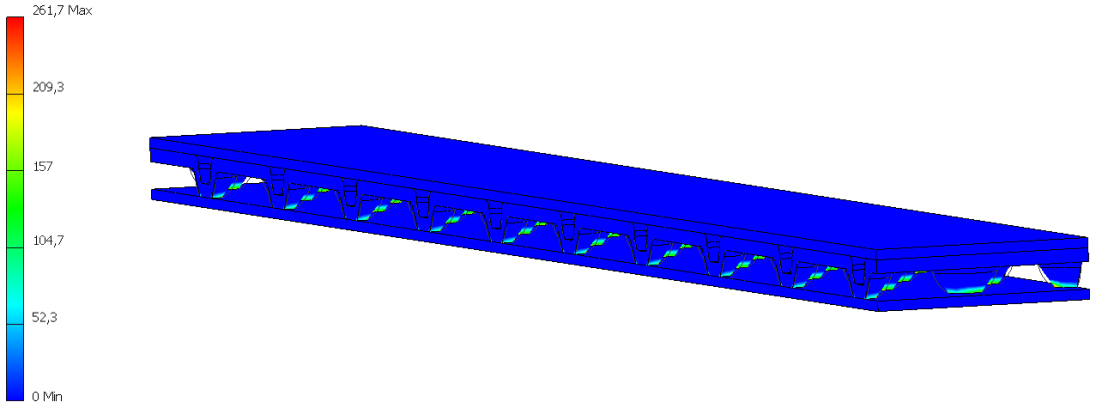

Figure 4.66: Contact-pressure distribution for the grooved current collector.

The corresponding contact-pressure analysis for the traditional current collector is reported in Figure 4.67.

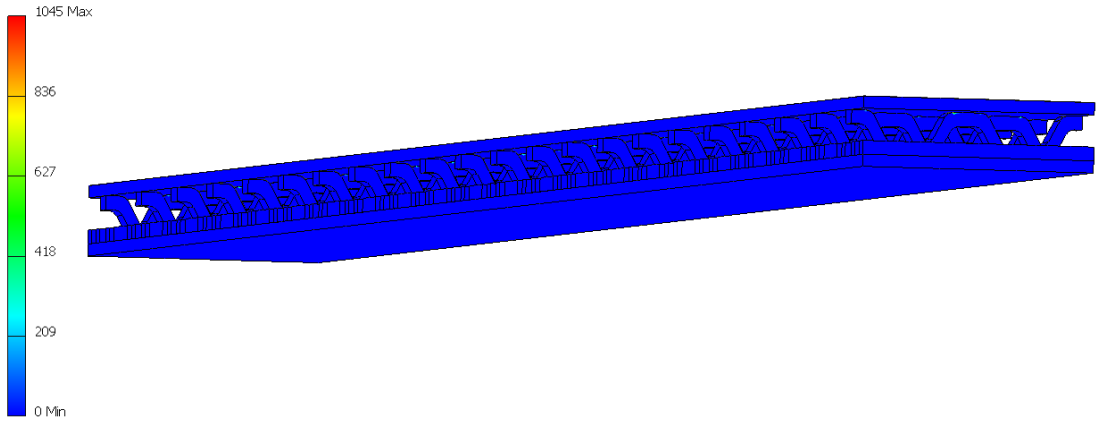

Figure 4.67: Contact-pressure distribution for the traditional current collector.

For the grooved configuration, the maximum local contact pressure reaches approximately

$$p_{\text{contact,max}}^{\text{grooved}} \simeq 261.7 \text{ MPa}. \tag{4.25}$$

The contact-pressure field is concentrated at the discrete contact regions generated by the embossed topology. The local increase in pressure is associated with the reduced effective area through which the externally applied load is transmitted. Nevertheless, the repeated arrangement of the embossments distributes these contact regions over the collector surface.

The interpretation of the traditional configuration requires particular care. In the reference arrangement analysed throughout this work, the arched side of the traditional current collector does not face the porous electrode. Consequently, the contact pressure directly exerted by the arch apices on the porous medium is approximately zero in the actual traditional configuration.

The maximum value reported by the structural analysis,

$$p_{\text{contact,max}}^{\text{traditional}} \simeq 1045 \text{ MPa}, \tag{4.26}$$

is therefore associated with the local contact regions within the analysed assembly and must not be interpreted as a pressure directly applied to the porous electrode in the reference configuration.

Nevertheless, the result is particularly useful from a design perspective. During the development of the grooved collector, a possible alternative strategy could have consisted of simply reversing the orientation of the traditional current collector. Such a configuration would have exposed the open portion of the arches to the gas channel and could therefore have increased the gas-accessible area without introducing a new collector topology.

However, reversing the traditional current collector would simultaneously place the arch apices in direct contact with the porous electrode. The contact-pressure analysis shows that the traditional arched geometry is characterised by considerably stronger local pressure concentrations than the grooved configuration. If these concentrated contact regions were transferred directly to the porous medium, the applied stack

compression would be transmitted through highly restricted local areas.

This load-transfer mechanism could promote local indentation, concentrated compaction or a punching-like mechanical action on the porous electrode. Although a dedicated failure criterion for the porous material is not implemented in the present structural model, the magnitude and localisation of the calculated contact pressure indicate that a simple inversion of the traditional collector would represent a mechanically unfavourable design solution.

The grooved geometry avoids this limitation. Its topology allows the gas-accessible area to be increased while maintaining a repeated distribution of contact regions over the adjoining layer. Local contact-pressure amplification remains present, as expected for a patterned structure subjected to compression, but the contact load is transmitted through a more distributed set of geometrical features.

The structural results therefore provide an additional criterion supporting the adopted collector design. The grooved configuration exhibits a markedly lower maximum von Mises stress and avoids the severe local contact-loading mechanism that would result from placing the traditional arch apices directly against the porous electrode. The proposed topology consequently provides a more favourable mechanical load transfer while preserving the fluid-dynamic advantages identified in the preceding analysis.

Chapter 5

Conclusions and Future Perspectives

The present thesis investigated the influence of current-collector geometry on the fluid-dynamic, mass-transport, and electrochemical behaviour of a Molten Carbonate Fuel Cell (MCFC). The main objective was to evaluate a grooved current collector characterized by a high free-area ratio (>80%) as an alternative to a traditional industrial configuration. A more open structure should reduce the shadow effect and permit lower polarization losses but could also increase the risk of cell mechanical failure in view of high compression pressures required for cell assembly. This issue limits the effective free-area ratio in a traditional configuration (around 60%) but was overcome by proposing a completely new geometry based on an embossed surface.

A three-dimensional multiphysics model was developed in COMSOL Multiphysics, which couples free-channel flow, porous-medium transport, multicomponent species transport, and local electrochemical formulation by assuming a stationary isothermal system. The three collector designs were analysed under the same operating conditions and cell geometry. The grooved current collector-based cell was compared to a traditional structure-based cell. The free channel geometry was considered the reference case.

The detailed fluid-dynamic analysis of the feeding channels shows that the grooved geometry redistributes the gas through the periodic embossment pattern and maintains a laminar regime. Local acceleration occurs in the open passages, whereas lower velocities develop on the lee side of the embossments because of geometrical shielding. The velocity profiles confirm the progressive transition from predominantly streamwise

transport in the channel to vertical transport through the porous electrodes.

In view of different flow rates, the anodic and cathodic reactant distributions vary. A lower anodic gas velocity results in a comparatively smoother hydrogen distribution, whereas a higher cathodic velocity produces more pronounced wake-like concentration deficits in the carbon dioxide field. These local transport differences are transmitted through the porous electrodes and remain visible at the reactive surface.

Comparing current collectors, the grooved configuration allows a clear reduction in hydraulic resistance. On the anodic side, the pressure drop decreases from approximately 4.2 Pa cm^{-1} for the traditional collector to approximately 2.3 Pa cm^{-1} for the grooved geometry, corresponding to a reduction of about 45%. Similar qualitative trends are observed on the cathodic side.

The improved gas accessibility is also reflected in the electrochemical response. Assuming a potentiostatic operation, the average current density increases moving from the traditional configuration to the grooved collector, corresponding to an improvement of approximately 5.4%.

A preliminary static structural analysis was also performed in Autodesk Inventor under an applied compressive pressure of 4.35 MPa. The maximum von Mises stress decreases from approximately 599.3 MPa for the traditional configuration to approximately 67.25 MPa for the grooved geometry.

Overall, the proposed grooved current collector shows a favourable combination of a lower hydraulic resistance, an improved average electrochemical response and a more favourable structural stress distribution.

Nevertheless, the present model includes simplifying assumptions. The porous electrodes are represented as homogeneous equivalent media, the matrix and electrolyte are not explicitly resolved, and the simulations are performed under stationary and isothermal conditions. The results should therefore be interpreted primarily as a comparative assessment of the two current-collector geometries. Future work should remove these simplifying assumptions to have a more detailed cell description. A systematic optimisation of embossment size, spacing, height and arrangement should also be performed.

In conclusion, the present work identifies current collector design as a relevant pathway for improving MCFC operation. The proposed grooved geometry reduced pressure losses, increased the average current density and improved the structural response with respect to the traditional reference configuration, supporting its further optimisation and experimental investigation.

Bibliography

[1] International Energy Agency. *Net Zero by 2050: A Roadmap for the Global Energy Sector*. International Energy Agency, 2021. URL: https://www.iea.org/reports/net-zero-by-2050.

[2] Intergovernmental Panel on Climate Change. *Climate Change 2023: Synthesis Report*. IPCC, 2023. URL: https://www.ipcc.ch/report/ar6/syr/.

[3] L. Caprile, B. Passalacqua, and A. Torazza. "Carbon capture: Energy wasting technologies or the MCFCs challenge?" In: *International Journal of Hydrogen Energy* 36.16 (2011), pp. 10269–10277. DOI: 10.1016/j.ijhydene.2010.10.028.

[4] Ricardo R. Contreras, Jorge Almarza, and Luis Rinc'on. "Molten carbonate fuel cells: A technological perspective and review". In: *Energy Sources, Part A: Recovery, Utilization, and Environmental Effects* (2025). DOI: 10.1080/15567036.2021.2013346.

[5] Chang-Whan Lee et al. "Study on the effect of current collector structures on the performance of MCFCs using three-dimensional fluid dynamics analysis". In: *Journal of Industrial and Engineering Chemistry* 51 (2017), pp. 153–161. DOI: 10.1016/j.jiec.2017.02.026.

[6] Emilio Audasso. "Simulation of High Temperature Fuel Cells for Carbon Capture". PhD thesis. University of Genoa, 2021.

[7] Massimiliano Della Pietra, Stefano Frangini, and Luca Turchetti. "MCEC, a promising, innovative and versatile technology". In: *Energia, Ambiente e Innovazione* 1 (2021), pp. 77–81. DOI: 10.12910/EAI2021-016.

[8] Chang-Whan Lee et al. “Effect of the flow directions on a 100 cm2 MCFC single cell with internal flow channels”. In: *International Journal of Hydrogen Energy* 41.41 (2016), pp. 18747–18760. DOI: 10.1016/j.ijhydene.2016.03.188.

[9] Emilio Audasso et al. “New, Dual-Anion Mechanism for Molten Carbonate Fuel Cells Working as Carbon Capture Devices”. In: *Journal of The Electrochemical Society* 167.8 (2020), p. 084504. DOI: 10.1149/1945-7111/ab8979.

[10] Tomasz Wejrzanowski et al. “Microstructure driven design of porous electrodes for molten carbonate fuel cell application: Recent progress”. In: *International Journal of Hydrogen Energy* 45.47 (2020), pp. 25719–25732. DOI: 10.1016/j.ijhydene.2019.12.038.

[11] Seung-Goo Kim et al. “A study on the chemical stability and electrode performance of modified NiO cathodes for molten carbonate fuel cells”. In: *Electrochimica Acta* 49.19 (2004), pp. 3081–3089. DOI: 10.1016/j.electacta.2004.01.027.

[12] A. Wijayasinghe, B. Bergman, and C. Lagergren. “LiFeO2–LiCoO2–NiO materials for Molten Carbonate Fuel Cell cathodes. Part I: Powder synthesis and material characterization”. In: *Solid State Ionics* 177.1–2 (2006), pp. 165–173. DOI: 10.1016/j.ssi.2005.10.018.

[13] A. Wijayasinghe, B. Bergman, and C. Lagergren. “LiFeO2–LiCoO2–NiO materials for Molten Carbonate Fuel Cell cathodes. Part II: Fabrication and characterization of porous gas diffusion cathodes”. In: *Solid State Ionics* 177.1–2 (2006), pp. 175–184. DOI: 10.1016/j.ssi.2005.10.019.

[14] Karol Cwieka et al. “Microstructure and electrochemical behavior of layered cathodes for molten carbonate fuel cells”. In: *Journal of Power Sources* 482 (2021), p. 229949. DOI: 10.1016/j.jpowsour.2021.229949.

[15] Asrar A. Sheikh et al. “A review on MCFC matrix: State-of-the-art, degradation mechanisms and technological improvements”. In: *Heliyon* 10.4 (2024), e25847. DOI: 10.1016/j.heliyon.2024.e25847.

[16] Zijing Lin, Jeffry W. Stevenson, and Mohammad A. Khaleel. “The effect of interconnect rib size on the fuel cell concentration polarization in planar SOFCs”. In: *Journal of Power Sources* 117.1–2 (2003), pp. 92–97. DOI: 10.1016/S0378-7753(02)00726-7.

[17] Pavel Shuhayeu et al. “Degradation and Corrosion of Metal Components in High-Temperature Molten Salt Fuel Cells”. In: *Energies* 18.13 (2025), p. 3317. DOI: 10.3390/en18133317.

[18] G. Durante et al. “High temperature corrosion of metallic materials in molten carbonate fuel cells environment”. In: *Journal of Power Sources* 152.1 (2005), pp. 204–209. DOI: 10.1016/j.jpowsour.2005.01.031.

[19] B. Bergman. “Contact corrosion resistance between the cathode and current collector plate in the molten carbonate fuel cell”. In: *Journal of The Electrochemical Society* (2001). DOI: 10.1149/1.1339027.

[20] Jaroslaw Milewski et al. “Experimental and Theoretical Investigation of Contact Resistance in Molten Carbonate Fuel Cells”. In: *SSRN Electronic Journal* (2023). DOI: 10.2139/ssrn.4340797.

[21] MinJoong Kim et al. “Corrosion-resistant coating for cathode current collector and wet-seal area of molten carbonate fuel cells”. In: *International Journal of Hydrogen Energy* 43 (2018), pp. 11363–11371. DOI: 10.1016/j.ijhydene.2018.02.196.

[22] Guanyu Tao et al. “Research progress on bipolar plates in proton exchange membrane fuel cells: Application of carbon materials and key technologies”. In: *Journal of Power Sources* 626 (2025), p. 235791. DOI: 10.1016/j.jpowsour.2024.235791.

[23] Tao Liu, Youkun Tao, and Haohui Song. “Degradation mechanisms and protective coatings for ferritic stainless-steel interconnects of solid oxide fuel cells: A review”. In: *Materials Today Communications* 41 (2024), p. 110802. DOI: 10.1016/j.mtcomm.2024.110802.

[24] Zhenguo Yang et al. “Oxidation Behavior of Ferritic Stainless Steels under SOFC Interconnect Exposure Conditions”. In: *Journal of The Electrochemical Society* 151.12 (2004), B669–B678. DOI: 10.1149/1.1810393.

[25] T. Dey et al. “Study of contact resistance at the electrode-interconnect interfaces in planar type Solid Oxide Fuel Cells”. In: *Journal of Power Sources* 233 (2013), pp. 290–298. DOI: 10.1016/j.jpowsour.2013.01.111.

[26] Danilo Marra, Barbara Bosio, and Elisabetta Arato. "Fluid-dynamic characterisation of MCFC gas distributors". In: *Chemical Engineering and Processing: Process Intensification* 48.3 (2009), pp. 797–807. DOI: 10.1016/j.cep.2008.10.005.

[27] Ruiyun Zhang et al. "Analysis of the assembly pressure of a high-power molten carbonate fuel cell stack during initial roasting". In: *Fuel* 378 (2024), p. 132895. DOI: 10.1016/j.fuel.2024.132895.

[28] Claude-Louis Navier. "M'emoire sur les lois du mouvement des fluides". In: *M'emoires de l'Acad'emie Royale des Sciences de l'Institut de France* 6 (1822), pp. 389–440.

[29] George Gabriel Stokes. "On the theories of the internal friction of fluids in motion, and of the equilibrium and motion of elastic solids". In: *Transactions of the Cambridge Philosophical Society* 8 (1845), pp. 287–319.

[30] H. C. Brinkman. "A calculation of the viscous force exerted by a flowing fluid on a dense swarm of particles". In: *Applied Scientific Research* 1 (1949), pp. 27–34. DOI: 10.1007/BF02120313.

[31] R. Byron Bird, Warren E. Stewart, and Edwin N. Lightfoot. *Transport Phenomena*. 2nd ed. John Wiley & Sons, 2002. ISBN: 978-0-471-41077-5.

[32] J. Kozeny. ""Uber kapillare Leitung des Wassers im Boden". In: *Sitzungsberichte der Akademie der Wissenschaften in Wien* 136.2a (1927), pp. 271–306.

[33] P. C. Carman. "Fluid flow through granular beds". In: *Transactions of the Institution of Chemical Engineers* 15 (1937), pp. 150–166.

[34] E. L. Cussler. *Diffusion: Mass Transfer in Fluid Systems*. 3rd ed. Cambridge University Press, 2009. ISBN: 978-0-521-87121-1.

[35] Adolf Fick. "Ueber Diffusion". In: *Annalen der Physik* 170.1 (1855), pp. 59–86. DOI: 10.1002/andp.18551700105.

[36] Edward A. Mason and A. P. Malinauskas. *Gas Transport in Porous Media: The Dusty-Gas Model*. Elsevier, 1983. ISBN: 978-0-444-42115-9.

[37] M. Y. Ramandi, P. Berg, and I. Dincer. "Three-dimensional modeling of polarization characteristics in molten carbonate fuel cells using peroxide and superoxide mechanisms". In: *Journal of Power Sources* 218 (2012), pp. 192–203. DOI: 10.1016/j.jpowsour.2012.06.062.

[38] C. R. Wilke and C. Y. Lee. "Estimation of Diffusion Coefficients for Gases and Vapors". In: *Industrial & Engineering Chemistry* 47.6 (1955), pp. 1253–1257. DOI: 10.1021/ie50546a056.

[39] E. Audasso, B. Bosio, and S. Nam. "Extension of an effective MCFC kinetic model to a wider range of operating conditions". In: *International Journal of Hydrogen Energy* 41.12 (2016), pp. 5571–5581. DOI: 10.1016/j.ijhydene.2015.10.152.

[40] Lucia Cardona et al. "Reversible molten carbonate cells: Testing and preliminary formulation of a kinetic model". In: *Electrochemistry Communications* 179 (2025), p. 108023. DOI: 10.1016/j.elecom.2025.108023.

[41] Tomasz Wejrzanowski et al. "Optimization of the Microstructure of Molten Carbonate Fuel Cell Anode". In: *Materials Science Forum* 890 (2017), pp. 274–277. DOI: 10.4028/www.scientific.net/MSF.890.274](http://www.scientific.net/MSF.890.274).